Electrical Waveform Configuration Across Cardiac Scales: Effects on Subcutaneous Myocardial Excitation, Ventricular Fibrillation Induction, and hiPSC-CM Maturation-Relevant Transcriptional Responses



Study submitted in part fulfilment of the requirement for the award of

PhD

School Of Electronic Engineering

Peter Bennett, Beng Tech, Beng (Hons)

August 2026

Supervisor:

Prof. Stephen Daniels

Declaration

I hereby certify that this material, which I now submit for assessment on the programme of study leading to the award of Doctor of Philosophy is entirely my own work, and that I have exercised reasonable care to ensure that the work is original and have conformed to the regulations on the use and declaration of Generative AI, and does not to the best of my knowledge breach any law of copyright, and has not been taken from the work of others save and to the extent that such work has been cited and acknowledged within the text of my work.

Signed: Peter Bennett

ID Number: 10212759

Date: 28th August 2026

Gen AI Tool Use

Generative AI tools were used in a limited editorial capacity during the preparation of this thesis. Their use was restricted to language refinement, sentence restructuring, grammar checking, clarity of expression and review of academic tone. Generative AI tools were not used to generate primary data, perform statistical analyses, fabricate results, create references, replace literature review, or substitute for the candidate's interpretation of the research findings. All scientific content, experimental design, data analysis, interpretation and final editorial decisions remain the responsibility of the candidate. I confirm that I have conformed to the regulations on the use and declaration of Gen AI.

Tool	Purpose of use	Thesis sections affected	Candidate oversight
ChatGPT / OpenAI language model	Editorial support, language refinement, sentence restructuring, grammar checking, clarity of expression and academic tone review	Used selectively across thesis drafts, particularly for improving readability and coherence of candidate-authored text	All outputs were reviewed, edited and approved by the candidate. No primary data, statistical outputs, references or scientific conclusions were generated by the tool.
Grammarly	Grammar checking, spelling correction, punctuation review, sentence clarity suggestions and consistency of written expression	Used selectively across thesis drafts to support proofreading and language clarity	All suggested changes were reviewed and accepted or rejected by the candidate. Grammarly was not used to generate scientific content, analyse data, create references, or alter the interpretation of research findings.

Dedication

I dedicate this work to my three fantastic children, Darragh, David and Oisín, to show them what is possible.

Acknowledgements

To my amazing wife, Cora, thank you for your patience, love and support throughout this journey. You may never fully understand my obsession with academic endeavour, but I owe you more than I can express for everything you have done over the past number of years. To our three wonderful children, Darragh, David and Oisín, thank you for your understanding, encouragement and patience when this project demanded so much time and attention. You have been a constant source of motivation, and I hope this work shows you that difficult goals can be achieved through perseverance and belief.

To my mother, Aileen, who has been a pillar of strength throughout my life, I owe a debt of gratitude that words could never adequately express. Everything I have achieved, including this PhD, rests in no small part on the foundation she created, and I hope she knows how deeply grateful and proud I am to be her son.

To my brother, Eoin, thank you for your encouragement, humour and support. Your success, both professionally and personally, has been an inspiration to me. Consider this thesis one small step towards following your example, although going forward, I will insist that you address me as Dr Bennett.

I would also like to remember my beloved grandparents, Paddy and Laura, who played an immeasurable part in shaping my life and the person I am today. Although they are no longer with us, their love, kindness and unwavering belief in me have remained a constant source of strength throughout this journey. I was incredibly fortunate to have them in my life, and the example they set through their warmth, generosity and devotion to our family continues to guide me. They were, quite simply, the best grandparents I could ever have wished for. I will always be profoundly grateful for everything they gave me, and I hope they would have been proud to see me reach this point.

I would also like to sincerely acknowledge Boston Scientific for its commitment to supporting and funding this PhD. In particular, I would like to thank Brian Aseltine, Kevin O'Riordan, Mike Keane, Anna Paschero, Moira Sweeney and Jake Ludwig for their continued support, encouragement and belief in both this project and in me throughout the journey. Their willingness to invest in the research, provide the time and resources required, and support my professional and academic development has been instrumental in allowing

me to reach this point. I am genuinely grateful for the opportunities, trust and support that Boston Scientific has provided throughout this work.

I would like to extend my sincere thanks to all the amazing staff at CIMA in Pamplona. During this project, I have had the privilege of working with exceptional colleagues and collaborators, many of whom I now also consider friends. Your expertise, generosity and support have made an important contribution to this work, and I am deeply grateful for the time, knowledge and encouragement you have shared with me.

A special word of thanks is due to Stephen Hahn. His support, encouragement, technical insight and mentorship over the past number of years have been invaluable. I would have been lost without his guidance, and I am deeply grateful for the time, patience and expertise he has shared with me.

Finally, I would like to express my sincere gratitude to Professor Stephen Daniels. I cannot thank you enough for your support, guidance and encouragement throughout this project. It has been an incredible privilege and pleasure to work with you, and your mentorship has been central to the completion of this thesis. Your belief in the work, your advice throughout the many challenges along the way, and your continued encouragement have played an enormous part in bringing this journey to its conclusion.

Table of Contents

Declaration II

Gen AI Tool Use III

Dedication IV

Acknowledgements V

Table of Contents VII

Table of Abbreviations XI

List of Symbols XV

List of Figures XVII

List of Tables XXI

Research Outputs XXIII

Ethics and Regulatory Approval XXV

Data Availability and Supporting Evidence XXVI

Abstract XXVIII

Chapter 1 : Clinical Rationale and Research Framework for Cardiac Waveform Optimisation 1

1.1. Introduction and Research Motivation 1

1.1.1. Global Burden of Cardiovascular Disease 1

1.2. Electrical Stimulation in Cardiovascular Medicine 2

1.3. Knowledge Gap in Electrical Waveform Optimisation 7

1.4. Research Aim and Objectives 9

1.5. Hypotheses 10

1.6. Novel Contributions 11

1.7. Thesis Structure and Chapter Interlinking 12

Chapter 2 : Development of a Custom Waveform Generator for Subcutaneous Cardiac Pacing and hiPSC Cardiac Tissue Stimulation 14

2.1. Introduction and Background 14

2.2. Design Objectives and System Overview 16
2.3. System Design and Architecture 17
2.3.1. Power supply architecture 21
2.3.2. Control Unit and Switching Logic 21
2.3.3. Control and Operational Modes 23
2.4. Validation and Testing 24
2.4.1. Pulse Timing and Waveform Parameters 25
2.4.2. Current Regulation 25
2.4.3. Operational Stability 26
2.5. Discussion and Future Work 26
2.6. Limitations 26
2.7. Future improvements: 27
2.7.1. Multi-channel output 27
2.7.2. Closed-loop control 27
2.7.3. Enhanced GUI and data logging 27
2.8. Conclusion 28
Chapter 3 Subcutaneous Pacing 29
3.1. Introduction 29
3.1.1. Research Question 31
3.2. Method 32
3.2.1. Subcutaneous Pacing Threshold Testing Preparation 32
3.2.2. Subcutaneous Pacing Threshold Testing Method 33
3.3. Results 34
3.3.1. Subcutaneous Testing Results 34
3.3.2. Collective Evaluation of Stimulation Thresholds and Pulse Duration Dependencies 41
3.4. Discussion 44
3.5. Limitations 47

3.6. Conclusion 48
Chapter 4 Ventricular Fibrillation Induction Characteristics 49
4.1. Introduction 49
4.2. Research Question 54
4.3. Methods 55
4.3.1. Subcutaneous Ventricular Fibrillation Induction Testing Preparation 55
4.3.2. Subcutaneous Ventricular Fibrillation Testing Method 56
4.4. Results 56
4.4.1. Subject-Specific VF Induction Threshold 56
4.4.2. Effects of Pulse Width and Frequency on Stimulation Current Requirements. 66
4.5. Discussion: 71
4.5.1. Clinical Implications of Subcutaneous VF Induction Thresholds 71
4.6. Limitations 74
4.7. Conclusion 75
Chapter 5 Maturation of Human Induced Pluripotent Stem Cells 76
5.1. Introduction 76
5.2. Defining Maturation Metrics 78
5.2.1. Muscle Contraction 78
5.2.2. Pacemaker Function 79
5.2.3. Electrical Coupling 81
5.2.4. Calcium Handling 82
5.2.5. Electrical Conditioning Framework 84
5.3. Research Question 86
5.4. Methods 87
5.4.1. Generation and Preparation of Human-Induced Pluripotent Stem Cell-Derived Cardiomyocytes 87
5.4.2. Electrical Stimulation Test Method and Protocol 88

5.5. Results 91
5.5.1. Experimental design and viable dataset 91
5.5.2. Raw transcriptional dataset overview 93
5.5.3. Z-Score Transformation and standardised dataset 94
5.5.4. Principal component analysis of the standardised transcriptional dataset 95
5.5.5. Main effects linear regression models 97
5.6. Discussion 98
5.6.1. Principal findings 98
5.6.2. Electrical stimulation as a modulator of coordinated maturation 99
5.6.3. Distributed Transcriptional organisation versus dominant gene regulation 100
5.6.4. Electrophysiological and Gap Junction Regulation 101
5.6.5. Simplified Engineered Tissue Context and Limits of Maturation 101
5.6.6. Implications for waveform optimisation and bioelectrical design constraints 102
5.7. Limitations 103
5.8. Conclusion 103
Chapter 6 General Discussion and Conclusion 105
6.1. Overview and Integrative Perspective 105
6.1.1. Objective 1: Development of a Programmable Waveform Platform 106
6.1.2. Objective 2: Subcutaneous Pacing Threshold Characteristics 107
6.1.3. Objective 3: Waveform Modulation of Ventricular Fibrillation Induction 108
6.1.4. Objective 4: Waveform-Dependent Maturation of hiPSC-Derived Cardiomyocytes. 112
6.2. Future Works 115
Bibliography 117

Table of Abbreviations

Acronyms	Explanation
ACTA2	Actin alpha 2, smooth muscle
APHRS	Asia Pacific Heart Rhythm Society
ATP	Anti-tachycardia pacing
ATP2A2	ATPase sarcoplasmic/endoplasmic reticulum Ca^{2+} transporting 2; gene encoding SERCA2
AWG	Arbitrary waveform generator
B27	B27 cell culture supplement
BPM	Beats per minute
C59	Wnt pathway inhibitor used during cardiomyocyte differentiation
CACNA1C	Calcium voltage-gated channel subunit alpha 1C
Ca^{2+}	Calcium ion
CI	Confidence interval
CIED	Cardiac implantable electronic device
CIMA	Centro de Investigación Médica Aplicada
CM	Cardiomyocyte
COL1A1	Collagen type I alpha 1 chain
CO_2	Carbon dioxide
CRT	Cardiac resynchronisation therapy
CWG	Custom Waveform Generator
Cx40	Connexin 40
Cx43	Connexin 43
CVD	Cardiovascular disease
DC–DC	Direct-current to direct-current converter
DDR2	Discoidin domain receptor tyrosine kinase 2
DFT	Defibrillation threshold testing
DOE	Design of Experiments
ECG	Electrocardiogram / electrocardiography
EFFORTLESS	EFFORTLESS S-ICD Registry
ELN	Engineering Laboratory Notebook

EMBLEM	Boston Scientific EMBLEM S-ICD platform
EMC	Electromagnetic compatibility
EHRA	European Heart Rhythm Association
EMPOWER	EMPOWER leadless pacemaker / clinical trial platform
ES	Electrical stimulation
$EtCO_2$	End-tidal carbon dioxide
EV-ICD	Extravascular implantable cardioverter-defibrillator
FFR	Force-frequency relationship
GJA1	Gap junction protein alpha 1; gene encoding connexin 43
GJA5	Gap junction protein alpha 5; gene encoding connexin 40
GLM	General linear model
GSK3	Glycogen synthase kinase 3
GUI	Graphical user interface
HCN4	Hyperpolarisation-activated cyclic nucleotide-gated channel 4
hiPSC	Human induced pluripotent stem cell
hiPSC-CM	Human induced pluripotent stem cell-derived cardiomyocyte
HRS	Heart Rhythm Society
IACUC	Institutional Animal Care and Use Committee
ICD	Implantable cardioverter-defibrillator
IEC	International Electrotechnical Commission
IK1	Inward rectifier potassium current
ISO	International Organization for Standardization
ISO/IEC	International Organization for Standardization / International Electrotechnical Commission
KCNJ2	Potassium inwardly rectifying channel subfamily J member 2
KSR	KnockOut Serum Replacement
Li-MnO_2	Lithium manganese dioxide
mA	Milliampere
MHC	Myosin heavy chain
MI	Myocardial infarction
MLC2a	Myosin light chain 2 atrial isoform

MLC2v	Myosin light chain 2 ventricular isoform
MOSFET	Metal-oxide-semiconductor field-effect transistor
MYH6	Myosin heavy chain 6
MYH7	Myosin heavy chain 7
MYH7/MYH6	Ratio of MYH7 to MYH6 expression
MYL2	Myosin light chain 2
MYL7	Myosin light chain 7
MYL2/MYL7	Ratio of MYL2 to MYL7 expression
NA	Not available / not applicable
NORDIC	NO Regular Defibrillation testing In Cardioverter Defibrillator Implantation trial
NSR	Normal sinus rhythm
PC1	Principal component 1
PC2	Principal component 2
PC3	Principal component 3
PCA	Principal component analysis
PRAETORIAN	Prospective Randomized Comparison of Subcutaneous and Transvenous Implantable Cardioverter Defibrillator Therapy trial
PRAETORIAN-DFT	PRAETORIAN defibrillation testing trial
PW	Pulse width
qPCR	Quantitative polymerase chain reaction
R^2	Coefficient of determination
ROCK	Rho-associated protein kinase
RPMI	Roswell Park Memorial Institute medium
RYR2	Ryanodine receptor 2
SCA	Sudden cardiac arrest
SCD	Sudden cardiac death
S-ICD	Subcutaneous implantable cardioverter-defibrillator
SCN5A	Sodium voltage-gated channel alpha subunit 5
SD	Standard deviation
SERCA2a	Sarcoplasmic/endoplasmic reticulum Ca^{2+} ATPase 2a
SHOX2	Short stature homeobox 2

SIMPLE	Shockless IMPLant Evaluation trial
SOLAECE	Sociedad Latinoamericana de Estimulación Cardíaca y Electrofisiología (Latin American Society of Cardiac Pacing and Electrophysiology).
SR	Sarcoplasmic reticulum
SD	Standard deviation
TNNI1	Troponin I1, slow skeletal type
TNNI3	Troponin I3, cardiac type
TNNI3/TNNI1	Ratio of TNNI3 to TNNI1 expression
USB	Universal Serial Bus
VF	Ventricular fibrillation
VT	Ventricular tachycardia
WHO	World Health Organisation
Y-27632	ROCK inhibitor used to support cell survival

List of Symbols

Symbols	Explanation	Units
$\Delta E_{ele}c$	Interfacial potential of the bipolar electrode	V
I	Threshold current required to achieve capture / stimulation current	mA
I_{rh}	Rheobase current; minimum asymptotic current required for capture	mA
τc	Chronaxie; pulse width at which threshold current equals twice the rheobase	ms
PW	Pulse width	ms
T	Period of stimulation	ms or s
f	Stimulation frequency	Hz
Duty cycle	Fraction of each stimulation cycle during which current is delivered	%
Iavg	Average current over the stimulation pulse train	mA
Ipeak	Peak stimulation current	mA
zij	z-score for endpoint j in run i	Dimensionless
xij	Raw normalised value for endpoint j in run i	Endpoint-specific
μj	Mean value of endpoint j across viable runs	Endpoint-specific
σj	Standard deviation of endpoint j across viable runs	Endpoint-specific
i	Run index within the DOE dataset	Dimensionless
j	Endpoint / variable index within the DOE dataset	Dimensionless
ΔCt	Difference in qPCR cycle threshold between target and reference genes	Cycles
ΔΔCt	Difference between sample ΔCt and calibrator/control ΔCt	Cycles
2^-ΔΔCt	Relative normalised gene-expression value	Dimensionless
n	Number of replicates, animals, constructs, or observations depending on context	Dimensionless
N	Number of observations or replicate measurements	Dimensionless
SD	Standard deviation	Variable-specific
±SD	Mean plus/minus standard deviation	Variable-specific
CI	Confidence interval	Variable-specific
95% CI	95% confidence interval	Variable-specific

p	Probability value / statistical significance value	Dimensionless
F	F-statistic from general linear model or ANOVA-type testing	Dimensionless
R^2	Coefficient of determination; proportion of variance explained by a model	Dimensionless
Pred R^2	Predicted coefficient of determination	Dimensionless
α	Alpha isoform designation, e.g. α-myosin heavy chain	Dimensionless
β	Beta isoform designation, e.g. β-myosin heavy chain	Dimensionless
$EtCO_2$	End-tidal carbon dioxide	mmHg or % depending on monitor setting
Ω	Ohm; unit of electrical resistance or impedance	Ω
V	Voltage / electrical potential	V
mA	Milliampere; unit of electrical current	mA
A	Ampere; unit of electrical current	A
Ah	Ampere-hour; battery capacity	Ah
W	Watt; electrical power	W
Hz	Hertz; frequency in cycles per second	Hz
ms	Millisecond; pulse duration or time interval	ms
s	Second; time	s
min	Minute; time	min
h	Hour; time	h
d	Day; duration of culture or stimulation	days
V/cm	Electric field strength	V/cm
V cm^{-1}	Electric field strength; preferred formatted form of V cm-1	V cm^{-1}
µm	Micrometre; microscopic length scale	µm
mm	Millimetre; length	mm
mm^2	Square millimetre; area	mm^2
µL	Microlitre; fluid volume	µL
mL	Millilitre; fluid volume	mL
µM	Micromolar concentration	µM
µg/mL	Microgram per millilitre; mass concentration	µg/mL
mg/kg	Dose normalised to body mass	mg/kg
mg/kg/h	Infusion rate normalised to body mass and time	mg/kg/h
°C	Temperature in degrees Celsius	°C

List of Figures

Figure 1. Representative configuration of a conventional transvenous cardiac implantable electronic device system. (A) Schematic illustrating transvenous leads positioned in the right atrium and right ventricle, with a left ventricular pacing lead advanced through the coronary sinus. (B) Represents a transvenous systems complete with pulse generator, and associated leads providing direct intracardiac sensing and therapy delivery. 4

Figure 2. Representative configuration of a subcutaneous implantable cardioverter-defibrillator (S-ICD) system. (A) Schematic illustrating the entirely extravascular configuration, with the defibrillation electrode positioned along the parasternal region and the pulse generator implanted in the lateral thoracic position. (B) Representative Boston Scientific EMBLEM™ MRI S-ICD pulse generator and subcutaneous electrode..... 5

Figure 3. Representative configuration of an extravascular implantable cardioverter-defibrillator (EV-ICD) system. (A) Schematic illustrating the extravascular configuration, with the defibrillation electrode positioned in the substernal space and the pulse generator implanted in the lateral thoracic region. (B) Representative Medtronic Aurora EV-ICD™ pulse generator and substernal electrode. 5

Figure 4. Integrated experimental framework illustrating the development of a programmable waveform generator and its applications in in vivo subcutaneous pacing and ventricular fibrillation induction studies, with subsequent translation to in vitro hiPSC-CMs conditioning. The framework highlights how stimulation parameters were examined across organ-level electrophysiological outcomes and cellular-level maturation- relevant transcript responses. 10

Figure 5. Definition of stimulation waveform architecture and associated timing parameters used throughout this study. Monophasic (A), biphasic (B), and biphasic with interphase delay (C) waveforms are shown. Key temporal parameters are defined as: A, period; B, pulse width; C, inter-pulse delay; D, interphase delay. 16

Figure 6. System-level architecture of the Custom Waveform Generator (CWG). The diagram illustrates the microcontroller-driven control framework, galvanically isolated power delivery, and H-bridge output stage enabling programmable monophasic and biphasic stimulation. The modular design supports both high-current subcutaneous stimulation and low-voltage in vitro applications. 19

Figure 7. Physical implementation and experimental validation of the CWG platform per configuration type. (A) In vivo CWG enclosure designed for high-current subcutaneous stimulation. (B) In vitro CWG enclosure for low-voltage tissue stimulation. (C) Internal

architecture of the in vivo system showing boost converter, current regulation, and switching stage. (D) Internal layout of an in vitro system integrating Arduino control and MOSFET H-bridge driver. (E) Representative monophasic waveform output. (F) Representative monophasic and biphasic waveforms. 20
Figure 8. Graphical user interface (GUI) for real-time control, configuration, and monitoring of stimulation protocols. Custom-developed interface allowing user-defined configuration of waveform parameters, including pulse amplitude, width, interphase delay, frequency, and duration. The GUI also supports calibration routines. 24
Figure 9. Surgical access and electrode configuration in the porcine model. Representative image illustrating subject positioning in dorsal recumbency with completed transvenous and subcutaneous instruments. The right jugular venous cutdown enabled transvenous placement of a right ventricular ICD lead. An S-ICD electrode was implanted along the right parasternal margin via a subxiphoid tunnelling approach. A non-functional subcutaneous generator was positioned in the right lateral thorax to complete the coil-to-can vector, consistent with clinical device configurations. 33
Figure 10. Strength-duration curves for SW6022 show mean threshold current (mA) as a function of pulse width (ms) for monophasic stimulation. Data points represent the mean ± 95% CI at each pulse width. These plots illustrate the relationship between stimulus duration and excitability. 36
Figure 11. Strength-duration curves for SW6045 showing mean threshold current (mA) as a function of pulse width (ms) for pooled monophasic and biphasic stimulation. Data points represent the mean ± 95% CI at each pulse width. Solid blue line connects the means of each threshold curve. The dashed orange line indicates the fitted Weiss-Lapicque model, from which the rheobase and chronaxie values were derived. 38
Figure 12. Strength-duration curves for SW6047 showing mean threshold current (mA) as a function of pulse width (ms) for pooled monophasic and biphasic stimulation. Data points represent the mean ± 95% CI at each pulse width. Solid blue line connects the means of each threshold curve. The dashed orange line indicates the fitted Weiss-Lapicque model, from which the rheobase and chronaxie values were derived. 40
Figure 13. Strength-duration curve for SW6054, monophasic only. Data points represent single measurements at each pulse width. The dashed line is the Weiss-Lapicque fitted strength-duration curve. 41
Figure 14. Strength-duration characteristics of subcutaneous pacing in four swine. Symbols represent mean threshold current at each pulse width (1-10 ms), error bars are 95% CIs where replicate trials were available (n=1-4 per condition, no error bars n=1). Dashed curves are

Weiss-Lapicque fitted curves, Equation 4, yielding the rheobase Irh (mA) and chronaxie τc (ms). Thresholds fall steeply from 1-4 ms and approach an asymptote at longer pulse durations, demonstrating classical excitability behaviour with marked between-animal variability. For SW6045 and SW6047, monophasic and biphasic data were pooled because the waveforms showed no significant impact on threshold (p=0.926, GLM Pooled). 42
Figure 15. Relationship between waveform parameters and VF induction thresholds in SW6022. (A) Mean peak current (± 95% CI) vs stimulation frequency grouped by pulse width. (B) Corresponding average current (± 95% CI). Longer pulse widths and higher frequencies lowered peak current while increasing average current. 60
Figure 16. Relationship between waveform parameters and VF induction thresholds in SW6045. (A) Mean peak current (± 95% CI) vs stimulation frequency grouped by pulse width. (B) Corresponding average current (± 95% CI). Data represent 3-5 replicates per condition. 63
Figure 17. Relationship between waveform parameters and VF induction thresholds in SW6047. (A) Mean peak current (± 95% CI) vs stimulation frequency grouped by pulse width. (B) Corresponding average current (± 95% CI). 66
Figure 18. Average Current (A) Main Effect plots show how pulse width and frequency affect average current. Increasing pulse width significantly increases average current, whereas frequency has a smaller effect. (B) Half-Normal plot highlights the significant factors, with pulse width being the main contributor to average current, followed by frequency. (C) The interaction plot shows how pulse width affects average current across different frequencies. The nearly parallel lines suggest minimal interaction, confirming the additive effect of pulse width and frequency. (D) Response surface contour plot displays the combined influence of pulse width and frequency on average current, with both increasing the current, but pulse width being the more dominant factor. (E) Predicted versus actual plot shows a strong match between model predictions and observed values, confirming the model's validity. 68
Figure 19. Peak Current (A) Main Effect plots showing the influence of pulse width and frequency on peak current. Increasing pulse width substantially reduces peak current, whereas frequency has a lesser effect. (B) Half-Normal plot identifying statistically significant factors. Pulse width is the dominant contributor to peak current, followed by frequency. (C) Interaction plot illustrating the effect of pulse width on peak current at different frequencies. The near-parallel trends indicate minimal interaction between pulse width and frequency. (D) Response surface contour plot illustrating the combined effects of pulse width and frequency on peak current. Both parameters decrease peak current, with

pulse width exerting the dominant influence. (E) Predicted versus actual plot demonstrating strong agreement between model predictions and observed values, confirming model validity. 70

Figure 20 Custom electrical stimulation platform used for conditioning engineered hiPSC-CM tissues. (A) Schematic of the bioreactor chamber showing two parallel carbon rod electrodes positioned 20 mm apart and a tissue holder maintaining four constructs at equal spacing between the electrodes; schematic not to scale. (B) Photograph of the 3D-printed stereolithography tissue holder. (C) Representative image of the stimulation configuration with electrodes immersed in culture medium. (D) Representative photograph of the assembled stimulation platform and instrument connections. 90

Figure 21. Distribution of DOE conditions in voltage–pulse width space with viability status indicated. Each point represents one programmed stimulation condition from the 16-run design. Viable conditions retained for downstream analysis are shown in green, and non-viable conditions excluded from analysis are shown in red. Frequency and waveform type were also varied within the DOE but are not displayed in this two-dimensional projection. 92

Figure 22. Principal component analysis of the standardised transcriptional dataset. (A) Colour-coded summary of loading values for principal components 1 and 2 across the 18 directly measured transcripts and 3 derived maturation-associated expression ratios included in the analysis. (B) Scree plot showing the eigenvalue spectrum across successive principal components. (C) Loading plot showing the relative orientation and contribution of variables in PC1–PC2 space. PCA was performed on the z-scored dataset using the correlation matrix; the first three principal components accounted for 72.0% of the total variance. 96

List of Tables

Table 1. Functional design requirements for the dual-mode CWG derived from design inputs. Requirements are defined to support both high-current subcutaneous stimulation and low-voltage in vitro pacing conditions. 17

Table 2. Summary of current regulation performance across operating ranges. Maximum positive and negative deviations and standard deviation of output current are reported for programmed step changes of 10-400 mA across representative loads of 12.5-250 Ω. 25

Table 3. Subcutaneous pacing thresholds in SW6022 as a function of pulse width. Mean peak current required for capture is shown as mean ± SD with corresponding 95% confidence intervals (CI). Each pulse width was tested with 3-4 replicates per condition. 35

Table 4. Subcutaneous pacing thresholds in SW6045 as a function of pulse width. Mean peak capture current is shown as the mean ± SD, with the corresponding 95% confidence interval (CI). Each pulse width was tested with 1-3 replicates per condition 37

Table 5. Subcutaneous pacing threshold in SW6047 as a function of pulse width. Mean peak current required for capture is shown as mean ± SD with corresponding 95% confidence intervals (CI).. Each pulse width was tested 1-3 replicates per condition. 39

Table 6. Subcutaneous pacing thresholds in SW6054 as a function of pulse width. Each pulse width was tested once; therefore, variability metrics (SD and 95% CI) could not be calculated 40

Table 7. Subject-specific rheobase and chronaxie for subcutaneous pacing. Rheobase (mA) and chronaxie (ms) were estimated from Weiss-Lapicque fits to each animal's strength-duration data, with pulse widths ranging from 1 to 10 ms. Values illustrate marked intersubject variability and an inverse pattern between rheobase and chronaxie. For SW6045 and SW6047, monophasic and biphasic data demonstrated no significant impact on threshold, with p-values of 0.93 and 1.0, respectively**.** 43

Table 8. Mean Peak current (mA) required for VF induction in SW6022 as a function of pulse width (ms) and frequency (Hz). Values shown as mean ±95% CI; n=1-4 replicates per condition 59

Table 9. Mean Average currents (mA) during VF-induction pulse trains in SW6022. Values shown as mean ±95% CI, for each pulse width (ms) and frequency (Hz) combination (n =2-4). Average current is the time-averaged current over the pulse train. 59

Table 10. Mean peak currents (mA) required for VF induction in SW6045 across varying pulse widths (ms) and stimulation frequencies (Hz). Values are presented as mean ±95% CI;

n=3-5 replicates per condition. Conditions at 1 ms and 10 Hz were excluded because peak currents exceeded 400 mA. 62
Table 11. Mean average current (mA) per pulse train in SW6045 for each pulse width (ms) and frequency (Hz). Values are mean ±95% CI; n=3-5. Average current increases with pulse width and frequency. 62
Table 12. Peak current (mA) required for VF induction in SW6047 across varying pulse widths (ms) and frequencies (Hz). Data represent mean ± 95% CI; n = 2-3 per condition otherwise specified. Measured currents ≥400 mA were excluded from analysis due to measurement limits 64
Table 13. Mean average current (mA) required for VF induction in SW6047 across pulse width (ms) and frequency (Hz) conditions. Data are reported as ± 95% CI, with median, minimum, maximum, and standard deviation included. Average current indicates the time-averaged current delivered during waveform exposure and provides insights into potential power consumption, energy delivery, and implications for device battery life. 64
Table 14. Representative studies of electrical stimulation used to promote cardiomyocyte maturation. The table summarises stimulation parameters, experimental models, and reported biological outcomes across selected studies using hiPSC-derived or neonatal cardiomyocytes. Because waveform configuration, culture format, and stimulation geometry differ across studies, direct comparison of amplitudes and biological outcomes should be made with caution. Amplitude values are reported as presented in the original sources. ... 85
Table 15. Stimulus configurations used in the 16-run DOE and their analysis status. The table lists voltage, pulse width, frequency, waveform type, and whether each condition was retained or excluded from downstream analysis. Each condition was represented by four tissue constructs (n = 4) within a single experimental run; independent repeat runs were not performed. 92
Table 16: Selected ranges of raw normalised transcript and ratio endpoints across viable runs (n = 13) 94
Table 17. Summary of general linear model (GLM) results for PC1, PC2, and MYL2/MYL7. Reported values include model R^2, overall regression p-values, predictor-level p-values, and lack-of-fit p-values. All p-values are shown as nominal values, as no multiple-testing correction was applied in the reported GLM outputs. 98

Research Outputs

Publications

1. P.Bennett, S. J.Hahn, and S.Daniels, “Strength-Duration Characterisation of Subcutaneous Pacing: A Preclinical Study.” Pacing and Clinical Electrophysiology (2026): . https://doi.org/10.1111/pace.70256

Manuscripts Under Review

1. P. Bennett, S. J. Hahn, and S. Daniels, “Waveform Configuration Influences Ventricular Fibrillation Induction Thresholds in Subcutaneous Implantable Cardioverter Defibrillator Systems: A Preclinical Study.” Heart Rhythm O2 (submitted; under review).

Oral Presentations

1. Global Technology Expo (GTE), Boston Scientific, 2022
   Development of electro-mechanical stimulation systems for the in vitro maturation of hiPSC-derived cardiac tissue as part of the EU Horizon 2020 BRAV3 project.

2. Global Technology Expo (GTE), Boston Scientific, 2024
   Electro-anatomical modelling and electrical stimulation approaches for cardiac tissue maturation in a BioVAD bioreactor system (BRAV3 Horizon 2020 collaboration).

3. BRAV3 Consortium Research Symposium, Madrid, 2025
   Electrical stimulation–driven maturation of engineered cardiac tissue: system design, experimental outcomes, and translational considerations.

Poster Presentations

1. Global Technology Expo (GTE), Boston Scientific, 2022
   Author of a poster on “Engineered hiPSC-derived cardiomyocytes: electro-mechanical conditioning strategies for regenerative cardiac support (EU Horizon 2020 BRAV3).”

2. Global Technology Expo (GTE), Boston Scientific, 2024
   Author of a poster on “Electrical stimulation and bioreactor-based maturation of human induced pluripotent stem cell–derived cardiac tissue for BioVAD applications.”

3. EU Horizon 2020 BRAV3 Research Dissemination Showcase, 2024–2025
4. Poster contributions on electrical stimulation systems and maturation metrics for engineered myocardial constructs.

Research proposals & competitive submissions

Plug-and-Beat – Horizon Europe proposal (Application ID: 101291634)
Joint author and technical contributor to a competitive EU research-to-innovation proposal developed with Leartiker and BRAV3 consortium partners.
The proposal focused on the translation of electro-mechanical stimulation and bioreactor systems for engineered cardiac tissue, building on outcomes from the EU Horizon 2020 BRAV3 project

Ethics and Regulatory Approval

Ethics Approval: All animal procedures were approved by the Boston Scientifics, Institutional Animal Care and Use Committee (IACUC) Protocol #17-082N and conformed to Directive 2010/63/EU

Patient Consent: Not applicable

Clinical Trial Registration: Not applicable

Data Availability and Supporting Evidence

The supporting datasets and appendix files generated during this doctoral research have been deposited in Zenodo to support transparency, traceability, reproducibility and long-term preservation of the work.[1] The repository contains the raw and processed datasets underlying the experimental chapters of this thesis, together with the associated statistical reports and native analysis files where available. These files support Chapters 2–5 and include custom waveform generator characterisation data, subcutaneous pacing threshold measurements, ventricular fibrillation induction datasets, design-of-experiments files, qPCR-derived transcriptional datasets, z-scored datasets, principal component analysis outputs and general linear model outputs.

The repository includes native analysis files, spreadsheet workbooks and exported statistical reports. These materials are intended to allow the reader to trace the experimental measurements, data processing steps and statistical analyses reported in the thesis. Proprietary analysis files, including Minitab and Design-Expert project files, are included to preserve the original workflows; where possible, accompanying spreadsheet or document-based exports are also provided to support accessibility. No patient-identifiable data are included in the repository. Animal and biological experimental data should be interpreted in accordance with the ethical approvals, institutional governance and experimental limitations described in the relevant thesis chapters.

File / appendix	Thesis chapter supported	Contents
Appendix 1 Chapter 2 Raw Data.xlsx	Chapter 2	Raw data for custom waveform generator characterisation, including pulse width testing and pulse amplitude testing.
Appendix 2 Chapter 2 CWG characterisation testing.docx	Chapter 2	Characterisation test report for the custom waveform generator, including test article, firmware reference, test loads, oscilloscope/DMM setup, equipment details and testing protocol. The report identifies CWG characterisation testing and includes pulse timing and pulse amplitude testing procedures.
Appendix 3 Chapter 3 Raw Data.xlsx	Chapter 3	Raw data supporting subcutaneous pacing threshold analysis.
Appendix 4 Chapter 3 SW6045 Mono Vs Biph.docx	Chapter 3	General linear model output for subject SW6045 comparing threshold current against waveform

		and pulse width. The report shows pulse width had a significant effect on threshold, while waveform type did not.
Appendix 5 Chapter 3 SW6047 Mono Vs Biph.docx	Chapter 3	General linear model output for subject SW6047 comparing threshold current against waveform and pulse width. The report similarly shows a strong pulse-width effect and no waveform-type effect.
Appendix 6 Chapter 3 Biphasic Vs Monophasic Waveforms.docx	Chapter 3	Combined subject-level GLM comparing waveform, pulse width and subject effects across SW6045 and SW6047.
Appendix 7 Chapter 4 Raw Data.xlsx	Chapter 4	Raw ventricular fibrillation induction threshold data.
Appendix 8 Chapter 4 VF DOE.dxpx	Chapter 4	Design-Expert DOE project file supporting Chapter 4 ventricular fibrillation waveform optimisation analysis.
Appendix 9 Chapter 5 Statistical Report.docx	Chapter 5	Statistical output for Chapter 5, including PCA, eigenanalysis, GLM outputs and transcriptional modelling of hiPSC-CM maturation-associated endpoints. The report includes PCA eigenvalues showing PC1 accounting for 35.8% and PCs 1–3 accounting for 72.0% cumulative variance.
Appendix 10 Chapter 5 Raw Data.xlsx	Chapter 5	Raw and organised hiPSC-CM qPCR/transcriptional data, including transformed datasets and Minitab-ready data sheets.
Appendix 11 Chapter 5 Minitab-DOEscomplete.mpx	Chapter 5	Native Minitab project file containing DOE and statistical analysis workflows for Chapter 5.
Appendix 11 Chapter 5 Raw Data REV B.xlsx	Chapter 5	Revised Chapter 5 raw data workbook supporting the final transcriptional analysis dataset.
Appendix 12 Regression Analysis PC1 versus Voltage, PW, Frequency, Type.docx	Chapter 5	Regression analysis of PC1 against voltage, pulse width, frequency and waveform type. The model output reports PC1 regression statistics, coefficients, R^2 and predictor p-values.
Appendix 13 Regression Analysis MYL2_MYL7 versus Voltage, PW, Frequency, Type.docx	Chapter 5	Regression analysis of the MYL2/MYL7 ratio against voltage, pulse width, frequency and waveform type, including model coefficients, R^2, lack-of-fit testing and residual diagnostics.

Abstract

Electrical Waveform Configuration Across Cardiac Scales: Effects on Subcutaneous Myocardial Excitation, Ventricular Fibrillation Induction, and hiPSC-CM Maturation-Relevant Transcriptional Responses

Current methods of subcutaneous post-shock pacing and subcutaneous ventricular fibrillation induction rely on fixed waveform configurations. While these approaches yield high efficacy in therapy delivery, they do not optimise waveforms to accommodate patient comfort or the delivered energy.

This study aimed to characterise, in a pre-clinical setting, the cardiac response to subcutaneous pacing thresholds as a function of pulse width and amplitude. The data enabled the generation of strength-duration curves, from which rheobase and chronaxie values were derived for each animal. Although capture currents were significantly higher than those required for conventional endocardial pacing, reliable myocardial capture was consistently achieved. The characterisation data align with classical electrophysiological strength-duration hyperbolic responses.

Building on these findings, the study implemented a design-of-experiments framework to assess the impact of waveform parameters on the effectiveness of ventricular fibrillation induction. The results indicated that successful induction is largely dependent on specific waveform settings. Longer pulse durations and higher frequencies lowered the peak current required for induction but increased the average current. These results reveal important trade-offs between stimulation efficiency and device energy consumption.

Finally, waveform parameters were evaluated as potential cues for transcriptional organisation in engineered cardiac microtissues. A design-of-experiments structure was implemented, using quantitative polymerase chain reaction to assess waveform-associated changes in the expression of maturation-relevant cardiac genes.

This thesis demonstrated that waveform configuration is an important design variable influencing cardiac capture and arrhythmia induction in vivo and is associated with maturation-relevant transcriptional responses in hiPSC-CM constructs in vitro. These findings have implications for the optimisation of S-ICD-related stimulation strategies and electrical conditioning approaches in cardiac tissue engineering.

Chapter 1 : Clinical Rationale and Research Framework for Cardiac Waveform Optimisation

1.1.Introduction and Research Motivation

1.1.1. Global Burden of Cardiovascular Disease

Cardiovascular disease (CVD) continues to be the primary cause of global mortality. The World Health Organisation (WHO) estimate 19.8 million deaths occur annually due to CVD, accounting for approximately 32% of all global deaths. Of these deaths, the majority are attributed to ischaemic heart disease and stroke, which together account for approximately 85% of all CVD-related mortality.[2]

The global burden of CVD also includes considerable illness, disability, and economic impacts. According to Palaniappan et al. in the 2026 Heart Disease and Stroke Statistics Update Fact Sheet, more than 600 million people are affected by cardiovascular diseases. These figures reflect the combined influence of population growth, ageing populations, and increased exposure to modifiable risk factors such as hypertension, obesity, diabetes, and sedentary lifestyles.[3]

Sudden cardiac arrest (SCA) represents the most catastrophic consequence of cardiovascular disease. If blood flow is not restored promptly, SCA may progress to sudden cardiac death (SCD). SCD, as detailed by Zipes and Wellens, is described as the unexpected natural death from a cardiac cause within a short period. SCD is often attributed to a cardiac arrhythmia.[4] These arrhythmias include ventricular tachycardia (VT) and ventricular fibrillation (VF). A typical healthy heart beats between 60 and 100 beats per minute (bpm), depending on the physical demand. In VT, the heart rate will typically exceed 100 bpm. VT is classified according to its duration. Less than 30 s is classified as non-sustained, and greater than 30 s is classified as sustained. Sustained VTs, if not treated by cardioversion or anti-tachycardia pacing, can result in syncope or cardiac arrest.[5] An untreated VT can progress to VF. VF is a ventricular arrhythmia causing the heart to beat much faster than normal. Heart rates exceeding 300 bpm are not uncommon. This has a significant impact on the heart's efficiency to pump blood. The ventricles begin to quiver, making them incapable of contracting. As a result, the quantity of blood pumped to the body from the heart is largely impeded. VF is a life-threatening arrhythmia requiring immediate defibrillation to preserve life.[6] As such, preventing SCD has become a key objective in modern cardiovascular medicine.

Sudden cardiac arrest is commonly conceptualised as an electrical failure of the heart, whereas acute myocardial infarction is primarily a vascular event caused by obstruction of

coronary blood flow.[7] Myocardial infarction (MI) remains a major contributor to cardiovascular morbidity and mortality. During myocardial infarction, obstruction of coronary blood flow causes rapid ischaemic injury and irreversible cardiomyocyte death.[8] Research indicates that more than one billion cardiomyocytes can be lost during a large myocardial infarction.[9] Consequently, this triggers a cascade of inflammatory and fibrotic remodelling processes that ultimately result in scar formation, impaired ventricular function, and an increased risk of cardiovascular arrhythmia.[10]

The human heart, unlike other organs, has a limited capacity to regenerate.[11] After MI, necrotic myocardium is typically replaced by fibrotic tissue rather than new contractile cells.[9] This loss of healthy myocardium leads to progressive ventricular dysfunction and is a key contributor to chronic heart failure.[11] Although there have been substantial advances in drug therapy, interventional cardiology, and implantable cardiac devices, these approaches are largely compensatory rather than restorative. Electrical therapies, such as cardiac pacing and defibrillation, can re-establish rhythm but do not regenerate myocardium.[8] While pharmacological management primarily targets haemodynamic and neurohormonal pathways, there remains a considerable unmet clinical need for therapies capable of preventing deadly arrhythmias and regenerating functional myocardial tissue post-injury.

The global burden of cardiovascular disease has driven extensive research across various disciplines, including cardiac electrophysiology, device engineering, and regenerative medicine.[11,12] Next-generation therapeutics aim to target the root causes of cardiovascular disease and its consequences. To facilitate this, an improved comprehension of the interactions between electrical signals and cardiac tissue at both organ and cellular levels will be required.

1.2.Electrical Stimulation in Cardiovascular Medicine

Cardiac rhythm depends on the orderly and highly regulated generation and propagation of electrical impulses through specialised myocardial tissue.[13] Heart rate is controlled by two branches of the autonomic nervous system, the sympathetic and parasympathetic systems. These systems increase or decrease the heart rate to meet cardiovascular demand by modulating the heart's electrical activity.[14] Intrinsic electrical impulses generated by specialised pacemaker cells in the sinoatrial node initiate the cardiac cycle and determine the heart rate. These impulses propagate through the atrioventricular conduction system, through the atrioventricular node, before passing into the HIS bundle, the right and left bundle branches, and finally the Purkinje fibre network. This sequence of events coordinates ventricular depolarisation and contraction. This electrical conduction network synchronises excitation-contraction coupling throughout the heart and ensures effective haemodynamic

function.[15] Disruption of this electrical signalling system can result in brady-arrhythmias, conduction block or malignant ventricular tachyarrhythmias that compromise cardiac output and may culminate in SCD.[15]

The delivery of controlled electrical stimulation has become a central therapeutic strategy in cardiovascular medicine, enabling the restoration of rhythm, the prevention of lethal arrhythmias, and the modulation of cardiac function via active implantable devices.[16–18]

The interaction between electrical energy and excitable biological tissue has been studied for over 130 years.[16] Early physiological studies demonstrated that electrical stimulation could induce contractions in skeletal and cardiac muscle. These observations formed the scientific basis of electrotherapy, which eventually led to the development of cardiac pacing technologies in the mid-twentieth century.[16,17,19,20] The first implantable pacemaker, introduced in 1958, enabled long-term treatment of bradyarrhythmias. Implantable pacemakers deliver electrical impulses at regular intervals to the myocardium, restoring a physiological heart rate in patients with conduction system disease.[16,17,21] Since then, implantable electrical therapies have expanded considerably and now include cardiac resynchronisation therapy (CRT), anti-tachycardia pacing (ATP) and high-energy defibrillation delivered by implantable cardioverter defibrillators (ICDs). Collectively, these therapies represent one of the most successful applications of bioelectronic medicine and have significantly reduced mortality in patients with life-threatening cardiac arrhythmias.[22]

In pacing systems, low-energy pulses are delivered to the endocardium to stimulate myocardial depolarisation when intrinsic conduction is impaired. In contrast, defibrillation therapy requires the delivery of high-energy electrical shocks that simultaneously depolarise a critical mass of myocardium, terminating ventricular fibrillation or unstable ventricular tachycardia. The electrophysiological response to these stimuli depends on complex interactions among waveform characteristics, electrode geometry, tissue impedance, and myocardial excitability. Classical electrophysiological models, including strength-duration relationships described by Lapicque and Weiss, demonstrate that excitation thresholds are determined by both stimulation amplitude and pulse duration, highlighting the importance of waveform configuration in determining stimulation efficacy.[23–25]

Conventional transvenous pacing and defibrillation systems, as detailed in **Figure 1**, rely on leads implanted in the venous system to sense intrinsic activity and deliver electrical therapy as required.[26] While these systems provide life-enhancing and life-saving therapies, they also carry risks. Clinical registry data continue to detail the potential complications associated with transvenous systems. The documented risks are non-trivial and include infection, venous obstruction, lead fracture, and complications during explant. These issues have

prompted the development of alternative device designs that avoid transvenous lead placement.[12]

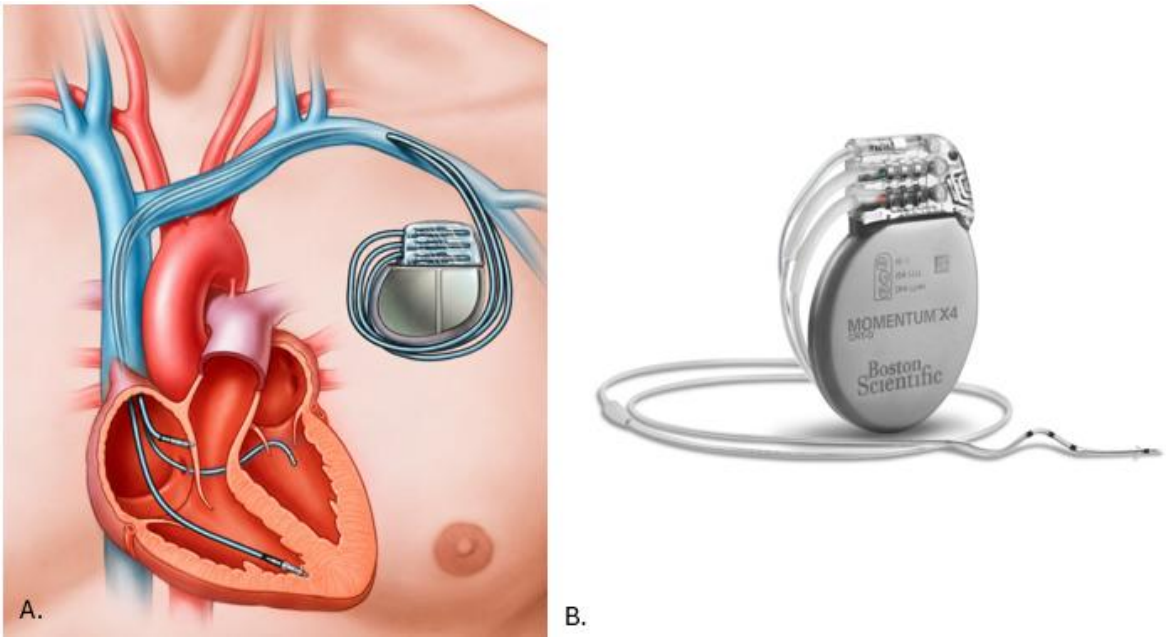


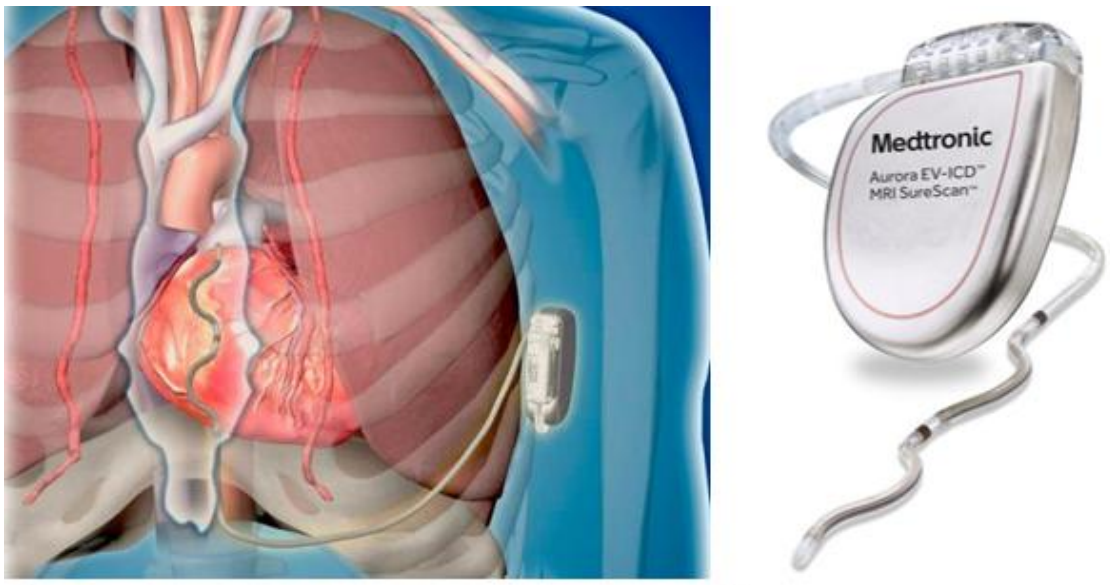
Figure 1. Representative configuration of a conventional transvenous cardiac implantable electronic device system. (A) Schematic illustrating transvenous leads positioned in the right atrium and right ventricle, with a left ventricular pacing lead advanced through the coronary sinus. (B) Represents a transvenous systems complete with pulse generator, and associated leads providing direct intracardiac sensing and therapy delivery.

Subcutaneous implantable cardioverter-defibrillators (S-ICD), **Figure 2**, and extravascular implantable cardioverter-defibrillators (EV-ICD) ,**Figure 3**, systems have been developed to address these clinical requirements and represent major advancements by offering life-saving defibrillation capabilities while minimising lead-related complications.[18,27,28]



A. B.

Figure 2. Representative configuration of a subcutaneous implantable cardioverter-defibrillator (S-ICD) system. (A) Schematic illustrating the entirely extravascular configuration, with the defibrillation electrode positioned along the parasternal region and the pulse generator implanted in the lateral thoracic position. (B) Representative Boston Scientific EMBLEM™ MRI S-ICD pulse generator and subcutaneous electrode.



A. B.

Figure 3. Representative configuration of an extravascular implantable cardioverter-defibrillator (EV-ICD) system. (A) Schematic illustrating the extravascular configuration, with the defibrillation electrode positioned in the substernal space and the pulse generator implanted in the lateral thoracic region. (B) Representative Medtronic Aurora EV-ICD™ pulse generator and substernal electrode.

The transition from intravascular to extravascular stimulation introduces new electrophysiological challenges. Factors such as increased electrode-myocardium distance, tissue impedance variability, and shifts in current density distribution affect excitation thresholds and defibrillation success.[12,29] Despite the growing clinical adoption of these systems, a systematic understanding of waveform-dependent excitability in subcutaneous or extravascular arrangements remains limited.

Beyond clinical electrophysiology, electrical stimulation has also become a significant tool in cardiac bioengineering and regenerative medicine. Human-induced pluripotent stem cell-derived cardiomyocytes (hiPSC-CMs) provide an increasingly valuable platform for modelling cardiac disease, drug testing, and the development of regenerative therapies. hiPSC-CMs generally exhibit immature structural, electrophysiological, and metabolic phenotypes when cultured in vitro, resembling foetal rather than adult cardiomyocytes.[30] Multiple strategies have been explored to promote maturation, including mechanical loading, modulation of substrate stiffness, metabolic conditioning, and three-dimensional tissue engineering. Among these approaches, electrical stimulation has emerged as an effective biophysical cue for promoting cardiomyocyte maturation.[31,32]

Experimental studies have shown that controlled electrical conditioning can improve sarcomeric alignment, enhance calcium handling, increase conduction velocity, and promote more adult-like electrophysiological behaviour in engineered cardiac tissue. For example, progressive electrical stimulation in engineered Biowire constructs significantly improved structural organisation and functional maturation of hiPSC-CMs.[32] Similar electromechanical conditioning of engineered cardiac tissues has been shown to promote contractile maturation, improve excitation-contraction coupling, and enhance electrophysiological integration.[33] These findings suggest that electrical stimulation can act not only as a therapeutic intervention in clinical cardiology but also as a powerful developmental cue in cardiac tissue engineering.

Despite its widespread use in both clinical and research settings, electrical stimulation is often treated as a binary input, with many studies simply comparing stimulated versus non-stimulated conditions or altering a single parameter such as pacing frequency.[34] In reality, electrical therapy involves a complex, multidimensional parameter space that includes waveform characteristics such as amplitude, pulse width, frequency, and waveform type.[35] However, systematic investigations into how these waveform parameters influence cardiac excitability and cellular maturation across different biological scales remain limited. Achieving a thorough understanding of how electrical waveform configurations impact cardiac function at both organ and cellular levels is therefore essential. Such insights are

crucial for optimising next-generation bioelectronic therapies and advancing translational strategies in regenerative cardiology.

1.3. Knowledge Gap in Electrical Waveform Optimisation

While Electrical stimulation is central to clinical cardiac rhythm management and becoming increasingly important in cardiac bioengineering, optimisation of stimulation waveforms remains largely empirical and context-specific. There currently exists no single unified framework that links waveform characteristics to biological or therapeutic outcomes.[7,36] Classical electrophysiological models provide an important foundation for understanding electrical excitation. In particular, the strength-duration relationship described by Weiss and Lapicque establishes that excitation threshold depends on the interaction between stimulus amplitude and pulse duration.[23–25] However, these models were derived primarily from direct myocardial or neural stimulation under controlled electrode-tissue interface conditions.[23–25] Their applicability to contemporary extravascular cardiac systems and to engineered cardiac tissues has not been comprehensively validated.

In clinical electrophysiology, waveform optimisation has traditionally aimed to achieve reliable cardiac capture or effective defibrillation while reducing energy consumption.[7,37] Transvenous pacing systems use two main types of leads, passive and active. Passive leads feature tines that enable the distal end of the lead to contact the endocardium, providing stable contact. Active leads have a screw-in mechanism for direct fixation into the myocardium. The design and implantation workflow for these leads has been optimised to achieve stable tissue impedance and well-established source-sink relationships. In contrast, subcutaneous and extravascular stimulation systems consist of an electrode implanted outside the vasculature, typically positioned parallel to the sternum in the parasternal region. These factors lead to altered current-density distributions and variations in dynamic impedance, which directly influence the biophysical determinants of cardiac excitation.[12,18,29]

Despite the widespread clinical use of S-ICDs and the emerging development of extravascular ICD technologies with pacing capabilities, systematic studies examining parameters such as rheobase, chronaxie, and waveform-dependent capture dynamics remain limited in these settings. Existing reports have predominantly focused on clinical efficacy, safety, defibrillation success, complications and inappropriate shock rates, with comparatively few studies addressing electrophysiological thresholds or the energy-efficiency trade-offs inherent to these systems.[37–40]

At the cellular level, electrical stimulation is extensively employed to promote the maturation of human induced pluripotent stem cell-derived cardiomyocytes (hiPSC-CMs). However, despite widespread use, most maturation protocols focus on or alter a single parameter, most often pacing frequency. An analysis of representative cardiac tissue-engineering studies shows a consistent pattern in stimulation design: electrical stimulation is commonly delivered in the form of monophasic or biphasic square pulse in the low V cm^{-1} range with pulse widths typically fixed between 1 – 2 ms and stimulation frequencies spanning 1 – 6 Hz.[32,35,41–43] Across the studies, electrical stimulation has been shown to enhance structural and functional maturation, including sarcomeric organisation, calcium-handling behaviour, electrophysiological performance, and contractile force.[32,41–44] However, waveform configuration is less commonly examined as an independent experimental variable; in many protocols, pulse width is fixed, and field strength is selected primarily to achieve reliable capture rather than being systematically optimised alongside frequency and waveform geometry.[32,35,42–45] Interestingly, a pulse width of approximately 0.4 ms is commonly used as a clinical reference point for chronic pacing threshold assessment.[37]

As a result, the multidimensional parameter space governing excitation, including amplitude, pulse duration, frequency, duty cycle, and waveform type, remains largely unexplored. More critically, to date, there have been limited systematic investigations that have assessed the influence of waveform configuration itself, independent of simple pacing rate, on hiPSC-CM maturation-relevant responses.

It remains unclear whether current stimulation protocols are mechanistically optimal, energetically efficient, or merely adequate for inducing incremental maturation.[36,45] This represents a significant knowledge gap, particularly since immature cardiomyocytes have altered membrane capacitance, ion channel density, and calcium-handling kinetics, all of which are likely to influence waveform-dependent excitation dynamics.[30,31]

1.4.Research Aim and Objectives

This study investigates the influence of defined electrical waveform configurations on cardiac responses across in vivo and in vitro experimental systems.

Four complementary objectives were established to address this hypothesis:

- **Objective 1: (Chapter 2) Development of a custom waveform-generator platform:**
  Design and implement a custom waveform generator capable of delivering programmable, electrically isolated stimulation pulses to support both in vivo and in vitro experimental studies.
- **Objective 2 - (Chapter 3) Subcutaneous Pacing Threshold Characterisation**:
  Characterisation of myocardial capture thresholds in an extravascular stimulation environment using a porcine S-ICD model to derive electrophysiological parameters, including rheobase and chronaxie values.
- **Objective 3 - (Chapter 4) Ventricular Fibrillation Induction Analysis:**
  Examination of electrical waveform parameters on the success of ventricular fibrillation induction, including peak and average current, as well as stimulation reproducibility in in vivo animal models.
- **Objective 4 – (Chapter 5) Waveform-associated transcriptional responses in hiPSC-CMs:**
  Evaluate the impact of electrical waveform configuration on maturation-associated transcriptional responses in hiPSC-derived cardiomyocytes. This will be assessed using a Design of Experiments framework and targeted quantitative gene-expression analysis across the structural, electrophysiological, intercellular coupling, and calcium-handling domains.

Collectively, these objectives examine electrical stimulation as a set of controllable waveform parameters, rather than a single binary intervention. By combining waveform engineering, preclinical electrophysiology and hiPSC-CM maturation studies, this study aims to generate insight into the optimisation of electrical stimulation for cardiac therapy and regenerative bioengineering. **Figure 4** summarises the thesis's overall experimental framework.

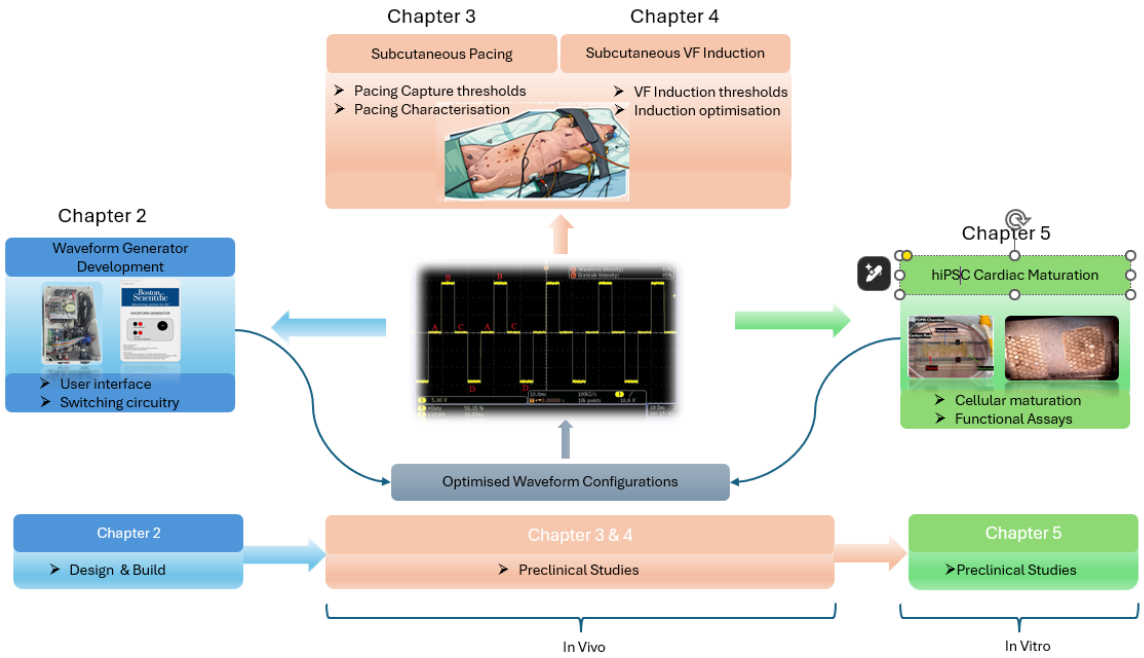


Figure 4. Integrated experimental framework illustrating the development of a programmable waveform generator and its applications in in vivo subcutaneous pacing and ventricular fibrillation induction studies, with subsequent translation to in vitro hiPSC-CMs conditioning. The framework highlights how stimulation parameters were examined across organ-level electrophysiological outcomes and cellular-level maturation- relevant transcript responses.

1.5.Hypotheses

This thesis investigates the influence of electrical waveform configurations on cardiac excitability, ventricular arrhythmia induction and cardiomyocyte maturation-associated responses. The central hypothesis is that these effects are not determined by the presence or absence of electrical stimulation alone but by the specific waveform parameters used to deliver that stimulation, including amplitude, pulse width, frequency and waveform type. This hypothesis is grounded in classical strength-duration theory and principles of membrane charging dynamics, where changes in stimulus amplitude and duration influence excitation probability, current demand and downstream biological response.

It is therefore hypothesised that coordinated variation in waveform parameters will produce measurable differences in myocardial capture thresholds, arrhythmia induction characteristics, and maturation-associated transcriptional response.

The following hypotheses are presented:

1) Subcutaneous myocardial capture thresholds are influenced by waveform configuration. Specifically, variation in pulse amplitude and pulse duration will alter capture thresholds

and allow strength-duration parameters, including rheobase and chronaxie, to be derived under extracellular stimulation conditions.

2) Ventricular fibrillation induction is influenced by waveform configuration. In particular, pulse width, frequency and amplitude will affect both peak current requirements and average current burden during VF induction.
3) Electrical stimulation waveform parameters influence maturation-associated transcriptional responses in hiPSC-CMs. Prolonged stimulation using defined waveform configurations will be associated with changes in transcriptional markers related to sarcomeric remodelling, electrophysiological phenotype, intercellular coupling and calcium handling.

1.6.Novel Contributions

This thesis introduces a unified experimental framework to investigate the impact of electrical waveform configurations across both, in vivo and in vitro cardiac systems. It develops a custom programmable stimulation platform that enables controlled variation of parameters, including amplitude, pulse width, frequency, and waveform morphology. To our knowledge, this continuity of waveform control across in vivo and in vitro cardiac models has not previously been applied in a single experimental framework spanning subcutaneous cardiac stimulation and hiPSC-CM conditioning.

Within this framework, the study provides, to the best of our knowledge, the first systematic derivation of strength-duration relationships, including rheobase and chronaxie, under subcutaneous stimulation in a large-animal preclinical model. By measuring excitation thresholds in an extravascular setup, it expands classical electrophysiological theory beyond transvenous systems. This provides a parameterised foundation for improving pacing strategies for future S-ICD devices.

This thesis develops a quantitative analysis of waveform-dependent VF induction using a structured DOE framework. It examines the balance between peak current demand and average current burden, which influences the probability of successful VF induction.

At the cellular level, this study shows that waveform configuration is associated with maturation-relevant transcriptional responses in hiPSC-CMs. Variation was observed in markers related to sarcomeric remodelling, electrophysiological phenotype, intercellular coupling and calcium handling, including MYH7, MYL2/MYL7, GJA1, GJA5, HCN4, and SHOX2. These findings suggest that electrical waveform parameters may influence maturation-relevant transcriptional organisation, rather than functioning solely as pacing cues.

Collectively, these contributions advance a cross-scale, experimentally grounded framework for waveform optimisation applicable to both bioelectronic device development and electrically guided cardiac tissue engineering.

1.7. Thesis Structure and Chapter Interlinking

This thesis is organised as a progressive, cross-scale investigation of waveform-dependent cardiac modulation. The work begins with the engineering development of a programmable stimulation platform, then applies this system to organ-level electrophysiological studies and finally extends the same waveform-based rationale to cellular transcriptional responses in hiPSC-derived cardiac tissue.

Chapter 1 establishes the clinical and scientific rationale for waveform optimisation. It introduces the need to understand electrical stimulation not simply as a binary intervention, but as a set of controllable parameters that may influence cardiac excitability, arrhythmia induction and maturation-associated cellular responses. The chapter also defines the knowledge gap at the intersection of extravascular electrophysiology, device engineering and electrically mediated hiPSC-CM maturation.

Chapter 2 describes the design, development and validation of the custom programmable waveform generator used throughout the experimental work. The chapter details the system architecture, operating modes and validation approach used to control stimulation amplitude, pulse width, frequency and waveform morphology. This establishes the technical foundation required to deliver comparable waveform configurations across the subsequent in vivo and in vitro studies.

Chapter 3 applies the stimulation platform in a porcine model of subcutaneous cardiac pacing. Using an extravascular stimulation configuration, the chapter characterises myocardial capture thresholds and derives strength-duration relationships, including rheobase and chronaxie values. These measurements provide a framework for understanding how classical excitability principles translate to non-transvenous stimulation pathways.

Chapter 4 builds directly upon the previous chapters, investigating waveform-dependent VF induction thresholds using the same stimulation architecture. This chapter evaluates how pulse width, frequency and current amplitude influence VF induction, with particular attention to the distinction between peak current demand and average current burden. In doing so, it extends the thesis from myocardial capture physiology to arrhythmia initiation and explores the energetic trade-offs relevant to extravascular device design.

Finally, Chapter 6 integrates the findings across all experimental domains. It considers how waveform configuration influences myocardial capture, VF induction, and hiPSC-CM

transcriptional responses, while also addressing the limitations of each model system. The chapter concludes by discussing how a parameter-based understanding of electrical stimulation may inform future work in implantable bioelectronic device development and electrically guided cardiac tissue engineering.

Chapter 2 : Development of a Custom Waveform Generator for Subcutaneous Cardiac Pacing and hiPSC Cardiac Tissue Stimulation

2.1. Introduction and Background

Modern cardiac research relies on precise and reproducible control of electrical stimulation parameters across a broad spectrum of applications, spanning high-energy defibrillation in preclinical and clinical settings to low-amplitude pacing used in cardiac tissue engineering.[46] In clinical practice, implantable cardiac devices, including pacemakers and implantable cardioverter-defibrillators (ICDs), are used to continuously monitor intrinsic cardiac electrical activity and deliver targeted therapies, such as bradycardia pacing, anti-tachycardia pacing, and high-energy defibrillation shocks, as required to restore rhythm.[47,48] Within this domain, subcutaneous implantable cardioverter defibrillators (S-ICDs) represent an extravascular approach to defibrillation, where controlled delivery of electrical waveforms is essential for both therapeutic efficacy and procedures such as defibrillation threshold (DFT) testing.

In parallel, electrical stimulation has emerged as an important approach in cardiac tissue engineering, particularly for the maturation of human induced pluripotent stem cell-derived cardiomyocytes (hiPSC-CMs), which are otherwise characterised by immature structural, electrophysiological and metabolic phenotypes. [32,49] Experimental studies have demonstrated that the application of electrical stimuli enhances cardiomyocyte maturation by promoting sarcomere organisation, increasing conduction velocity and promoting more physiologically relevant calcium handling and electrophysiological behaviour. [32,41,42] Furthermore, biomimetic electrical stimulation has been shown to enhance cell-to-cell coupling, contractile function, and overall tissue organisation, particularly when charge-balanced or biphasic waveforms are employed to minimise electro-mechanical damage and improve stimulation efficiency. [45,50]

In light of these developments, translating controlled electrical stimulation across experimental scales continues to be a formidable task. Preclinical studies on subcutaneous cardiac stimulation and ventricular fibrillation (VF) induction require delivering high-current, precisely timed electrical pulses.[51] These must be administered under conditions that minimise interference with physiological monitoring systems. Additionally, cardiac tissue engineering applications require long-duration, low-amplitude stimulation within controlled

incubators or bioreactors. In such settings, stability and reproducibility over extended periods are essential in attaining consistent cellular maturation.[32,41,46]

To facilitate such studies, bench-top arbitrary waveform generators (AWGs), typically coupled with high-voltage amplifiers, are commonly employed.[52] While these systems offer waveform flexibility, they introduce several limitations in preclinical and translational research settings. In particular, they often lack electrical isolation from mains-referenced systems, are not optimised for portable in vivo use, and can introduce unintended ground-return pathways that compromise the integrity of the testing. [53]

Within these, Chapters 3 and 4 detail the application of subcutaneous stimulation to capture myocardium and to induce VF. To support research objectives 2 and 3, a stimulator capable of delivering high currents while maintaining strict electrical isolation to prevent interference with physiological monitoring systems is required. Chapter 5 investigates the influence of waveform parameters, including pulse amplitude, duration, frequency, and waveform type, on hiPSC-CM maturation over a 14-day stimulation period. Implementing the protocol required a low-voltage stimulator capable of continuous operation in an incubator.

Both the in vivo and in vitro testing protocols share common design requirements. These include programmable control of waveform parameters, such as amplitude, pulse width, frequency, and interphase delay, as well as the ability to generate both monophasic and biphasic waveforms. The temporal structure of these waveforms is defined in **Figure 5**. To address the dual requirements, a Custom Waveform Generator (CWG) was developed. The preclinical, in vivo configuration, delivers short-duration, high-current pulses to enable reliable and repeatable myocardial capture and controlled VF induction within a subcutaneous electrode configuration. The in vitro configuration provides stable, low-voltage pacing to engineered cardiac microtissues, enabling long-term stimulation protocols required for cellular maturation studies.

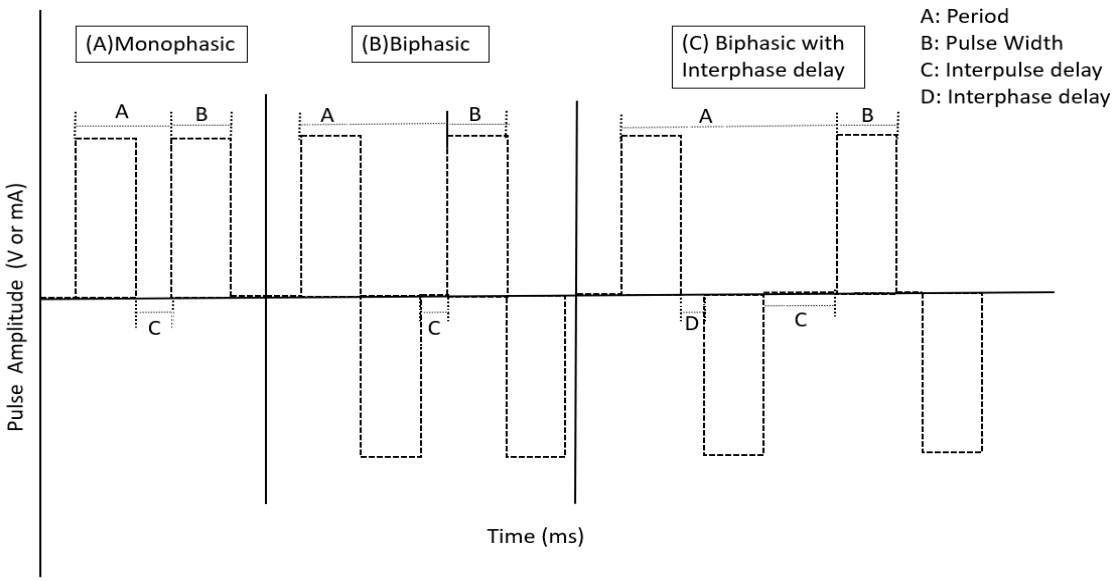


Figure 5. Definition of stimulation waveform architecture and associated timing parameters used throughout this study. Monophasic (A), biphasic (B), and biphasic with interphase delay (C) waveforms are shown. Key temporal parameters are defined as: A, period; B, pulse width; C, inter-pulse delay; D, interphase delay.

Multiple studies have highlighted the benefits of biphasic stimulation due to its ability to minimise net DC charge delivery, reduce electrode polarisation and mitigate tissue damage during repetitive stimulation.[50] Biphasic waveforms have demonstrated greater efficacy and lower defibrillation thresholds than monophasic shocks.[47,54–56] Charge-balanced stimulation reduces electrochemical imbalance at the electrode-electrolyte interface, thereby maintaining culture stability and limiting electrochemical degradation during prolonged operation.[57,58]

2.2. Design Objectives and System Overview

To address the limitations in existing stimulation systems, a CWG was developed to meet the multi-scale experimental requirements of this study. The CWG was designed to provide accurate, programmable electrical stimulation suitable for both high-current in vivo applications and low-voltage in vitro tissue culture. The functional design criteria were captured through a design input and design requirement process, whereby the user needs of the experimental platform were translated into engineering requirements relating to functional, performance, safety and regulatory considerations. The resulting dual-mode design requirements are outlined in **Table 1**.

Table 1. Functional design requirements for the dual-mode CWG derived from design inputs. Requirements are defined to support both high-current subcutaneous stimulation and low-voltage in vitro pacing conditions.

Requirement	In Vivo	In Vitro
Output mode	Constant-current stimulation	Constant-voltage stimulation
Output amplitude	400 mA	20 V
Load impedance range	12.5–250 Ω	100–500 Ω
Pulse width	1–10 ms	1–5 ms
Frequency range	1–5 Hz	
Waveform type	Monophasic/biphasic	
Isolation requirement	Fully galvanically isolated (battery-powered, no mains reference)	Low-noise operation with isolated or floating supply
Control mode	Standalone operation with pre-programmed protocols	PC-controlled (GUI-based) with real-time adjustment
Power architecture	Internal 12 V battery + DC–DC boost + current regulator	External low-voltage supply (e.g. SourceMeter or adapter)
Operational duration	Short-duration, high-power pulses (seconds–minutes)	Continuous operation (days–weeks)
Channel configuration	Single channel (expandable)	

2.3.System Design and Architecture

A common CWG platform was developed to meet the distinct requirements of the in vivo and in vitro experimental models. The system architecture was derived from the functional requirements defined in **Table 1** and was designed to provide accurate control, electrical isolation and reproducible performance across both applications.

The CWG used a modular architecture comprising three core subsystems: a programmable power-delivery stage, a microcontroller-based control unit, and a bidirectional H-bridge output stage. Together, these subsystems enabled programmable delivery of monophasic and biphasic stimulation waveforms, with independent control of amplitude, pulse width,

frequency and interphase as shown in **Figure 6**. The in vivo setup was designed to support high-current stimulation. It incorporates galvanic isolation in the high-current pathway to minimise unintended return currents and ground-loop artefacts during electrophysiological measurements. The in vitro configuration was designed to support consistent, low-noise waveform delivery and compatibility with laboratory equipment for extended cell culture experiments.

The common architecture enabled consistent and repeatable delivery of predetermined waveform configurations. By limiting hardware-related variability, the platform supported systematic characterisation of the influence of stimulation waveforms on biological responses. Its modular structure also provides a practical basis for future development, including the integration of closed-loop control, sensor feedback or multi-channel stimulation, without altering the core waveform generation framework.

The physical implementation of the in vivo and in vitro configurations, together with representative output waveforms, is shown in **Figure 7**.

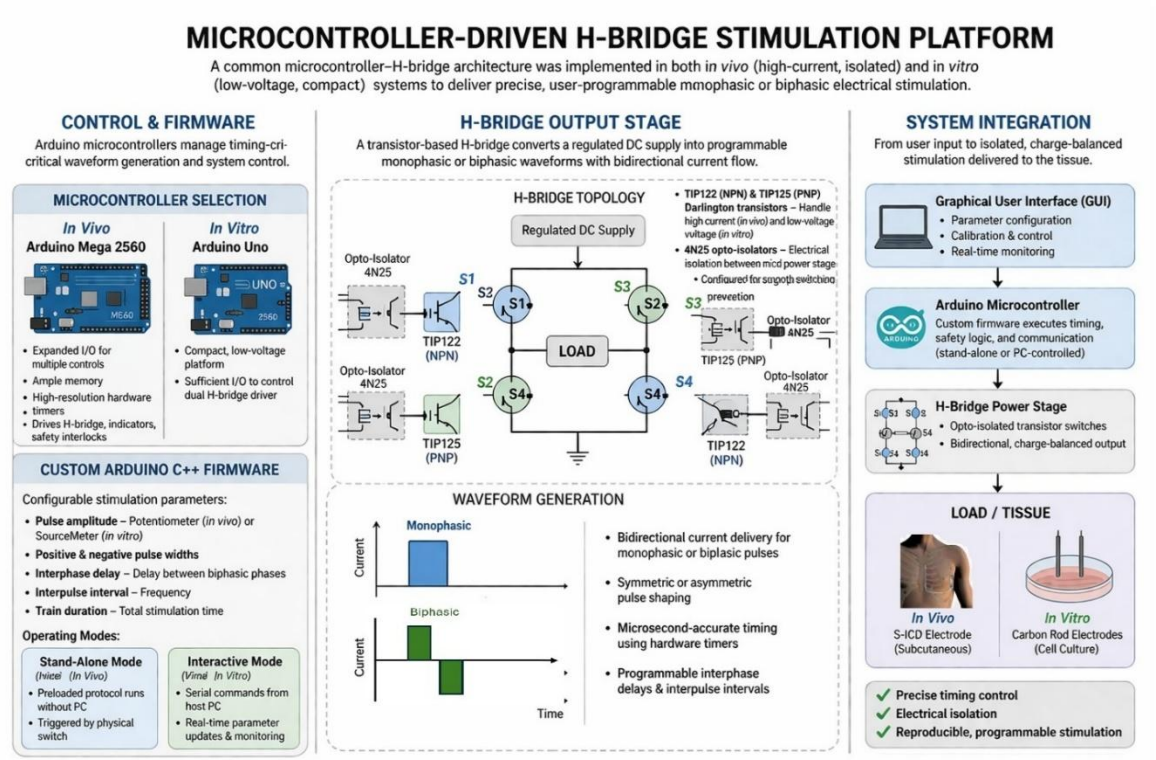


Figure 6. System-level architecture of the Custom Waveform Generator (CWG). The diagram illustrates the microcontroller-driven control framework, galvanically isolated power delivery, and H-bridge output stage enabling programmable monophasic and biphasic stimulation. The modular design supports both high-current subcutaneous stimulation and low-voltage in vitro applications.

In Vivo Configuration **In Vitro Configuration**



Figure 7. Physical implementation and experimental validation of the CWG platform per configuration type. (A) In vivo CWG enclosure designed for high-current subcutaneous stimulation. (B) In vitro CWG enclosure for low-voltage tissue stimulation. (C) Internal architecture of the in vivo system showing boost converter, current regulation, and switching stage. (D) Internal layout of an in vitro system integrating Arduino control and MOSFET H-bridge driver. (E) Representative monophasic waveform output. (F) Representative monophasic and biphasic waveforms.

2.3.1. Power supply architecture

The power supply architecture was developed to support two competing requirements: high current stimulation for acute subcutaneous in vivo studies and low-voltage stimulation for long-term in vitro tissue culture experiments. These requirements are summarised in Table 1.

The subcutaneous in vivo waveform generator provides complete galvanic isolation from the mains-referenced systems by implementing a 12 V, 7 Ah sealed lead-acid battery as the primary energy source. The battery, in turn, powers a 900 W DC-DC boost converter with an adjustable output range of 10 to 120 V, providing the necessary high-voltage rail for pulse delivery.

Subcutaneous stimulation protocols, including post-shock pacing and VF induction, utilise controlled current delivery rather than voltage-driven excitation.[51] A constant-current output stage was implemented, using a TL783 high-voltage linear regulator configured in current-regulation mode, as shown in Figure 4.C. The TL783 supports currents up to 700 mA, exceeding the maximum design requirement of 400 mA. This provides sufficient current capacity while maintaining consistent stimulation output across the expected range of subcutaneous load impedances.

The in vitro configuration prioritises voltage-controlled stimulation to meet tissue culture requirements. This minimises electromechanical effects at the electrode-media interface. The constant-current stage was substituted with an external, programmable Keithley 2400 SourceMeter. This option enables a regulated DC output, featuring integrated current compliance and measurement functions. Such a setup enables accurate control of the stimulation amplitude and protects the engineered cardiac tissues from damage caused by overcurrent. Control Unit and Switching Logic

2.3.2. Control Unit and Switching Logic

The control architecture was designed to satisfy the design requirements by providing precise pulse timing, flexible waveform generation and safe operation across both the in vivo and in vitro configurations. A microcontroller-based switching framework was coupled to a H-bridge output stage, allowing monophasic and biphasic waveforms to be generated with controlled timing and bidirectional current delivery, as shown in Figure 4 E.

A dual-platform microcontroller strategy was used because the two experimental configurations had different operational demands. The in vivo system, shown in Figure 4 A, used an Arduino Mega 2560. This platform was selected for its expanded input and output capacity, increased memory and hardware functionality. These features were required to

coordinate multiple opto-isolated switching elements, implement safety interlocks and execute predefined stimulation protocols with microsecond-level timing accuracy. The in vitro configuration, Figure 4 B, used an Arduino Uno. The Uno provides sufficient I/O capability for the reduced hardware requirements of the tissue culture setup while allowing a smaller physical footprint. The Uno interfaced directly with an integrated MOSFET H-Bridge driver, simplifying the circuit design and reducing switching losses, as shown in Figure 4 D. The in vivo configuration waveform fidelity matched the performance of the in vitro system, Figure 3 F.

A common firmware architecture supports both in vivo and in vitro configurations, ensuring consistent waveform parameters across platforms. The firmware enables full programmability of stimulation parameters, pulse amplitude, pulse width, interphase, and inter-pulse delays, as such satisfying the design and hardware requirements as detailed in Table 1.

Two operational modes were implemented:

1. Standalone mode supports in vivo studies. The system executes predefined stimulation protocols independently of external control systems. This approach facilitates reliability and reduces system complexity in the animal laboratory.
2. Interactive mode developed for in vitro Testing. In this mode, the system allows real-time parameter adjustments via serial communication with a host computer. This mode enabled dynamic protocol changes and continuous monitoring during long tissue experiments.

The H-bridge output stage converted the regulated DC supply into configurable monophasic and biphasic waveforms. In the in vivo configuration, the H-bridge used discrete, TIP122 and TIP125 Darlington transistors connected to the Arduino outputs via opto-isolators. This approach facilitates electrical isolation between the control and power circuits. Preventing switching transients and high-voltage spikes from reaching the microcontroller or external components. In the in vitro setup, a MOSFET-based driver was employed. This approach provides faster switching and lower conduction losses while maintaining adequate control for generating millisecond-scale pulses.

Together, the power, control and switching architecture provide a flexible stimulation platform capable of supporting both acute subcutaneous stimulation protocols and long-term in vitro cardiac tissue experiments. The design allowed reproducible waveform generation

while preserving the different safety, isolation and control requirements of each experimental setting.

2.3.3. Control and Operational Modes

A control interface was developed to support the two operational modes. The in vivo system operated in standalone mode. In this mode, stimulation profiles stored locally on the microcontroller were executed via the hardware-triggered control interface. A hardware interlock prevents unintended output activation. For in vitro operation, the stimulator operated in an interactive mode, allowing real-time parameter updates.

A custom GUI provides operators with access to automated calibration procedures and allows configuration of waveform parameters to meet specific test needs. The Arduino controller communicates via USB with a Python-based GUI application running on a laptop. Through this GUI, as shown in **Figure 8**, the user can adjust waveform parameters in real time, start and stop stimulation, and record parameter settings. A watchdog timer was implemented to monitor for communication errors, to ensure the stimulus would stop in such events, and to ensure the safety of the cells.

The design incorporates additional hardware safety features to minimise the risk of unintended stimulation and to protect both the in vivo animal subjects and the in vitro cell constructs. These include enforced switching of the H-bridge output. The control signals are timed to prevent simultaneous activation of opposing switch pairs, S1/S3 or S2/S4, thereby preventing shoot-through or short circuits. Switching signals are connected through opto-isolators, providing electrical isolation between the control and power domains.

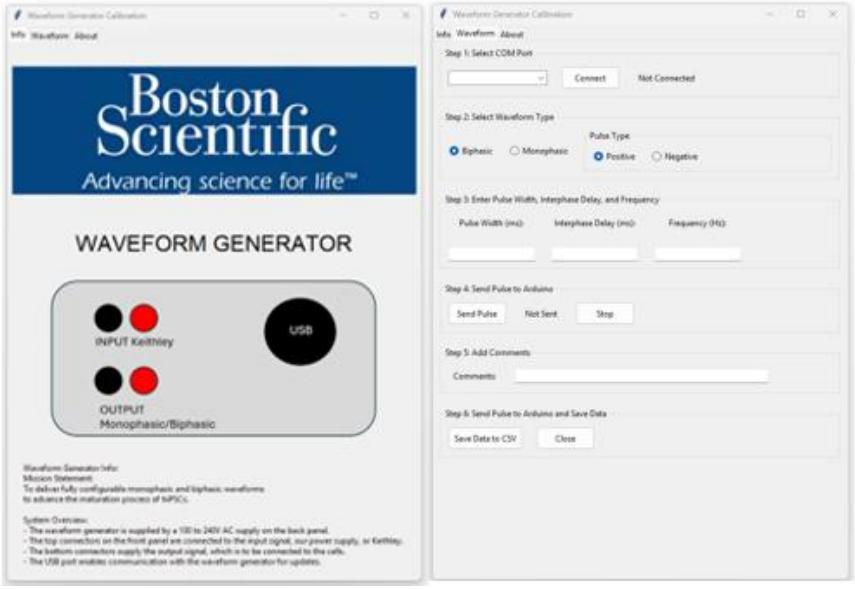


Figure 8. Graphical user interface (GUI) for real-time control, configuration, and monitoring of stimulation protocols. Custom-developed interface allowing user-defined configuration of waveform parameters, including pulse amplitude, width, interphase delay, frequency, and duration. The GUI also supports calibration routines.

2.4. Validation and Testing

Validation testing was conducted to confirm, through examination and the provision of objective evidence, that the requirements for the CWG's specific intended uses could be consistently fulfilled. The CWG validation and characterisation followed a scheduled experimental protocol. All data was recorded in the Engineering Laboratory Notebook (ELN) test report, 1.7. All tests were performed using calibrated laboratory instruments in accordance with ISO/IEC 17025:2017.

Testing was conducted across the full intended operating range, as detailed in **Table 1**. The assessment focused on two principal performance domains: pulse timing and waveform accuracy, and pulse amplitude regulation. Resistive loads ranging from 12.5 Ω to 250 Ω were used to represent the typical impedance spectrum in subcutaneous and tissue-level stimulation.

The objective evidence report and raw measurement workbook supporting CWG characterisation testing are available in the digital repository listed in the front matter Section X Data Availability and Supporting Evidence.

2.4.1. Pulse Timing and Waveform Parameters

Pulse width accuracy was evaluated by comparing programmed pulse parameters with measured outputs across all relevant load conditions. This process included verification of the key measurable waveform parameters, as detailed in **Figure 5**. The CWG demonstrated consistent high accuracy with recorded pulse-width errors of less than 0.67% over the 1-5 ms range for loads from 12.5 Ω to 250 Ω. Biphasic symmetry was assessed through duty-cycle analysis, confirming that for symmetric pulse settings, the duty cycle remained within ± 0.7% of the expected 50%, indicating precise charge-balanced waveforms.[59] These findings show that waveform generation is highly reproducible and largely unaffected by load within the tested range, ensuring reliable operation during both in vivo and in vitro stimulation.

2.4.2. Current Regulation

Current regulation was evaluated by measuring programmed setpoints ranging from 10 mA to 400 mA in 10 mA increments. Testing was conducted with resistive loads from 12.5 Ω to 250 Ω. Results indicated that the CWG consistently delivered stable and predictable amplitude outputs across all test conditions.[59] **Table 2**, below, summarises current regulation performance across defined operating ranges.

Table 2. Summary of current regulation performance across operating ranges. Maximum positive and negative deviations and standard deviation of output current are reported for programmed step changes of 10-400 mA across representative loads of 12.5-250 Ω.

Operating range (mA)	Max Positive deviation (%)	Max Negative deviation (%)	Mean SD (mA) across all tested load conditions
10 – 120	+0.94	-0.94	0.56
120 – 250	+0.94	-2.27	1.65
250 – 400	+0.92	-2.45	3.25

Within the 10-120 mA range, maximum deviations were consistently below ± 1%, achieving peak stability between 12.5 Ω and 75 Ω. However, as the load impedance increased from 200 Ω to 250 Ω, there was a marked rise in deviations, with values reaching 1.65% at 250 mA, 250 Ω and 3.25% at 400 mA, 250 Ω. Throughout the testing process, no instances of instability, oscillations, or nonlinear behaviour were observed.

The CWG demonstrated consistent, reliable performance. The validation data support the intended end use as a current-controlled stimulation platform for preclinical in vivo applications.

2.4.3. Operational Stability

Under high-power, stress conditions (350 mA, 12.5 Ω load), the CWG consistently delivered stable current throughout the specified test period. Thermal monitoring confirmed all components remained within safe operating temperatures, with no activation of thermal protection. These findings confirm that the thermal and electrical design margins are sufficient even under near worst-case loads.

Electromagnetic compatibility (EMC) was tested under typical laboratory conditions. When operating alongside clinical monitoring and measurement devices, the CWG did not result in any noticeable interference or signal artefacts. While formal compliance testing per IEC 61326-1 was not conducted, these results indicate that the device meets acceptable electromagnetic standards for preclinical and intraoperative use.

2.5. Discussion and Future Work

The development of the Custom Waveform Generator demonstrates the advantages of integrating multifunctional capabilities into a single device for experimental cardiac research. A common platform capable of supporting both in vivo and in vitro testing was successfully designed, fabricated, and formally tested. Although the dual functionality necessitated certain engineering trade-offs, none compromised the device's fundamental performance. In fact, the integrated design ultimately enhanced its performance. The high-voltage isolation optimised for in vivo application also resulted in low noise levels for in vitro stimulation, and the precise control required for in vitro experiments improved the fidelity of in vivo pulse delivery.

2.6.Limitations

Despite its successes, the CWG, in its current form, remains a laboratory prototype. It's currently a single-channel device. Reducing the quantity of testing that can be conducted simultaneously. Another limitation is reliance on a PC for the most user-friendly in vitro operation. While the device can run stand-alone, the GUI facilitates prolonged runs and data logging. This was an advantage in the lab, enabling the stimulator to operate in a standalone bioreactor; a small built-in user interface may be required for enhanced convenience.

2.7. Future improvements:

There are several avenues to enhance the CWG in the future:

2.7.1. Multi-channel output

Incorporating independent H-bridge channels enables the concurrent stimulation of multiple tissue samples or various sites within an organ. By utilising the existing integrated driver, a two-channel configuration can be achieved by using the second bridge on the AEK-MOT module, along with an additional set of output terminals. The microcontroller firmware would require modifications to synchronise or stagger the stimulation pulses.

2.7.2. Closed-loop control

Incorporating sensing, such as ECG input or a tissue contraction sensor, could enable trigger-based or adaptive stimulation. For instance, in vivo, the device could detect an R-wave and deliver a pulse only after a certain delay, similar to shock on T pacing, utilised in transvenous VF induction studies. This could also be used to detect if VF was achieved and stop further pulses. In vitro, the stimulator can adjust pacing rates as tissues mature. As discussed in Chapter 5, an impedance measurement of the cellular construct can identify key maturation milestones. Given the complexity of closed-loop algorithms, this was beyond the initial scope, but should the system progress towards commercialisation, these aspects would certainly warrant resourcing and funding.

2.7.3. Enhanced GUI and data logging

Opportunities exist to enhance the graphical user interface to include automatic logging of stimulation parameters and responses. These include automatic recording of SourceMeter data, thereby yielding a more comprehensive dataset for experimental analysis. Currently, this information is recorded manually. Automating the process would minimise the risk of data entry errors. Additionally, incorporating the Keithley device's LAN interface into the GUI would facilitate seamless adjustment of voltage settings and current measurements without manual intervention.

2.8. Conclusion

The Custom Waveform Generator proved to be a highly effective and innovative solution for our dual needs. By emphasising a clear separation of concerns, isolated high-voltage vs precision low-voltage, while reusing the core waveform generation, the system achieved a design that is both versatile and reliable. The work presented here on the CWG will support the subsequent chapters' findings and stands on its own as a contribution to research instrumentation in bioengineering.

With further refinements and certification, this system could be adopted or adapted by other researchers who require custom electrical stimulation for cardiac, neural, or muscular applications. The Custom Waveform Generator successfully achieved its objectives and has been validated to operate under the demanding conditions of both in vivo defibrillator-testing and in vitro tissue-conditioning experiments. It provides precise control over stimulation parameters, allowing experimental variables to be finely tuned and kept consistent.

Chapter 3 Subcutaneous Pacing

3.1. Introduction

Electrical stimulation of excitable biological tissue is a fundamental principle in modern medicine. It supports therapeutic modulation of both cardiac and neural systems.[60] Applications span cardiac rhythm management, neuromodulation, and sensory prosthesis, in which controlled delivery of electrical energy is used to depolarise excitable membranes and restore or augment physiological function.[58]

Within cardiology, implantable cardioverter-defibrillators (ICDs) have transformed the prevention of sudden cardiac death (SCD). They have demonstrated substantial reductions in mortality among patients at risk of life-threatening ventricular arrhythmias.[40] Conventional transvenous ICDs provide reliable sensing, pacing, and high-voltage shock therapy through leads implanted within the cardiac chambers.[12] While this architecture provides effective therapy delivery, the intravascular leads remain a major contributor of device-related complications and long-term system failure.[61] Clinical registry data consistently demonstrate that complications following cardiac implantable electronic device (CIED) implantation are non-trivial. Reported complications span mechanical, vascular and systemic events, including cardiac perforation, pneumothorax, thromboembolic events, and infection.[29] In a nationwide cohort of 5,918 patients, Kirkfeldt et al. reported that 9.5% experienced at least one complication within six months of implantation.[62] Similarly, the contemporary registry analysis completed by Van Barreveld et al. using the nationwide DO-IT registry (n=1442; median follow-up 28.7 months) reported complication rates of 13.5% with a substantial proportion requiring reintervention or prolonged hospitalisation.[61] Koneru et al conducted a retrospective longitudinal analysis of data from the OptumLabsTM Data Warehouse. This analysis demonstrated that the incidence of lead complications accumulates over time, affecting approximately one in four patients at 10 years of follow-up. [63]

To resolve these limitations, ICD designs that eliminate transvenous leads have been developed. The fully subcutaneous ICD (S-ICD), developed by Boston Scientific, provides effective defibrillation therapy without the need for endovascular hardware.[12,29] The S-ICD is intended for patients who have an indication for primary or secondary prevention of sudden cardiac death (SCD) and do not require pacing.[64] A subcutaneously implanted electrode facilitates both sensing and the delivery of therapeutic shocks as indicated.[12] By implanting the entire system, including the pulse generator and electrode, in the subcutaneous tissues and along the chest wall, the S-ICD avoids complications specifically associated with transvenous or endocardial leads.[12,18] Medtronic developed the extravascular

ICD (EV-ICD), which positions a lead in the substernal space, anterior to the heart, beneath the sternum. This setup maintains the benefit of avoiding transvenous leads while enabling pacing therapies, particularly anti-tachycardia pacing (ATP) to prevent re-entrant ventricular tachycardias, and limited bradycardia support.[28] Therefore, EV-ICD systems aim to combine the main advantage of the S-ICD, no transvenous lead, with some of the diagnostic and therapeutic features previously exclusive to transvenous devices, such as rhythm pacing and ATP.[28,65]

Clinical experience with alternative ICD architectures has been encouraging. Real-world data confirms the safety and efficacy of S-ICDs in routine practice. In the multicentre EFFORTLESS S-ICD registry, Lambiase et al. reported complication-free survival of 97% at 30 days and 94% at 12 months (n=470), indicating that only 6.4% of patients experienced device-related complications at 12 months.[40] Knops et al. in the randomised PRAETORIAN trial (849 patients followed for 4 years) demonstrated that S-ICD therapy is non-inferior to transvenous ICDs and significantly reduces lead-related adverse events.[66] Data from the PRAETORIAN trial demonstrated a higher incidence of device-related complications in transvenous ICDs compared with S-ICDs (9.8% vs 5.9%), with a markedly higher burden of lead-related complications in transvenous systems.[64] These findings support S-ICD as an effective alternative that avoids the primary failure point of conventional ICD therapy, the transvenous lead. Initial feasibility of substernal extravascular defibrillation was demonstrated in early human studies, which established the technical viability and safety of this novel approach.[67] Subsequently, the EV-ICD pivotal trial confirmed high defibrillation efficacy and favourable safety outcomes, with 92.6% of patients remaining free from major complications at 6-10 months.[28] Further analyses of this cohort have demonstrated favourable patient-reported outcomes.[68]

Collectively, these findings underscore the potential of extravascular ICD systems to provide effective arrhythmia protection while mitigating the lead-related complications associated with transvenous ICD systems.[28,64,65] They have demonstrated success as a potential means to address the primary failure modes associated with intravascular leads while ensuring patient safety. The transition from intravascular to extravascular stimulation introduces fundamentally different electrophysiological conditions. Increased electrode-myocardium separation, heterogeneous tissue conductivity, and altered current density distributions significantly influence excitation thresholds and stimulation efficiencies.[29,40] The electrophysiological mechanisms governing myocardial excitation under extravascular stimulation remain incompletely characterised.[69,70] Classical models of excitability, including strength-duration relationships derived from direct electrode-tissue interfaces,

may not fully account for the spatial and biophysical complexities of subcutaneous or substernal stimulation. Consequently, there is a need to systematically evaluate how waveform configuration and stimulation parameters influence myocardial capture in these environments.

Accordingly, this work seeks to address this knowledge gap by investigating the relationship between electrical waveform configurations and myocardial excitability under extravascular stimulation conditions. Through controlled preclinical experimentation, this study aims to establish a quantitative and mechanistic framework linking stimulus parameters to cardiac capture response, thereby informing the design and optimisation of next-generation extravascular cardiac rhythm management systems.

3.1.1. Research Question

The central research question addressed in this study is:

How do electrical waveform parameters influence myocardial capture thresholds and excitability under subcutaneous conditions?

This preclinical study aimed to systematically characterise myocardial excitation under subcutaneous stimulation conditions using a porcine model.

The objectives included:

1. To quantify myocardial capture thresholds across varying waveform parameters.
2. To develop individualised strength-duration curves to determine rheobase and chronaxie.
3. To evaluate the applicability of traditional cardiac excitability models under subcutaneous stimulation conditions characterised by increased electrode-myocardium separation.
4. To compare the efficacy of biphasic and monophasic waveforms in modulating myocardial capture thresholds under subcutaneous stimulation conditions.

This work aims to inform energy-delivery requirements and guide waveform optimisation for emerging subcutaneous and extravascular cardiac rhythm management systems.

3.2. Method

3.2.1. Subcutaneous Pacing Threshold Testing Preparation

All animal procedures were performed in accordance with institutional and national ethical guidelines for the care and use of laboratory animals. The study protocol (Study #17-082N) was reviewed and approved by Boston Scientific's Institutional Animal Care and Use Committee (IACUC).[71]

Subjects (n = 4, swine) were selected as a clinically relevant large-animal model because porcine thoracic and cardiovascular anatomy broadly align with adult human anatomy for studies involving transthoracic or extravascular cardiac stimulation.[72] Each animal was premedicated with intramuscular ketamine (20 mg/kg) and xylazine (2 mg/kg), followed by endotracheal intubation and mechanical ventilation. General anaesthesia was maintained with isoflurane (1.5 - 2.0%) to maintain hemodynamic stability.[73]

To minimise skeletal muscle contractions during pacing and to prevent lead dislodgement or motion artefacts, vecuronium was administered as a neuromuscular blocker. An initial intravenous dose of (0.1–0.15 mg/kg) was followed by a continuous rate of infusion (CRI) of (0.1-0.2 mg/kg/hr). Vecuronium was selected over depolarising agents such as succinylcholine due to its minimal effect on serum potassium levels, eliminating the need for continuous electrolyte monitoring.[73]

Continuous physiologic monitoring included ECG, arterial blood pressure (via a Millar catheter), oxygen saturation (SpO_2), end-tidal CO2 (EtCO2), and core temperature.

Animals were positioned in dorsal recumbency. A right jugular venous cutdown was performed to provide venous access for the placement of an Endotak transvenous ICD lead. The lead was introduced and advanced under fluoroscopy to the right ventricular apex. The lead was then secured to the vessel using a non-absorbable suture. Arterial access was obtained via femoral artery cannulation, and a high-fidelity Millar pressure catheter was inserted into the thoracic aorta to enable real-time hemodynamic monitoring during pacing. **Figure 9**.

A subxiphoid incision was made to allow tunnelling of the subcutaneous electrode along the right parasternal margin. The electrode was secured at both ends using non-absorbable sutures. Additionally, a subcutaneous generator (dummy pulse can) was implanted in the right lateral thoracic region to complete the coil-to-can pacing vector.

All incisions were closed in anatomical layers using standard surgical technique. Animals were allowed to stabilise for a minimum of 15 minutes prior to the initiation of pacing threshold testing.

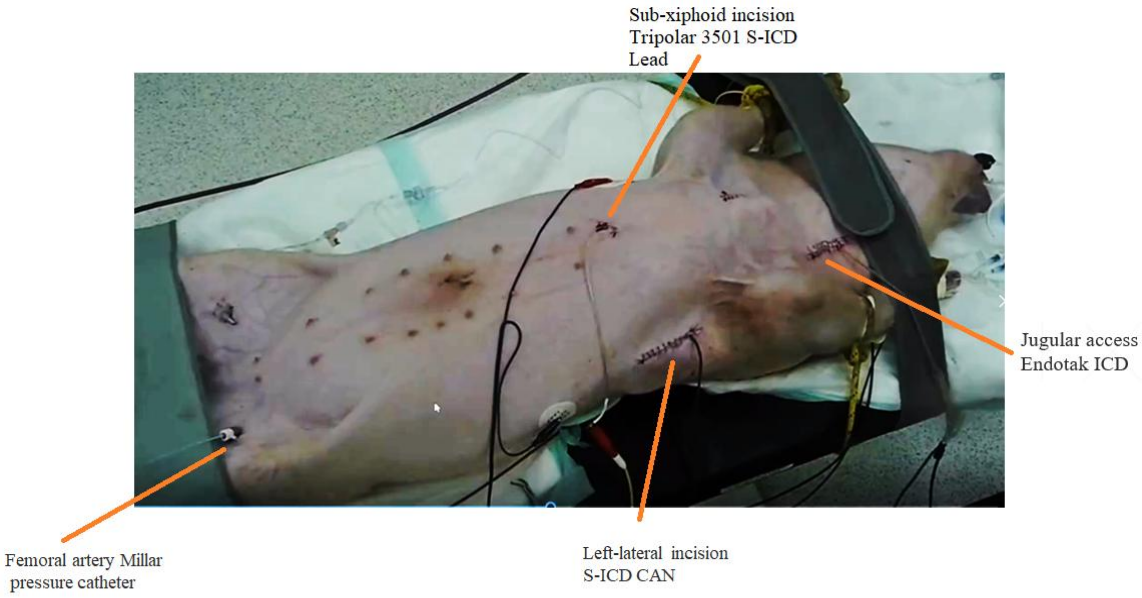


Figure 9. Surgical access and electrode configuration in the porcine model. Representative image illustrating subject positioning in dorsal recumbency with completed transvenous and subcutaneous instruments. The right jugular venous cutdown enabled transvenous placement of a right ventricular ICD lead. An S-ICD electrode was implanted along the right parasternal margin via a subxiphoid tunnelling approach. A non-functional subcutaneous generator was positioned in the right lateral thorax to complete the coil-to-can vector, consistent with clinical device configurations.

3.2.2. Subcutaneous Pacing Threshold Testing Method

Pacing threshold assessments were performed using the implanted subcutaneous electrode configuration. The electrode-can arrangement replicated the therapeutic vector of contemporary S-ICD systems, **Figure 9**.

The overarching aim was to evaluate how varying pulse width and amplitude influence the ability to capture myocardium when stimulation is applied from a non-intravascular position. Each test commenced with the delivery of a pacing train consisting of 10 pulses, paced to exceed the animal's intrinsic heart rate by 20-40 beats per minute. This pacing rate was chosen to ensure that each stimulus occurred independently of spontaneous cardiac activity, thereby avoiding fusion beats or misinterpreted capture.

Pulse delivery was administered asynchronously and under manual control. Testing was initiated at an amplitude below the anticipated capture threshold, with current levels increased incrementally by 10 mA or 10%, contingent upon waveform stability and observed physiological response. All pacing pulses were delivered as square waveforms, with both monophasic and biphasic configurations evaluated. Pulse widths were sequentially tested within a range beginning at one millisecond and increasing in one-millisecond steps up to ten milliseconds. For each pulse width, myocardial capture was assessed by analysing the

pressure waveform obtained from an intra-aortic Millar catheter, rather than relying solely on electrocardiographic data, due to significant artefact interference.

Each pulse width condition was repeated up to four times to confirm consistency and account for physiological variability. Between runs, a short recovery period was observed to allow stabilisation of hemodynamic parameters and to reduce any effects of tissue accommodation. Threshold data were used to generate strength-duration plots, from which rheobase and chronaxie values were estimated using nonlinear curve fitting to the classical strength–duration model. These values served as markers of tissue excitability under each of the tested waveform conditions.

3.3. Results

3.3.1. Subcutaneous Testing Results

The following section presents the results of the subcutaneous pacing threshold testing. The findings are reported in two sections.

The threshold responses of individual subjects are described in detail, including replicated measurements, fitted strength-duration curves and derived rheobase and chronaxie values.

A cross-subject analysis was performed to assess intra-test consistency, waveform-specific behaviour, and any notable deviations from expected electrophysiological patterns.

All animals are referred to by anonymised identifiers (SW6022, SW6045, SW6047, -SW6054), which correspond to individual test subjects enrolled in Study 17-082N. These identifiers carry no relation to treatment order, weight or other classification and serve solely as reference markers for data presentation.

Threshold data were modelled using the Weiss hyperbolic strength-duration formulation, which relates stimulus current to pulse widths as follows:

Equation 1. Weiss hyperbolic strength-duration formulation, I is the threshold current (mA), Irh is the rheobase (the minimum asymptote current required for capture), tc is the chronaxie (the pulse width at which the current equals twice the rheobase), and PW is the pulse width (ms).

$$I = I_{rh}\left(1 + \frac{\tau_c}{PW}\right)$$

Fitted strength-duration curves based on **Equation 1** were generated for each subject, providing both descriptive and model-derived characterisation of subcutaneous pacing

thresholds. Results are presented in tabular and graphical form, with mean values and 95% confidence intervals (CIs) reported where replicate trials were available.

For animals SW6045 and SW6047, both monophasic and biphasic pulse waveforms were tested. To ensure a balanced and statistically robust comparison between waveform types, the waveform analysis was restricted to pulse widths common to both stimulation conditions (1, 2, 4, and 8 ms). Pulse widths of 3, 5, 6, and 10 ms were excluded from the specific comparison, as these conditions were evaluated only with monophasic stimulation and would therefore introduce bias due to unequal representation of waveform types. A general linear model was therefore run using only the matched pulse-width conditions. This approach ensured that any observed differences could be attributed to waveform type rather than to confounding effects of pulse duration or unequal sample sizes.

3.3.1.1. Subject-Specific Threshold Analysis

SW6022

Testing in animal SW6022 consisted of three to four replicate measurements obtained at each tested pulse width from 1-10 ms. The capture thresholds are summarised in **Table 3**, reported as mean ± standard deviation (SD) together with 95% confidence intervals (CI).

Table 3. Subcutaneous pacing thresholds in SW6022 as a function of pulse width. Mean peak current required for capture is shown as mean ± SD with corresponding 95% confidence intervals (CI). Each pulse width was tested with 3-4 replicates per condition.

Animal ID	PW(ms)	Pulse Type	N	Mean (mA)	±SD (mA)	95% CI Lower (mA)	95% CI Upper (mA)
SW6022	1	Monophasic	4	132.00	8.08	119.15	144.85
SW6022	2	Monophasic	3	105.00	6.93	87.77	122.23
SW6022	3	Monophasic	3	94.67	10.97	67.42	121.92
SW6022	4	Monophasic	3	88.00	5.20	75.09	100.91
SW6022	5	Monophasic	4	96.00	5.77	86.82	105.18
SW6022	6	Monophasic	0	NA	NA	NA	NA
SW6022	8	Monophasic	3	82.00	0.00	82.00	82.00
SW6022	10	Monophasic	3	82.00	0.00	82.00	82.00

In line with classical transvenous pacing, threshold currents declined steeply between 1 ms and 4 ms , (132 mA to 88 mA), consistent with the rapid charging requirements of excitable

membranes at short pulse widths. Beyond 4 ms, the threshold approached a plateau, with values converging toward 82 mA, indicating that further increases in pulse width yielded minimal efficiency gains as the rheobase was approached.

A fitted Weiss-Lapicque hyperbolic strength-duration model, **Figure 10**, yielded a rheobase of 77.58 mA and a chronaxie of 0.70 ms. A comparable empirical estimate of the replicate data yielded a closely aligned estimate (rheobase = 82 mA, chronaxie = 0.63 ms), reinforcing the robustness of the fitted model.

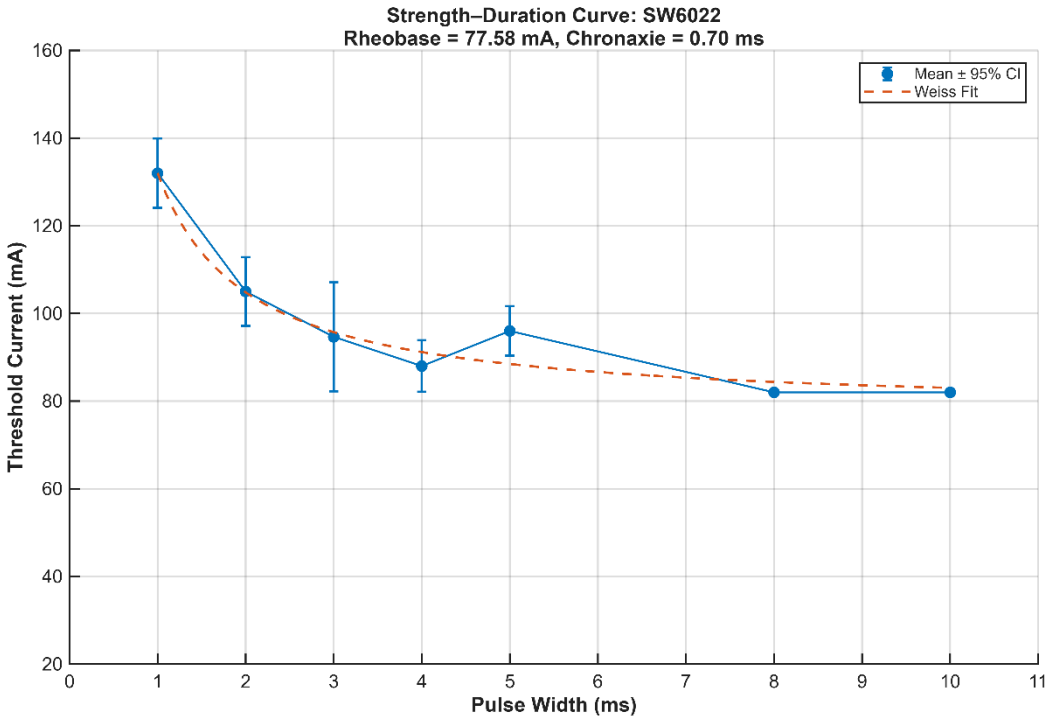


Figure 10. Strength-duration curves for SW6022 show mean threshold current (mA) as a function of pulse width (ms) for monophasic stimulation. Data points represent the mean ± 95% CI at each pulse width. These plots illustrate the relationship between stimulus duration and excitability.

Of the 4 animals tested, SW6022 was the only animal to show a non-monotonic trend, its threshold increased from 88 mA at 4 ms to 96 mA at 5 ms, before returning to the expected trajectory by 6-8 ms, Figure 2.

Device setup was confirmed not to influence the results, as the configuration remained consistent across all tests. Once the electrode and pulse generator were implanted, no further interactions occurred until they were explanted.

While this anomaly was not directly examined, the evidence indicates that myocardial adaptation may play a role. As described by Merrill et al, repeated subthreshold stimulation can result in transient depolarisations that may reflect transient physiological variability or measurement artefact, consequently elevating the excitation threshold.[60] This temporary

decrease in myocardial responsiveness may account for the increased threshold observed at 5 ms.

SW6045

SW6045 was assessed using both monophasic and biphasic stimulation protocols. The monophasic protocol was evaluated in duplicate, whereas the biphasic protocol was assessed once at each pulse duration. Statistical analysis indicated no significant difference in capture thresholds between the monophasic and biphasic configurations for SW6045 ($p = 0.930$). As detailed in Section 3.3.1, to ensure a balanced and statistically robust comparison between waveform types, the waveform analysis was restricted to pulse widths common to both stimulation conditions (1, 2, 4, and 8 ms). A summary of the pooled threshold data for SW6045 is provided in **Table 4**.

Table 4. Subcutaneous pacing thresholds in SW6045 as a function of pulse width. Mean peak capture current is shown as the mean ± SD, with the corresponding 95% confidence interval (CI). Each pulse width was tested with 1-3 replicates per condition

Animal ID	PW (ms)	Pulse Type	N	Mean (mA)	±SD (mA)	95% CI Lower (mA)	95% CI Upper (mA)
SW6045	1	Mono/Biphasic	3	113	0	113	113
SW6045	2	Mono/Biphasic	3	82.33	0.29	81.61	83.05
SW6045	3	Monophasic	1	66.7	NA	NA	NA
SW6045	4	Mono/Biphasic	3	66.33	0.47	65.16	67.50
SW6045	5	Monophasic	1	60	NA	NA	NA
SW6045	6	Monophasic	1	60	NA	NA	NA
SW6045	8	Mono/Biphasic	3	60	0	60.00	60.00
SW6045	10	Monophasic	1	54	NA	NA	NA

A fitted strength-duration curve, **Figure 11**, demonstrated a hyperbolic relationship between pulse width and threshold current. The fitted curve yielded a rheobase of 49.02 mA and chronaxie of 1.30 ms, indicating that SW6045 achieved capture at considerably lower currents in comparison to SW6022.

Contrary to the commonly reported advantages of biphasic stimulation, including reduced stimulation thresholds and minimised charge delivery per phase compared to monophasic configurations,[45,54] the biphasic configuration in this study did not confer a measurable reduction in activation thresholds. Notably, there was no significant difference in impact between the monophasic and biphasic waveforms. This finding may be attributed to the

specific characteristics of the biphasic waveform employed, potentially the set interphase delay.

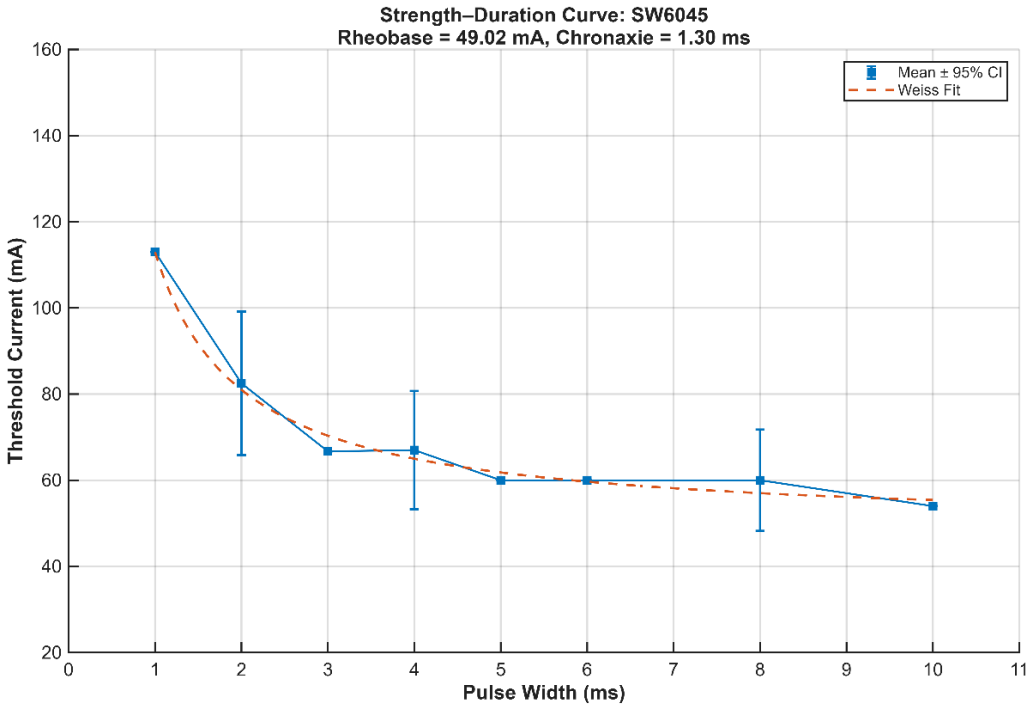


Figure 11. Strength-duration curves for SW6045 showing mean threshold current (mA) as a function of pulse width (ms) for pooled monophasic and biphasic stimulation. Data points represent the mean ± 95% CI at each pulse width. Solid blue line connects the means of each threshold curve. The dashed orange line indicates the fitted Weiss-Lapicque model, from which the rheobase and chronaxie values were derived.

SW6047

SW6047 was evaluated using both monophasic and biphasic waveform configurations. The monophasic waveform was tested in duplicate, while the biphasic waveform was tested once at each pulse width. The measured data for SW6047 are summarised below in **Table 5**.

Table 5. Subcutaneous pacing threshold in SW6047 as a function of pulse width. Mean peak current required for capture is shown as mean ± SD with corresponding 95% confidence intervals (CI).. Each pulse width was tested 1-3 replicates per condition.

Animal ID	PW (ms)	Pulse Type	N	Mean (mA)	±SD (mA)	95% CI Lower (mA)	95% CI Upper (mA)
SW6047	1	Mono/Biphasic	3	76.67	4.62	65.20	88.14
SW6047	2	Mono/Biphasic	3	49.00	0.00	49.00	49.00
SW6047	3	Monophasic	1	39.00	NA	NA	NA
SW6047	4	Mono/Biphasic	3	33.33	2.31	27.59	39.07
SW6047	5	Monophasic	1	32.00	NA	NA	NA
SW6047	6	Monophasic	1	28.00	NA	NA	NA
SW6047	8	Mono/Biphasic	3	26.00	0.00	26.00	26.00
SW6047	10	Monophasic	1	26.00	NA	NA	NA

A fitted strength-duration curve for SW6047 was generated using the Weiss hyperbolic model. The curve, depicted in **Figure 12**, illustrates a hyperbolic relationship between pulse width and threshold current. The model fitting yielded an estimated rheobase of 19.01 mA and a chronaxie of 3.11 ms, suggesting that SW6047 was capable of achieving cardiac capture at lower current levels compared to SW6022 and SW6045.

Regression analysis revealed no statistically significant difference in capture thresholds between monophasic and biphasic stimulation for SW6047 ($p = 1.00$). As with other subjects, all waveforms exhibited elevated threshold currents at shorter pulse widths. This reflects the increased charge required for myocardial activation with brief stimuli. Thresholds decreased with increasing pulse duration, following the expected hyperbolic trend.

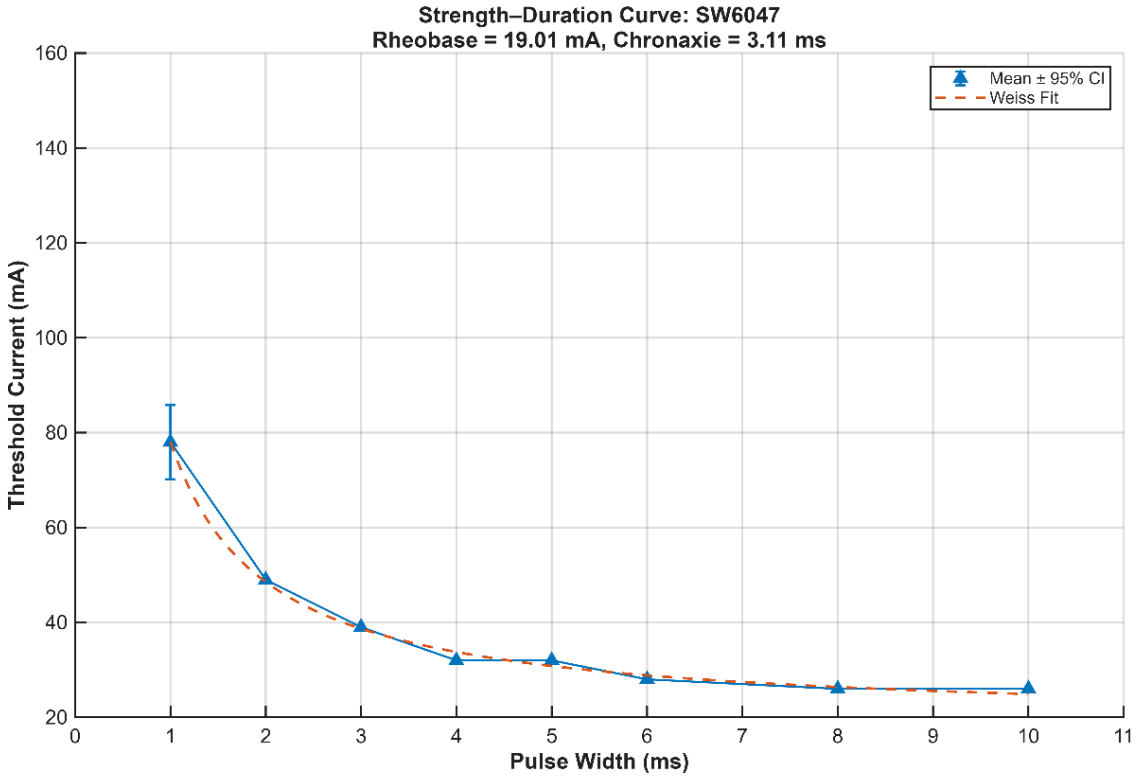


Figure 12. Strength-duration curves for SW6047 showing mean threshold current (mA) as a function of pulse width (ms) for pooled monophasic and biphasic stimulation. Data points represent the mean ± 95% CI at each pulse width. Solid blue line connects the means of each threshold curve. The dashed orange line indicates the fitted Weiss-Lapicque model, from which the rheobase and chronaxie values were derived.

SW6054

SW6054 was evaluated using a single monophasic waveform configuration across pulse widths ranging from 1 to 10 ms. The results are summarised below in **Table 6**.

Table 6. Subcutaneous pacing thresholds in SW6054 as a function of pulse width. Each pulse width was tested once; therefore, variability metrics (SD and 95% CI) could not be calculated

Animal ID	PW (ms)	Pulse Type	N	Mean (mA)	±SD (mA)	95% CI Lower (mA)	95% CI Upper (mA)
SW6054	1	Monophasic	1	155	NA	NA	NA
SW6054	2	Monophasic	1	113	NA	NA	NA
SW6054	3	Monophasic	1	91.5	NA	NA	NA
SW6054	4	Monophasic	1	91.5	NA	NA	NA
SW6054	5	Monophasic	1	82.4	NA	NA	NA
SW6054	6	Monophasic	1	74.1	NA	NA	NA
SW6054	8	Monophasic	1	66.7	NA	NA	NA
SW6054	10	Monophasic	1	66.7	NA	NA	NA

It was not possible to obtain replicate measurements for SW6054. The dataset demonstrated a clear strength-duration relationship, aligned with the results of the other animals. This behaviour is consistent with classical electrophysiological theory and aligned with the hyperboloid threshold profile observed in the remaining subjects. When fitted to the Weiss-Lapicque hyperbolic strength-duration model as shown in **Figure 13**, the data suggested a plateau in threshold current at approximately 67 mA from 8 ms onward, consistent with proximity to rheobase.

The single-run nature of this dataset prevented assessment of intra-subject variability, limiting confidence in the precision of the fitted parameters. Therefore, these findings can only be interpreted as descriptive rather than statistically definitive. SW6054 provides a representative subject-level profile of myocardial excitability under monophasic stimulation and supports the overall strength-duration behaviour observed across the study.

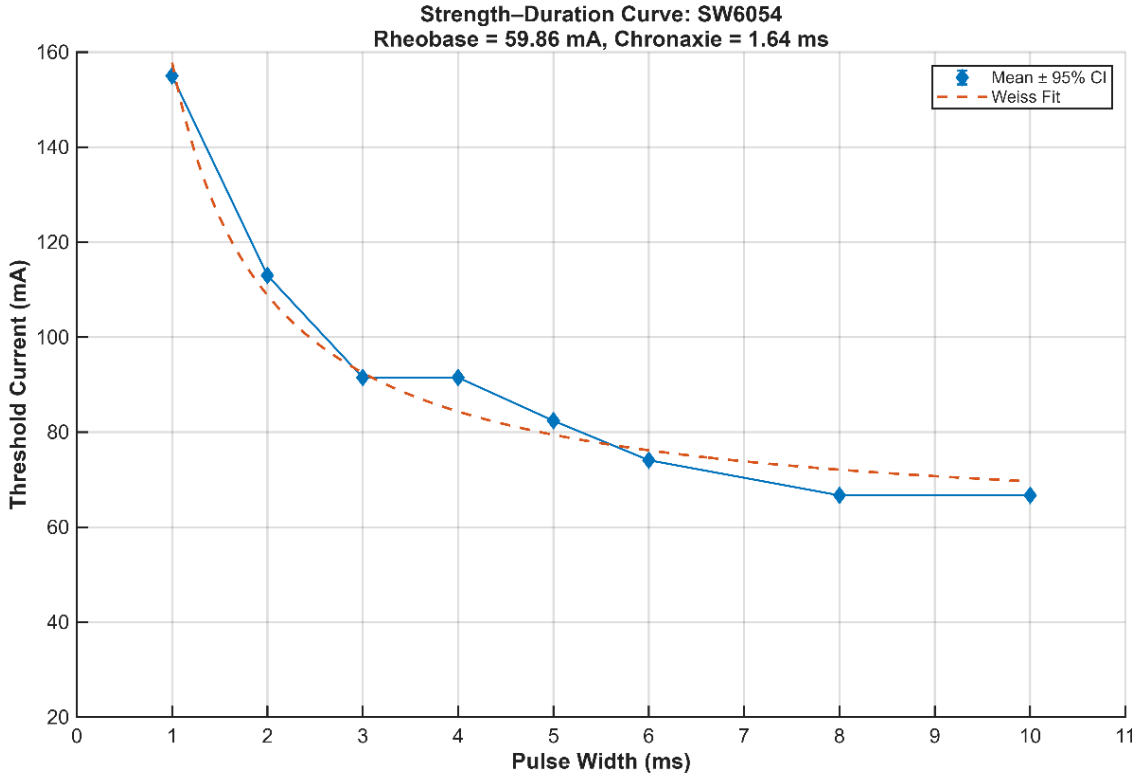


Figure 13. Strength-duration curve for SW6054, monophasic only. Data points represent single measurements at each pulse width. The dashed line is the Weiss-Lapicque fitted strength-duration curve.

3.3.2. Collective Evaluation of Stimulation Thresholds and Pulse Duration Dependencies

Across all four animals, subcutaneous pacing threshold data demonstrated a characteristic inverse relationship between stimulus pulse duration and the peak current required to achieve

myocardial capture, as shown in **Figure 14**. Threshold current decreased steeply with increasing pulse width between 1 and 4 ms and approached an asymptotic plateau at longer durations, consistent with classical strength-duration behaviour.14,15 This relationship was statistically confirmed using a general linear modelling approach, which demonstrated a highly significant main effect of pulse width on pacing threshold ($F = 151.48$, $p < 0.001$). Relative to 1 ms stimulation, threshold reductions of approximately 29 mA, 45 mA and 52 mA were observed at pulse widths of 2 ms, 4 ms and 8 ms, respectively. Although thresholds continued to decrease between 4 ms and 8 ms, the magnitude of reduction diminished, indicating an approach towards the rheobase region rather than a strict plateau.

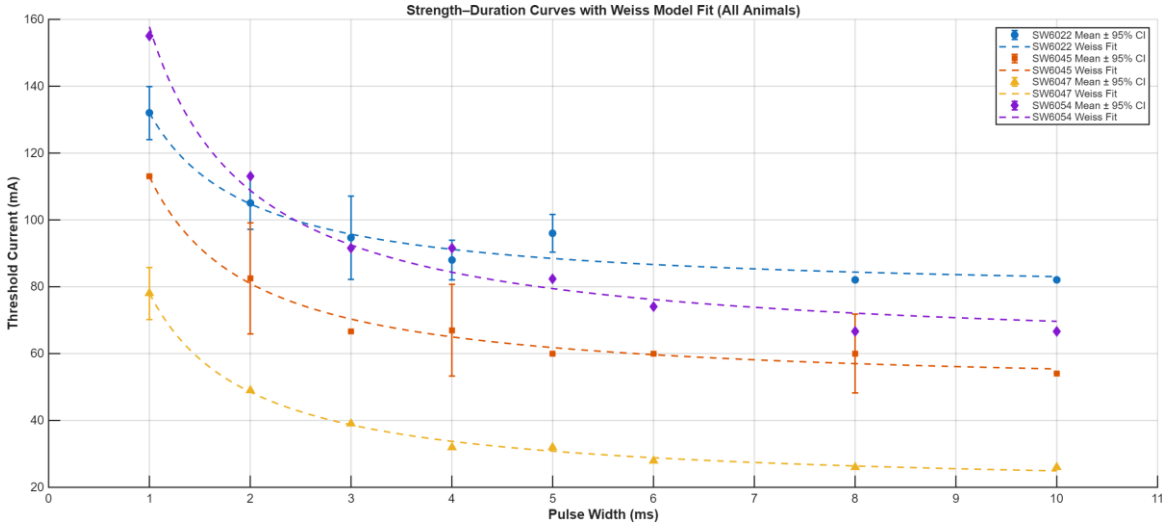


Figure 14. Strength-duration characteristics of subcutaneous pacing in four swine. Symbols represent mean threshold current at each pulse width (1-10 ms), error bars are 95% CIs where replicate trials were available (n=1-4 per condition, no error bars n=1). Dashed curves are Weiss-Lapicque fitted curves, Equation 4, yielding the rheobase Irh (mA) and chronaxie τc (ms). Thresholds fall steeply from 1-4 ms and approach an asymptote at longer pulse durations, demonstrating classical excitability behaviour with marked between-animal variability. For SW6045 and SW6047, monophasic and biphasic data were pooled because the waveforms showed no significant impact on threshold (p=0.926, GLM Pooled).

The observed behaviour is consistent with the foundational electrophysiological principles described by Weiss and Lapicque, in which excitation is governed by the interaction between stimulus strength and duration. Longer pulse widths allow greater temporal integration of membrane depolarisation, reducing the peak current required to reach excitation threshold. Notably, these classical relationships were preserved despite the absence of direct myocardial contact, confirming that subcutaneous stimulation can generate a sufficient electric field within the myocardium to elicit capture.

Fitting the Weiss-Lapicque model to the subject-specific data yielded estimates of rheobase and chronaxie for each animal, as summarised in **Table 7**. These parameters demonstrated substantial inter-subject variability, with rheobase values ranging from 19.01 mA to 77.58 mA and chronaxie values from 0.70 ms to 3.11 ms. Rheobase and chronaxie values demonstrated a consistent inverse relationship across stimulation conditions. Higher rheobase currents were associated with shorter chronaxies, whereas lower rheobase currents were associated with longer chronaxies. This inverse coupling was observed across all tested configurations, reflecting a trade-off between stimulus strength and duration.

Table 7. Subject-specific rheobase and chronaxie for subcutaneous pacing. Rheobase (mA) and chronaxie (ms) were estimated from Weiss-Lapicque fits to each animal's strength-duration data, with pulse widths ranging from 1 to 10 ms. Values illustrate marked intersubject variability and an inverse pattern between rheobase and chronaxie. For SW6045 and SW6047, monophasic and biphasic data demonstrated no significant impact on threshold, with p-values of 0.93 and 1.0, respectively**.**

Animal	Rheobase (mA)	Chronaxie (ms)
SW6022	77.58	0.70
SW6045	49.02	1.31
SW6047	19.01	3.11
SW6054	59.86	1.64

A highly significant subject was identified ($F=335.51$, $p < 0.001$), with an absolute threshold difference of approximately 30-40 mA observed between animals. This variability likely reflects differences in electrode positioning, tissue composition and transthoracic impedance, all of which influence current distribution and effective field strength at the myocardial surface. While direct measurements of these parameters were not obtained, the magnitude and consistency of the observed differences support a physiological and geometric basis rather than an experimental artefact.

Two animals, SW6045 and SW6047, were tested using both monophasic and biphasic waveforms at each pulse width, enabling the study to assess the impact of a two-phase stimulus profile relative to a single-phase pulse. Pooled analysis using a general linear model demonstrated no significant effect from waveform ($p = 0.926$), with an estimated effect size of less than 1 mA. This indicates that, under the conditions tested, monophasic and biphasic stimuli produce equivalent peak current requirements for myocardial capture. This

observation contrasts with prior studies reporting reduced thresholds with biphasic stimulation; however, the present findings suggest that such effects may not translate to the subcutaneous stimulation domain. The efficacy of biphasic stimulation can depend on the timing between the positive and negative pulses, referred to as the interphase delay. The biphasic pulses implemented in this study had minimal interphase delay. If the timing or phase symmetry was suboptimal for the myocardium, the second phase may not have contributed effectively to the recruitment of additional cardiac fibres. These findings suggest that waveform-dependent advantages observed in lower energy transvenous systems may not translate to the subcutaneous stimulation domain.

Although biphasic waveforms are known to reduce net charge delivery and may confer advantages for tissue safety, the threshold criterion employed in this study was based solely on successful capture. As such, it would not necessarily be reflected in peak current measurements. The absence of a waveform effect therefore suggests that, in this context, the excitation threshold is governed primarily by the peak field achieved at the myocardium rather than the temporal distribution of charge.

Collectively, these findings demonstrate that subcutaneous pacing follows classical strength-duration principles, with substantial inter-subject variability and minimal dependence on waveform morphology. This has important implications for the design and optimisation of extravascular cardiac stimulation systems, where anatomical variability and field distribution may play a more dominant role than waveform configuration in determining capture thresholds.

3.4. Discussion

The strength-duration profiles observed across all animals indicate that myocardial excitation during subcutaneous stimulation remains aligned by classical excitability behaviour, despite the difference in electrode placement of the extravascular configuration.[74] Across subjects, threshold current decreased with increasing pulse width, producing the expected hyperbolic strength-duration relationship.[75] This finding suggests that, although the stimulus was delivered through intervening subcutaneous and thoracic tissue rather than by direct endocardial contact, the underlying myocardial response remains consistent with established principles of electrical stimulation.[74,75]

Over a century ago, researchers such as Weiss (1901) and Lapicque (1907) demonstrated that excitation follows a strength–duration relationship, whereby the threshold current decreases hyperbolically with increasing pulse duration.[74] Within this framework, rheobase represents the minimum current required to produce excitation at very long pulse durations.

The concept details a point at which no further increase in pulse duration is required for the impact capture threshold.[76] Chronaxie represents the pulse duration required to achieve excitation at twice the rheobase current. These parameters provide quantitative descriptors of excitability and allow comparison between stimulation configurations.[37,76]

All four animals exhibited measurable rheobase currents ranging from 19 to 77 mA and chronaxies ranging from 0.7 to 3.1 ms. The fitted strength-duration curves showed strong agreement with the classical hyperbolic model with R^2 values of approximately 0.97 for each animal. The strong agreement with hyperbolic strength-duration behaviour indicates that myocardial excitability under subcutaneous stimulation follows classical excitation principles, even when the stimulus is delivered at a distance through intervening tissue rather than via direct intracardiac contact. These findings support the conclusion that subcutaneous myocardial capture is not determined solely by stimulus amplitude, but instead follows predictable pulse-width-dependent behaviour.

An inverse relationship was observed between rheobase and chronaxie across subjects, such that animals with higher rheobase currents consistently exhibited shorter chronaxies, whereas those with lower rheobase currents showed longer chronaxies. Animals SW6022 and SW6054, which exhibited the highest rheobase currents, also demonstrated the shortest chronaxies Table 7. This inverse coupling reflects a physiological trade-off between stimulus strength and duration that is characteristic of excitable tissue.[75] Potential contributors to this variability include differences in tissue impedance, electrode geometry and the relative position of the subcutaneous coil with respect to the myocardium. While these parameters were not directly measured in the present study, the observed pattern is consistent with established effects of tissue conductivity, electrode spacing and electric field distribution on excitation thresholds. Therefore, inter-animal variability should be interpreted not as a failure of the strength-duration model, but as evidence that extravascular stimulation thresholds are highly dependent on the anatomical and electrical properties of the stimulation pathway.

The study provides a useful benchmark for the current and energy requirements associated with myocardial capture using a subcutaneous electrode configuration. The currents required for myocardial capture via subcutaneous stimulation were markedly higher than those reported for transvenous leads. At shorter pulse widths, capture thresholds routinely exceeded 100 mA, indicating that the energy required for subcutaneous pacing is substantially greater relative to that of directly coupled endocardial configurations, where thresholds are typically achieved at much lower currents.

Compared with transcutaneous pacing, which delivers 50-100 mA at pulse widths of 20-40 ms, the subcutaneous vector reduces impedance.[21] However, despite this reduction, subcutaneous pacing still requires substantially higher currents than directly coupled endocardial or epicardial configurations, reflecting the increased distance between the stimulating electrode and the myocardial tissue. This distinction is important as it demonstrates that subcutaneous pacing occupies an intermediate position between external transcutaneous pacing and intracardiac stimulation, less demanding than stimulation through the intact chest wall, but substantially less efficient than direct myocardial or endocardial contact.

The results also help contextualise the rationale behind the evolution of the EV-ICD architecture.[65] By positioning the lead in the substernal space, closer to the anterior surface of the heart, EV-ICD systems reduce the tissue barrier between the stimulating electrode and the myocardium.[77] This anatomical change provides a plausible explanation for the lower pacing thresholds reported with substernal lead systems compared with gully subcutaneous vectors. Although EV-ICD systems avoid transvenous lead placement, substernal implantation introduces distinct procedural considerations related to the anterior mediastinal anatomy. Early clinical studies have reported system or procedure-related complications requiring continued evaluation.[28,77]

The findings also provide context for modular approaches that combine a subcutaneous ICDs with a separate intracardiac leadless pacemaker. In such systems, defibrillation protection remains extravascular, while pacing is delivered from direct contact with the myocardium. This architecture avoids the high-energy requirements observed with fully subcutaneous pacing while preserving the principal advantage of avoiding transvenous defibrillation leads.

The findings of this study present both challenges and an opportunities for informing the development of next-generation cardiac devices. The high capture thresholds observed suggest that any pacing-enabled subcutaneous ICD platform would require substantially greater energy reserves than those of current non-pacing systems. This has implications not only for battery longevity, but also for thermal management, lead integrity, device size and overall system. The preservation of a predictable strength-duration relationship suggests that waveform optimisation may provide a practical route to reducing peak current requirements while maintaining reliable myocardial capture. In this context, pulse width selection becomes a key design variable rather than a fixed pacing parameter.

Interestingly, the anticipated advantages of biphasic waveforms were not realised under the tested conditions. [50,54–56]. The absence of a statistically significant reduction in threshold ($p = 0.926$) may be related to the waveform parameters employed, particularly in optimising

interphase delays. It is also plausible that at higher field strengths, the nonlinear response of the surrounding tissue masks any benefit conferred by charge balancing. Therefore, these data should not be interpreted as evidence that biphasic stimulation has no role in extravascular pacing, but rather that the specific biphasic configuration tested here did not reduce capture thresholds under the conditions studied.

3.5. Limitations

Several limitations should be acknowledged. The study was conducted in four swine. While this cohort demonstrated consistent trends within the study, it was not large enough for definitive population-level conclusions. Swine were chosen because their thoracic anatomy offers a relevant preclinical model for human subcutaneous cardiac stimulation; however, variations in anatomy, adipose tissue density, and electrode placement relative to the heart among subjects may have influenced threshold measurements. A larger sample size would be necessary to better characterise the distribution of rheobase and chronaxie within a population. Nevertheless, the consistent qualitative findings across all animals suggest that the observed behaviors reflect underlying physiological mechanisms rather than experimental variability or minor sample differences.

The experiments were conducted acutely, with electrodes implanted and tested in a single session under general anaesthesia. In a chronic scenario, fibrotic encapsulation around the coil and generator could further increase thresholds over time, as scar tissue increases the system's impedance. Conversely, chronic implants may also enable fibrous stabilisation, preventing any motion of the lead during pulses. Adding a safety margin is a recognised industry standard, generally a two-fold increase, allowing for thresholds that may increase over months or years. Long-term animal studies or clinical data will be necessary to determine how chronic inflammation or fibrosis in the subcutaneous pocket affects pacing thresholds. Early clinical data from systems such as the Aurora EV-ICD suggest that pacing thresholds can remain stable over 6–12 months, although longer-term follow-up is required.

The study employed both monophasic and biphasic waveforms. The parameters of biphasic waveforms, particularly the interphase delays, were not systematically optimised. The finding that biphasic stimulation failed to reduce pacing thresholds in the present study ($p = 0.926$) contrasts with prior reports.[1,13] These studies reported clear advantages in neurostimulation and endocardial pacing, suggesting that additional studies are required to explore the influence of interphase duration, waveform symmetry, and pulse shape in this setting.

3.6. Conclusion

This research provides a characterisation of subcutaneous pacing thresholds and details their dependence on pulse parameters in a controlled preclinical model. The absence of intracardiac leads did not appear to alter the excitability behaviour of the myocardium, as demonstrated by the alignment of the data to classical strength–duration models. The principal difference observed was quantitative rather than qualitative. As expected, due to the increased transthoracic impedance, substantially higher currents and energies were required to achieve subcutaneous capture, while the qualitative excitability remained consistent with established theory.

The first research question investigated whether subcutaneous pacing could reliably achieve myocardial capture. Capture was achieved in all four animals, with rheobase values ranging from 19 to 78 mA and chronaxies from 0.7 to 3.1 ms. These results confirm that subcutaneous pacing is feasible in principle, albeit at a significantly higher energetic cost than endocardial systems.

The second research question explored the influence of pulse duration and waveform type on the strength-duration relationship. Threshold currents required for myocardial capture decreased hyperbolically with increasing pulse width, consistent with classical excitability models. No statistically significant differences were observed between monophasic and biphasic stimulation conditions ($p = 0.926$). It is important to note that the study was not specifically designed to optimise waveform parameters, such as interphase delay or symmetry. The absence of a clear advantage of biphasic stimulation should be interpreted with caution and necessitates additional testing and interphase optimisation.

By explicitly addressing these research questions, this study provides quantitative evidence that subcutaneous pacing adheres to the same electrophysiological principles that underpin conventional pacing, while quantifying the higher current demands inherent to this configuration. These findings provide a physiological foundation and quantitative benchmarks for the development of next-generation extravascular devices, including pacing-capable subcutaneous ICDs.

The study successfully demonstrated that myocardial tissue can be remotely stimulated via a subcutaneous configuration. As such, the findings align fundamental electrophysiological principles with innovative device design. This contribution supports the wider thesis aim of advancing safe and effective alternatives to transvenous cardiac pacing systems.

Chapter 4 Ventricular Fibrillation Induction Characteristics

4.1. Introduction

Sudden cardiac death (SCD) remains a major contributor to global mortality and represents a significant public health challenge. Cardiovascular disease (CVD) accounts for approximately 19.8 million deaths annually, corresponding to 32% of global mortality, with the majority attributable to myocardial infarction and stroke.[2] Sudden cardiac arrest (SCA), which frequently underlies SCD, is estimated to account for approximately 30% of cardiovascular deaths, representing over 5 million cases annually.[78] While ventricular fibrillation (VF) has historically been considered the dominant arrhythmia responsible for SCA, contemporary data indicate that asystole and pulseless electrical activity are more commonly observed in the general population, with VF accounting for approximately 20% of cases.[78] Despite this, VF remains a critical arrhythmic manifestation, particularly in early-phase ischaemic events and in cases where rapid defibrillation can significantly improve survival outcomes.[79]

The development and clinical adoption of implantable cardioverter defibrillators (ICDs) have revolutionised the prevention of SCD. ICDs provide both primary and secondary prevention by continuously monitoring the heart's electrical activity.[80] Over the past several decades, ICD systems have become established as a cornerstone in the management of patients at risk from primary or secondary SCD.[80] Continuous advancements in device design, sensing algorithms, and therapy delivery have contributed to their widespread adoption and demonstrated effectiveness in terminating life-threatening ventricular arrhythmias.[81] In the event that an ICD detects a ventricular tachycardia or ventricular fibrillation, the device delivers a high-energy shock, defibrillating the heart with the aim of terminating the arrhythmia.[12] However, as discussed in Chapter 3, complications associated with intravascular leads, such as lead infection, fracture, venous occlusion and extraction-related morbidity, have driven the development of newer subcutaneous (S-ICD) and extravascular (EV-ICD) systems that eliminate the need for transvenous access.[61,66]

S-ICDs differ significantly from transvenous systems. In S-ICDs, both the electrode and pulse generator are implanted outside the heart and vasculature, with the electrode positioned subcutaneously along the parasternal region and the pulse generator on the left thoracic wall.[12,22,64] As a result, the shock vector traverses a greater volume of heterogeneous, low-conductivity tissue before reaching the myocardium, thereby altering shock propagation, tissue impedance, and myocardial activation thresholds.[29] Finite-element modelling studies further indicate that subcutaneous electrode and generator position influence myocardial

electric-field distribution and estimated defibrillation efficacy. [69] These biophysical differences have direct implications for defibrillation testing, the intraoperative procedure used to ensure the device can effectively detect and terminate induced VF. [82]

Defibrillation Threshold Testing (DFT) testing involves the controlled induction of ventricular fibrillation, followed by the delivery of a therapeutic shock to assess successful arrhythmia termination.[64,82] Although the induction of VF may appear counterintuitive, it is a well-established component of device implantation protocols. The DFT is defined as a probabilistic measure, representing the minimum energy at which defibrillation is successful, historically requiring two consecutive successful shocks.[81] In clinical settings during implant, DFT testing serves to confirm system integrity in vivo.[83] During defibrillation testing, VF is induced under controlled conditions to confirm that the implanted system can appropriately detect the arrhythmia and deliver an effective shock. The procedure also assesses the defibrillation safety margin, providing confidence that programmed therapy energies exceed the tested minimum required for successful VF termination. [83]

In contemporary practice, however, the role of routine DFT testing has been fundamentally re-evaluated.[83,84] Pivotal randomised trials, including SIMPLE and NORDIC ICD, have demonstrated that omission of routine intraoperative VF induction and defibrillation testing is non-inferior with respect to shock efficacy and clinical outcomes, including arrhythmic mortality. These findings are supported by substantial technological advancements in ICD systems, which have improved defibrillation reliability and reduced the incidence of inadequate safety margins. As a result, routine DFT testing is no longer recommended in standard left-sided ICD implantations.[83,84]

In contrast to transvenous ICD systems, intraoperative defibrillation efficacy testing has historically remained a Class 1 recommendation for S-ICD implantation, indicating that the procedure was considered recommended on the basis that its benefit and usefulness were supported by the available evidence and/or expert consensus. The 2015 HRS/EHRA/APHRS/SOLAECE expert consensus statement specifically classified defibrillation efficacy testing during S-ICD implantation as Class I, Level of Evidence C-LD.[85] This recommendation reflects the fundamentally different sensing and shock-delivery characteristics of extravascular systems, including the absence of a direct electrode-myocardium interface, greater variability in sensed signal amplitude, and increased dependence on the electrode position and the pulse generator.[82] The PRAETORIAN-DFT trial now provides randomised evidence that routine defibrillation testing may be safely omitted in selected de novo S-ICD implants when guided by PRAETORIAN score

assessment. These findings should be interpreted as evidence supporting a potential shift toward selective testing rather than as a removal of the current Class 1 recommendation. VF induction remains relevant in current S-ICD practice, particularly where testing is clinically indicated, implant position is uncertain, PRAETORIAN score is elevated, system revision is performed, or future extravascular ICD platforms are being evaluated.[86]

It is important to note that in the context of S-ICDs, the term DFT is somewhat of a misnomer. Unlike transvenous ICD systems, in which shock energy can be titrated to identify the minimum effective defibrillation threshold, the S-ICD delivers a fixed, non-programmable output of 80 J.[51] Although the S-ICD can deliver shocks up to 80 J, intraoperative testing commonly evaluates successful conversion at a lower test energy to preserve a safety margin.[81,82] Consequently, intraoperative defibrillation testing in S-ICD practice primarily serves to assess conversion efficacy and confirm adequate VF detection, shock vector configuration, system impedance, and successful arrhythmia termination.[51,82]

The PRAETORIAN and PRAETORIAN-DFT studies represent key prospective investigations evaluating S-ICD defibrillation strategies.[64,86,87] Central to this approach is the PRAETORIAN score, a radiographic assessment tool derived from bidirectional chest radiographs that evaluates S-ICD system positioning to estimate the likelihood of successful defibrillation.[87] The PRAETORIAN-DFT trial enrolled 965 patients in a multicentre randomised comparison of testing in selected patients undergoing de novo S-ICD implantation. [86] The primary results reported that omission of defibrillation testing was non-inferior to routine testing for failed first shock in spontaneous-ventilation arrhythmias, with failed first shock occurring in 1.7% of patients in the no-defibrillation testing group compared with 2.3% in the defibrillation testing group.[86] The study also reported potential defibrillation testing-related complications in 1.7 % of patients undergoing testing, supporting the procedural rationale of selective rather than universal testing.[86]

As such, the PRAETORIAN-DFT study represents the first large-scale randomised effort to evaluate a structured, imaging-guided strategy for the selective omission of defibrillation testing in S-ICD implantation. The findings support a transition from universal routine DF testing towards a more selective, imaging-guided strategy in de novo S-ICD implantation. However, they do not eliminate the relevance of VF induction. Rather, they shift the clinical question from whether VF induction should be performed routinely to when it remains necessary and how it can be performed safely and efficiently. VF induction remains pertinent for selected patients, suboptimal or uncertain implant positioning, elevated PRAETORIAN scores, system revisions, preclinical validation, and the development of future lower-energy extravascular ICD platforms.[64,65,86–88]

Traditional transvenous ICD systems achieve VF induction through well-characterised mechanisms such as shock on T, burst pacing or direct current stimulation.[81] These strategies exploit fundamental electrophysiological mechanisms, whereby rapid or premature stimulation results in shortened diastolic intervals and nonuniform recovery of excitability, facilitating conduction block, wave break and the initiation of re-entrant activity leading to VF.[89] In contrast, S-ICDs utilise an entirely subcutaneous stimulation vector, introducing distinct patterns electric-field distribution between the electrode, generator and myocardium.[69] The standard S-ICD induction protocol, outlined in the manufacturer's technical document, applies a fixed non-adjustable 200 mA, 50 Hz biphasic stimulus across the coil to can vector. While this approach successfully induces VF in the majority of patients, it is empirically derived rather than mechanistically optimised.[51]

Electrical stimulation parameters, including pulse width, frequency and amplitude, are fundamental determinants of myocardial excitability, with variation in these parameters directly modulating stimulation thresholds and the likelihood of VF induction.[23–25,89,90] Yet their relative contribution to VF initiation within the subcutaneous field remains poorly defined. Moreover, S-ICDs use a 9 V lithium manganese dioxide (Li-MnO2) battery, which limits device miniaturisation compared to 3 V systems, employed in modern transvenous ICDs. Future device versions will require lower-voltage operation and more energy-efficient induction protocols, emphasising the importance of understanding the biophysical limits of VF initiation in subcutaneous systems.

One critical yet underexplored factor in subcutaneous VF induction is the average current delivered during stimulation. Peak current describes the instantaneous current amplitude required to initiate myocardial excitation, whereas average pulse-train current reflects the cumulative electrical burden imposed by the combined effects of pulse width, stimulation frequency and train duration. Experimental defibrillation studies conducted by Chen et al. demonstrated that current measurements can provide information beyond delivered energy alone. In a porcine VF model, average current was reported as a better descriptor of therapeutic dose than peak current for defibrillation waveforms.[91] Similarly, cardiac stimulation studies demonstrate that pulse duration is closely linked to stimulation efficiency, both in terms of excitability and energy demand.[92] In S-ICD systems, where current must traverse heterogeneous thoracic tissues before reaching the myocardium, electrode and generator positions influence the myocardial electric field distribution and defibrillation efficacy.[69] Commercialised S-ICD induction protocols use a fixed stimulation profile of 50 Hz, 200 mA, rather than explicitly optimising average pulse-train current.[51] Therefore, understanding how pulse width and frequency influence both peak and average current may

be important for improving induction reproducibility, reducing unnecessary electrical exposure and informing the design of more energy-efficient future extravascular ICD platforms.

4.2. Research Question

The central research question addressed in this study is:

How do electrical waveform parameters influence ventricular fibrillation induction thresholds and associated energy requirements under subcutaneous stimulation condition?

This preclinical study aimed to characterise ventricular fibrillation induction under subcutaneous stimulation using a porcine model designed to replicate clinically relevant S-ICD stimulation configurations. The objectives included:

1) To quantify ventricular fibrillation induction thresholds across a defined range of pulse width, frequency, and amplitude.
2) To evaluate the influence of pulse width and frequency on VF induction under subcutaneous stimulation conditions.
3) To assess the relationship between peak current and average current as complementary measures of stimulation intensity, efficiency and energetic burden.
4) To evaluate the applicability of classical electrophysiological principles, including strength-duration behaviour, to VF induction under subcutaneous conditions characterised by increased electrode-myocardium separation.
5) To inform waveform optimisation strategies for selective VF induction, defibrillation-testing protocols, reduction of induction energy requirements and the development of next-generation S-ICD systems.

4.3. Methods

4.3.1. Subcutaneous Ventricular Fibrillation Induction Testing Preparation

All procedures were conducted in accordance with institutional and national ethical guidelines for the care and use of laboratory animals.[75] The study protocol (Study #17-082N) was reviewed and approved by Boston Scientific's Institutional Animal Care and Use Committee (IACUC). Subjects (n = 3, swine) were selected based on thoracic anatomy and cardiac orientation comparable to adult humans.[72]

Animals were premedicated with intramuscular ketamine (20 mg/kg) and xylazine (2 mg/kg) to facilitate handling and intubation.[73] Mechanical ventilation was provided throughout the procedure, with continuous physiological monitoring including ECG, invasive arterial blood pressure (via a Millar catheter), oxygen saturation (SpO_2), end-tidal CO_2 ($EtCO_2$), and core temperature.

To prevent skeletal muscle contractions during VF induction and to minimise motion-related artefacts or lead dislodgement, vecuronium was administered intravenously (initial bolus: 0.1–0.15 mg/kg) followed by a continuous infusion rate of 0.1–0.2 mg/kg/hr.[73]

Surgical preparation included positioning each animal in dorsal recumbency. A right jugular venous cutdown was performed to facilitate placement of a transvenous ICD lead (Endotak Reliance™, Boston Scientific). The lead was advanced under fluoroscopic guidance to the right ventricular apex and secured using a non-absorbable suture.

Arterial access was obtained via percutaneous femoral artery cannulation, and a high-fidelity Millar pressure catheter (Millar Inc.) was advanced into the thoracic aorta to enable real-time hemodynamic monitoring.

For subcutaneous delivery of electrical stimuli, a standard S-ICD electrode was implanted along the right parasternal margin via a subxiphoid incision and tunnelling approach, replicating clinically relevant electrode positioning.[12,93] The electrode was secured at both ends using non-absorbable sutures. A non-functional subcutaneous generator can was implanted in the left lateral thoracic region to complete the coil-to-can vector, consistent with clinical device configurations, as detailed in **Figure 9**, Section 3.2.1.

All incisions were closed in anatomical layers using absorbable and non-absorbable sutures as appropriate. Animals were allowed to stabilise for a minimum of 15 minutes prior to the initiation of stimulation protocols.

4.3.2. Subcutaneous Ventricular Fibrillation Testing Method

Ventricular fibrillation induction testing was performed using a coil-to-can subcutaneous electrode configuration, replicating clinical S-ICD systems. The aim was to evaluate how pulse train parameters, specifically pulse width, frequency and amplitude, affect the success rate of ventricular fibrillation induction.

Each trial began with a pulse train delivered asynchronously from the subcutaneous coil to the generator can. Pulse trains consisted of biphasic square waveforms with pulse widths ranging from 1-8.6 ms at the following set frequencies: 10, 20, 30 and 50 Hz. Testing commenced with an amplitude below the expected capture threshold, typically 50-100 mA. From this starting point, the current was incrementally increased in steps of 10 mA or 10% until VF was induced or the train was completed without arrhythmogenic effect.

VF induction was confirmed via ECG, hemodynamic collapse, and invasive pressure monitoring. Following each induction, animals were promptly defibrillated back to normal sinus rhythm (NSR) using an internal RV shock, typically 30-40 J delivered through the transvenous ICD lead system. A short recovery period was observed between trials to allow complete hemodynamic stabilisation, prior to proceeding.

4.4. Results

This study builds on the findings from Chapter 3. Where preclinical testing assessed subcutaneous pacing, to characterise the rheobase and chronaxie characteristics of myocardial capture. This study investigates the electrophysiological factors influencing the induction of ventricular fibrillation (VF) via subcutaneous stimulation. Pacing-derived excitability metrics, rheobase and chronaxie, are cited throughout to evaluate each animal's susceptibility to VF. This section presents both individual animal results and a cohort analysis, assessing the impact of pulse width and frequency in the determination of peak and average current requirements to induce VF.

4.4.1. Subject-Specific VF Induction Threshold

Ventricular fibrillation induction thresholds were characterised for each of the three animals across a range of waveform configurations. The protocol tested pulse widths from 1 to 8.6 ms and frequencies between 10 to 50 Hz. VF induction threshold was defined as the minimum peak current required to reliably initiate fibrillation. Per industry standards, 2-5 replicate trials were performed. The study also incorporated the animals' rheobase and chronaxie, which were derived in Chapter 3, to contextualise cardiac excitability. In addition to peak current, the corresponding average current for each stimulation condition was

calculated. This approach enabled a comparison of the instantaneous excitation threshold, peak current, and the cumulative energy of waveform delivery with the average current.

Test conditions in which stimulus currents exceeded the device's output limit of 400 mA were excluded from the statistical analysis. They were classified as censored measurements rather than true physiological thresholds. As a result, summary statistics for these conditions only reflect successful sub-threshold inductions.

The average current delivered during each stimulation train was calculated to estimate the total electrical load applied over time. While peak current defines the instantaneous stimulus amplitude responsible for myocardial excitation, average current reflects the cumulative energetic burden associated with waveform delivery.

The average current of the biphasic pulses was determined by the waveform duty cycle. The duty cycle is given by

Equation 2. Duty Cycle

$$Duty\ Cycle = \left(\frac{2 * PW}{T}\right)$$

Where:
PW = Pulse Width (ms)
T = period of stimulation (ms), where $T = \frac{1}{f}$

Equation 3. Average Current

$$I_{avg} = Duty\ Cyle * I_{Peak}$$

Where:
I_{avg} = average current (mA)
I_{peak} = peak current (mA)

Equation 2 and **Equation 3** highlight, that the average current delivered is governed by pulse width duration and stimulation frequency. Increasing pulse width extends the duration of current delivery per pulse, while increasing frequency reduces the inter-pulse interval, thereby increasing the proportion of time during which current is applied. Consequently, waveform configurations that reduce peak current requirements will increase cumulative energy delivery.

SW6022

SW6022 recorded the highest subcutaneous pacing threshold of the tested animals, with a rheobase of 77.58 mA and a chronaxie of 0.70 ms. A total of 23 stimulation conditions were evaluated. All pulse trains consisted of biphasic waveforms with a fixed 1.5 ms interphase delay. Each waveform condition was repeated up to four times. Peak current thresholds are summarised in

Table 8, and corresponding average current thresholds are presented in **Table 9**. When stimulus profiles of shorter pulse widths and lower stimulation frequencies were tested, the current required for VF induction approached the system output limit of 400 mA. Significant skeletal capture was observed at these higher currents. At 2 ms and 20 Hz, VF induction required 360 mA (n = 1), whereas at 4 ms and 20 Hz the mean peak current was 333.75 mA (95% CI: 280.97 to 386.53; n = 4). By contrast, longer pulse widths and higher stimulation frequencies were associated with substantially lower VF thresholds. At 8.6 ms and 50 Hz, VF was induced at a mean peak current of 122.50 mA (95% CI: 102.82 to 142.18; n = 4), representing the lowest threshold observed in this subject.

A corresponding increase in average current was observed under waveform conditions with lower peak-current thresholds. At 4 ms and 20 Hz, the mean average current was 53.40 mA (95% CI: 44.96 to 61.84; n = 4), increasing to 54.46 mA (95% CI: 32.52 to 80.40; n = 4) at 4 ms and 30 Hz, and to 105.35 mA (95% CI: 88.42 to 122.28; n = 4) at 8.6 ms and 50 Hz.

The peak and average current trends are illustrated in **Figure 15**. **Figure 15**A. shows that the peak current reduced with increasing pulse width and frequency, whereas **Figure 15**B shows that the average current increased under the same waveform condition.

Table 8. Mean Peak current (mA) required for VF induction in SW6022 as a function of pulse width (ms) and frequency (Hz). Values shown as mean ±95% CI; n=1-4 replicates per condition

Pulse Width (ms)	Frequency (Hz)	Mean (mA)	Min (mA)	Max (mA)	N	95% CI Lower (mA)	95% CI Upper (mA)
8.6	50	122.50	113	139	4	102.82	142.18
4	50	155.00	155	155	2	--[1]	--[1]
2	50	262.00	262	262	2	--[1]	--[1]
4	30	235.25	191	324	4	135.49	335.01
4	20	333.75	291	360	4	280.97	386.53
2	30	324.00	324	324	4	324.00	324.00
2	20	360.00	360	360	1	--[1]	--[1]

Table 9. Mean Average currents (mA) during VF-induction pulse trains in SW6022. Values shown as mean ±95% CI, for each pulse width (ms) and frequency (Hz) combination (n =2-4). Average current is the time-averaged current over the pulse train.

Pulse Width (ms)	Frequency (Hz)	Mean (mA)	Min (mA)	Max (mA)	N	95% CI Lower (mA)	95% CI Upper (mA)
8.6	50	105.35	97.18	119.54	4	88.42	122.28
4	50	62.00	62.00	62.00	2	--[1]	--[1]
2	50	52.40	52.40	52.40	2	--[1]	--[1]
4	30	56.46	45.84	77.76	4	32.52	80.40
4	20	53.40	46.56	57.60	4	44.96	61.84
2	30	38.88	38.88	38.88	4	38.88	38.88
2	20	30.99	28.80	32.08	1	26.28	35.69

[1] -- Confidence intervals and standard deviations were not calculated for groups with fewer than three observations (n ≤ 2) due to insufficient sample size and the resulting instability of estimates. For these cases, descriptive statistics (mean, median, range) are reported only

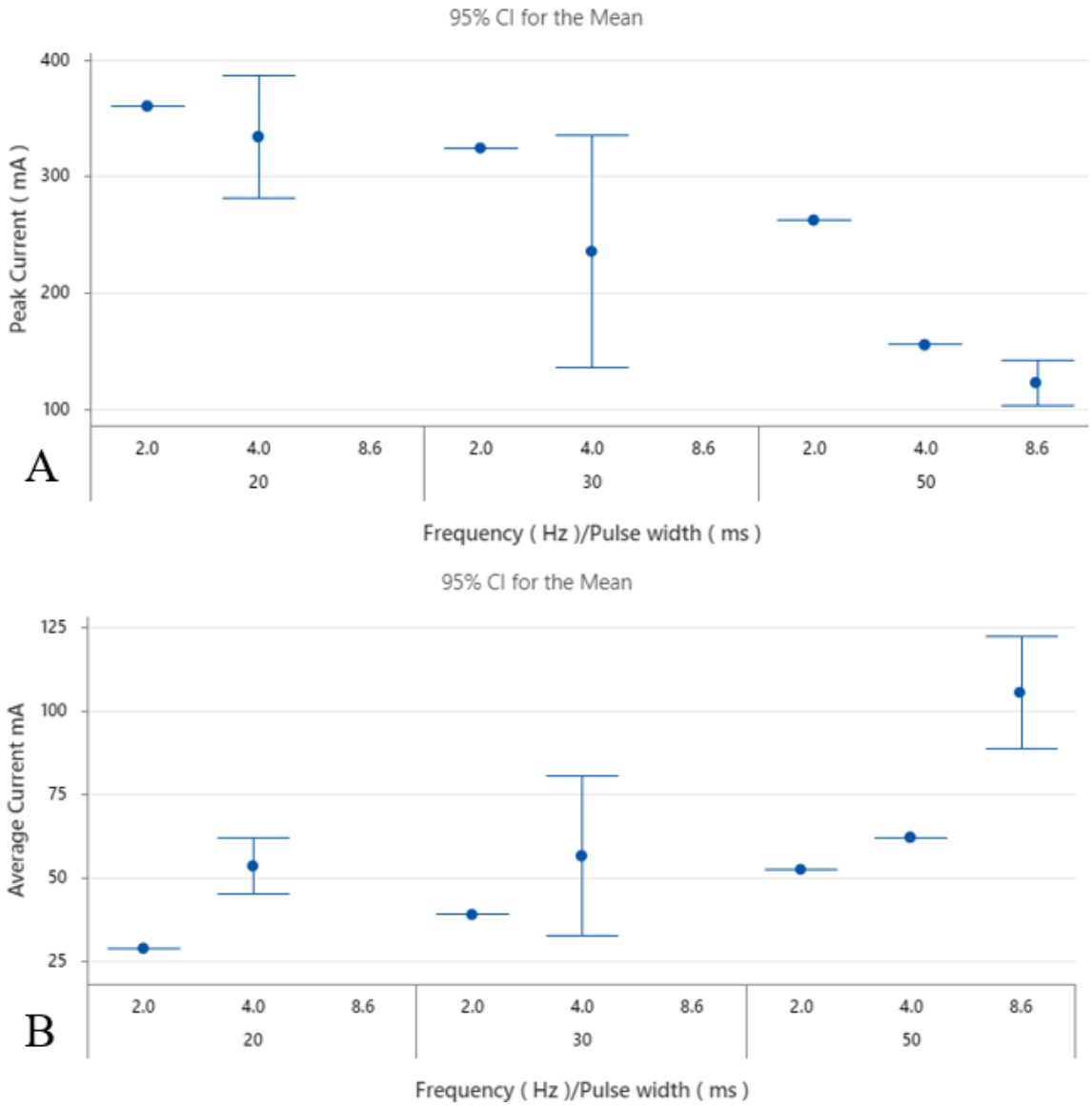


Figure 15. Relationship between waveform parameters and VF induction thresholds in SW6022. (A) Mean peak current (± 95% CI) vs stimulation frequency grouped by pulse width. (B) Corresponding average current (± 95% CI). Longer pulse widths and higher frequencies lowered peak current while increasing average current.

SW6045

SW6045 was evaluated using the same stimulation protocol, with biphasic waveforms delivered across a range of pulse widths and stimulation frequencies via the subcutaneous coil to can vector. Following the exclusion of the three trials at 1 ms and 10 Hz, in which peak current exceeded the device limit (≥400 mA), a total of 37 stimulation conditions were analysed. Peak current thresholds are summarised in Table 10, with corresponding average current values presented in Table 11.

As reported in Chapter 3 **Table 7**, SW6045 recorded an increased myocardial excitability relative to SW6022, with a rheobase of 49.02 mA and a chronaxie of 1.31 ms. Consistent with this, lower peak current thresholds were observed across comparable stimulation conditions.

As detailed in SW6022, stimulus profiles of shorter pulse widths and lower frequencies required higher peak current thresholds for VF induction. At 1 ms and 30 Hz, the mean peak current was 292.33 mA (95% CI: 215.27 to 369.40; n = 3). Similarly, at 2 ms and 20 Hz, the mean peak current was 256.80 mA (95% CI: 242.36 to 271.24; n = 5). Increasing pulse width and frequency was associated with lower peak current thresholds. At 2 ms and 50 Hz, the mean peak current decreased to 178.33 mA (95% CI: 151.08 to 205.58; n = 5). At 8.6 ms and 50 Hz, the mean peak current was 120.00 mA (95% CI: 67.87 to 172.13; n = 5).

A corresponding increase in average current was observed under waveform conditions with lower peak-current thresholds. At 1 ms and 30 Hz, the mean average current was 17.54 mA (05% CI: 12.92 to 22.16; n = 3). This increased to 25.53 mA(95% CI: 23.15 to 27.90; n = 5) at 2 ms and 30 Hz, and to 38.98 mA (95% CI: 33.08 to 44.87; n = 5) at 4 ms and 30 Hz. At 8.6 ms and 50 Hz, the mean average current reached 103.20 mA (95% CI: 58.37 to 148.03; n = 5).

These trends are illustrated in **Figure 16**. **Figure 16**A. demonstrates that peak current decreased with increasing pulse width and frequency, while **Figure 16**B shows that average current increased under the same conditions.

Table 10. Mean peak currents (mA) required for VF induction in SW6045 across varying pulse widths (ms) and stimulation frequencies (Hz). Values are presented as mean ±95% CI; n=3-5 replicates per condition. Conditions at 1 ms and 10 Hz were excluded because peak currents exceeded 400 mA.

Pulse Width (ms)	Frequency (Hz)	Mean (mA)	Min (mA)	Max (mA)	N	95% CI Lower (mA)	95% CI Upper (mA)
1	30	292.33	262	324	3	215.27	369.40
2	20	256.80	236	262	5	242.36	271.24
2	30	212.72	191	236	5	192.94	232.50
2	50	178.33	172	191	3	151.08	205.58
4	10	271.67	262	291	3	230.07	313.26
4	20	195.26	191	212	5	183.64	206.88
4	30	162.40	139	191	5	137.82	186.98
8.6	20	205.00	191	212	3	174.88	235.12
8.6	50	120.00	91.5	191	5	67.87	172.13

Table 11. Mean average current (mA) per pulse train in SW6045 for each pulse width (ms) and frequency (Hz). Values are mean ±95% CI; n=3-5. Average current increases with pulse width and frequency.

Pulse Width (ms)	Frequency (Hz)	Mean (mA)	Min (mA)	Max (mA)	N	95% CI Lower (mA)	95% CI Upper (mA)
1	10	8.02	8.02	8.02	3	8.02	8.02
1	30	17.54	15.72	19.44	3	12.92	22.16
2	20	20.54	18.88	20.96	5	19.39	21.7
2	30	25.53	22.92	28.32	5	23.15	27.9
2	50	35.67	34.4	38.2	3	30.22	41.12
4	10	21.73	20.96	23.28	3	18.41	25.06
4	20	31.24	30.56	33.92	5	29.38	33.1
4	30	38.98	33.36	45.84	5	33.08	44.87
8.6	20	70.52	65.7	72.93	3	60.16	80.88
8.6	50	103.2	78.69	164.26	5	58.37	148.03

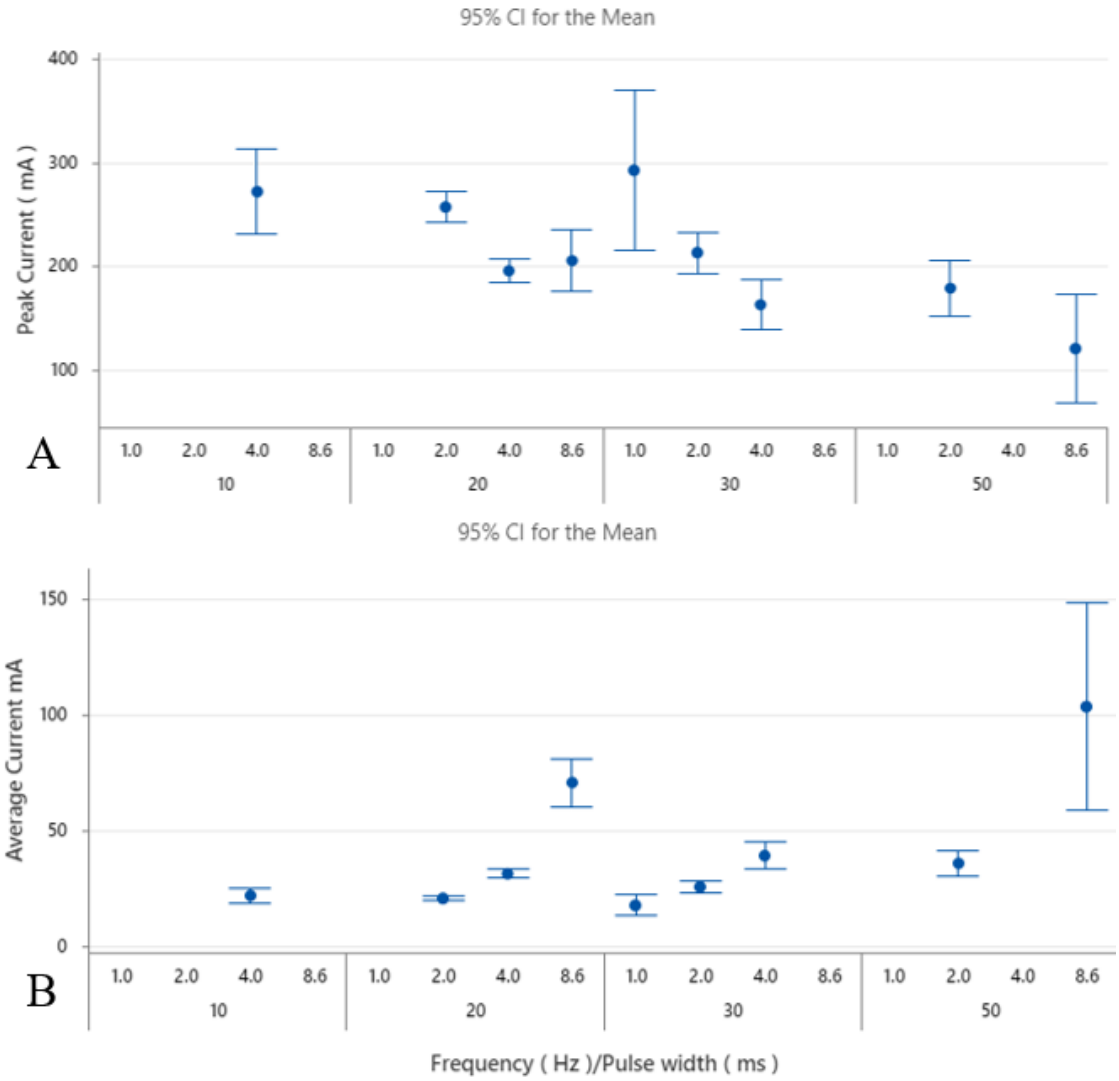


Figure 16. Relationship between waveform parameters and VF induction thresholds in SW6045. (A) Mean peak current (± 95% CI) vs stimulation frequency grouped by pulse width. (B) Corresponding average current (± 95% CI). Data represent 3-5 replicates per condition.

SW6047

Of the three animals tested, SW6047 recorded the highest myocardial excitability, as reflected by the lowest rheobase of 19.01 mA and the longest chronaxie of 3.11 ms. VF induction was assessed across 25 waveform conditions, with peak current thresholds summarised in

Table 12 and corresponding average current values presented in **Table 13**.

Consistent with the other animals tested, short-duration pulses, combined with low stimulation frequencies, required the highest peak currents to reliably induce VF. At 1 ms and 30 Hz, the mean peak current was 293.00 mA (range: 262-324 mA; n = 2). At 2 ms and 20 Hz, VF induction required 291.00 mA (95% CI%: 291.00 to 291.00; n = 3), reflecting no observed variability under these conditions. At 2 ms and 30 Hz, the mean peak current was

242.33 mA (95% CI: 64.72 to 419.95; n = 3), indicating substantial variability between replicates.

Increases in frequency or pulse width consistently reduced VF thresholds. At 2 ms and 50 Hz, the peak current reduced to 191.67 mA (95% CI: 141.96 to 241.37; n = 3). At 4 ms and 30 Hz, 160.33 mA (95% CI: 137.39 to 183.28; n = 3). The lowest peak current was observed at 8.6 ms and 50 Hz, where VF was reduced to 101.00 (95% CI: 101.00 to 101.00; n = 3).

A corresponding increase in average current was observed under waveform conditions with lower peak-current thresholds. At 1 ms and 30 Hz, the mean average current was 19.74 mA (95% CI: 9.36 to 30.12; n = 3). At 2 ms and 50 Hz, this increased to 38.33mA (95% CI: 28.39 to 48.27; n = 3). At 4 ms and 30 Hz, the mean average current was 38.48mA (95% CI: 32.97 to 43.99; n = 3). At 8.6 ms and 50 Hz, the highest average current was observed at 86.86 mA (95% CI: 86.86 to 86.86; n = 3).

These data are illustrated in **Figure 17**. **Figure 17**A. shows that peak current decreased with increasing pulse width and stimulation frequency, **Figure 17**B shows that average current increased under the same waveform conditions.

Table 12. Peak current (mA) required for VF induction in SW6047 across varying pulse widths (ms) and frequencies (Hz). Data represent mean ± 95% CI; n = 2-3 per condition otherwise specified. Measured currents ≥400 mA were excluded from analysis due to measurement limits

Pulse Width (ms)	Frequency (Hz)	Mean (mA)	Min (mA)	Max (mA)	N	95% CI Lower (mA)	95% CI Upper (mA)
1	30	293.00	262	324	2	--[2]	--[2]
2	20	291.00	291	291	3	0.00	0.00
2	30	242.33	191	324	3	64.72	419.95
2	50	191.67	172	212	3	141.96	241.37
4	10	293.00	262	324	2	--[2]	--[2]
4	20	220.00	212	236	3	185.58	254.42
4	30	160.33	155	171	3	137.39	183.28
8.6	20	172.67	155	191	3	127.93	217.40
8.6	50	101.00	101	101	3	0.00	0.00

Table 13. Mean average current (mA) required for VF induction in SW6047 across pulse width (ms) and frequency (Hz) conditions. Data are reported as ± 95% CI, with median, minimum, maximum,

[2] -- Confidence intervals and standard deviations were not calculated for groups with fewer than three observations (n ≤ 2) due to insufficient sample size and the resulting instability of estimates. For these cases, descriptive statistics (mean, median, range) are reported only

and standard deviation included. Average current indicates the time-averaged current delivered during waveform exposure and provides insights into potential power consumption, energy delivery, and implications for device battery life.

Pulse Width (ms)	Frequency (Hz)	Mean (mA)	Min (mA)	Max (mA)	N	95% CI Lower (mA)	95% CI Upper (mA)
1	20	16.04	16.04	16.04	3	0.00	0.00
1	30	19.74	15.72	24.06	3	9.36	30.12
2	20	23.28	23.28	23.28	3	0.00	0.00
2	30	29.08	22.92	38.88	3	7.77	50.39
2	50	38.33	34.40	42.40	3	28.39	48.27
4	10	26.32	20.96	32.08	3	12.48	40.16
4	20	35.20	33.92	37.76	3	29.69	40.71
4	30	38.48	37.20	41.04	3	32.97	43.99
8.6	20	59.40	53.32	65.70	3	44.01	74.79
8.6	50	86.86	86.86	86.86	3	0.00	0.00

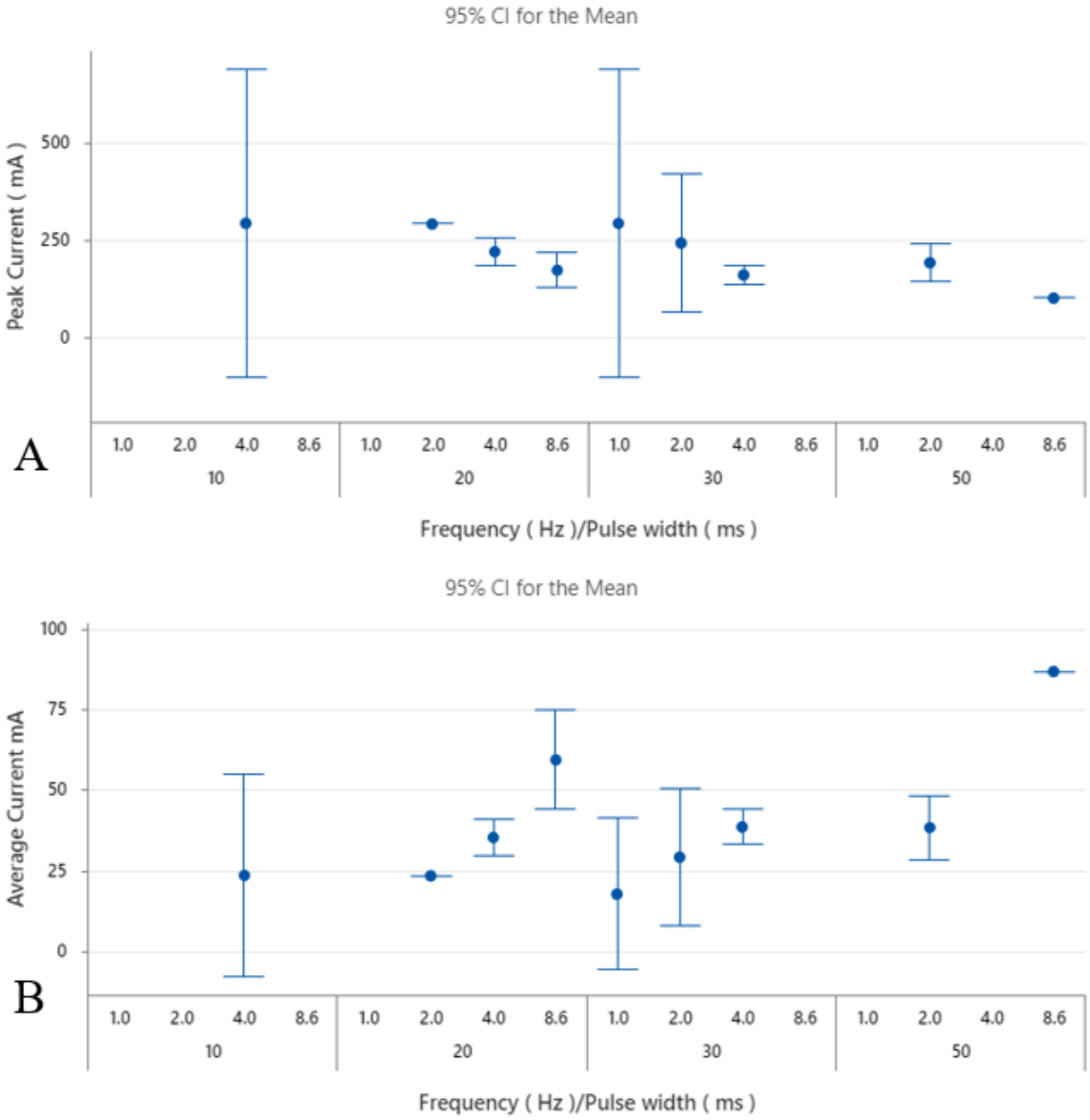


Figure 17. Relationship between waveform parameters and VF induction thresholds in SW6047. (A) Mean peak current (± 95% CI) vs stimulation frequency grouped by pulse width. (B) Corresponding average current (± 95% CI).

4.4.2. Effects of Pulse Width and Frequency on Stimulation Current Requirements.

A factorial design of experiments (DOE) framework was employed to examine the effects of pulse width and stimulation frequency on both average and peak currents during subcutaneous VF induction.

Statistical analysis of the design of experiments (DOE) was performed using Design-Expert® software (Version 10, Stat-Ease Inc., Minneapolis, MN, USA).

4.4.2.1. Influence on Average Current

Average current was assessed to evaluate the effect of pulse parameters on the total current required to induce VF subcutaneously. The factorial model demonstrated statistically

significant results for average current ($F = 39.37$, $p < 0.001$). The model accounted for 91.8% of the variation in average current ($R^2 = 0.918$) with reasonable predictability (predicted $R^2 = 0.76$). Adequate precision was reported at 18.5, which indicated a significant signal relative to background noise. The model assumption was validated by residual analysis. Normal probability plots indicated that the residuals followed the reference line with no major discrepancies. Indicating that the model is robust without transformation.

The main effects of pulse width and frequency on average current are displayed in **Figure 18** A. As expected, based on **Equation 3**, increases in pulse width and frequency resulted in an increase in average threshold currents. This is because pulse width directly increases the duration of current delivery per pulse, while frequency increases the number of pulses delivered per unit time.

Relative contributions of individual factors influencing the average current are detailed in the half-normal plot, **Figure 18** B. Here, pulse width is shown to be the major determinant of the average current. **Figure 18** C. shows that the response curves for different frequency levels are almost parallel across pulse widths. This indicates that pulse width and frequency have independent effects on average current, as evident from the absence of interactions. Consequently, the average current can be expressed as an additive property of charge per pulse. The combined effects of pulse width and frequency are illustrated in the contour plot, **Figure 18** D. There is a clear gradation in response to the average current with increasing pulse width and frequency. The contour lines are more closely spaced along the pulse-width axis, further confirming its dominant influence.

The relationship between predicted and actual values, as indicated in **Figure 18** E demonstrates the model's effectiveness. The scatter plot shows close correlation with all points lying on the unit line. From the analysis, it becomes evident that the average current is mainly determined by cumulative charge delivery. Pulse width is the major determinant of average current.

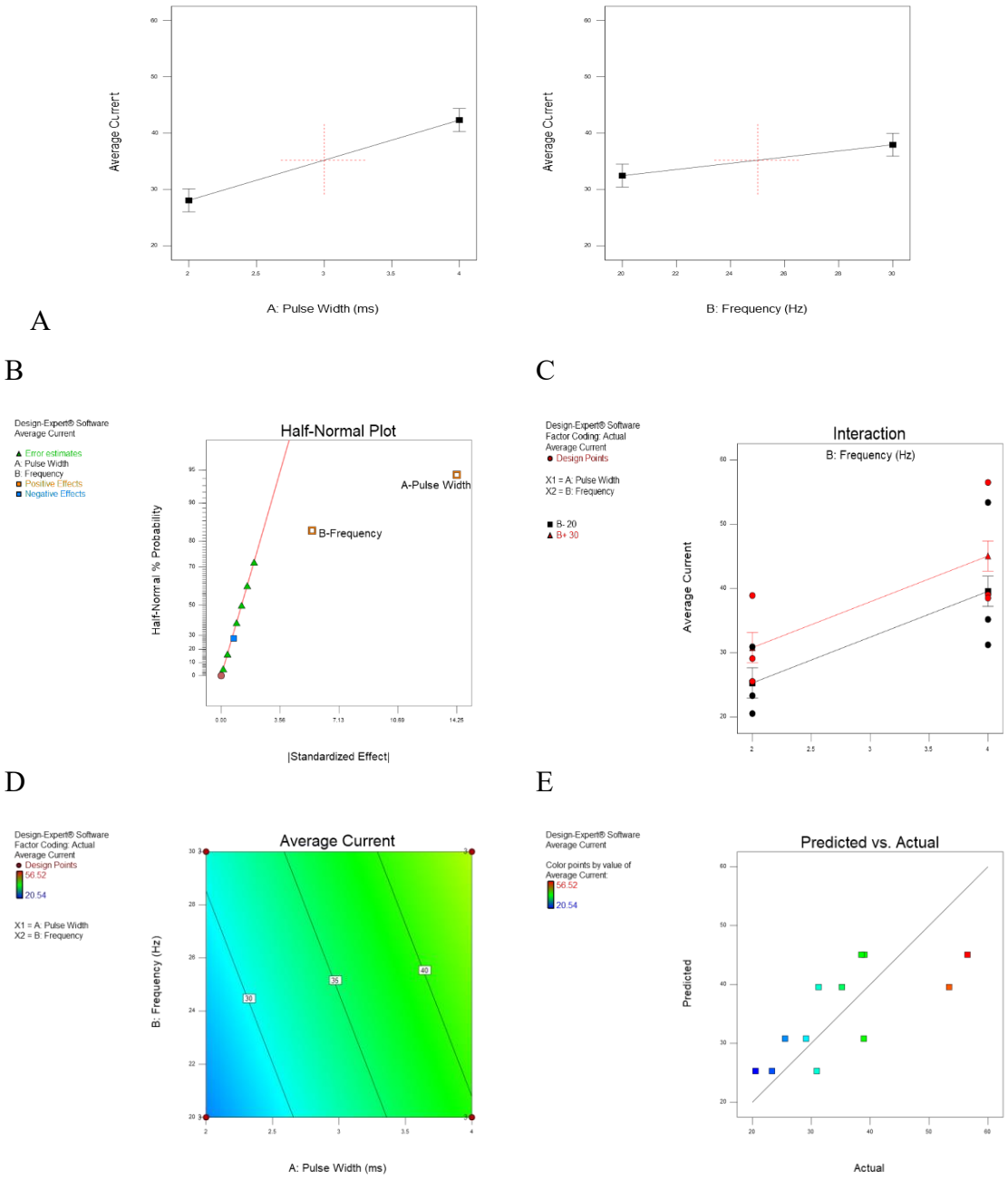


Figure 18. Average Current (A) Main Effect plots show how pulse width and frequency affect average current. Increasing pulse width significantly increases average current, whereas frequency has a smaller effect. (B) Half-Normal plot highlights the significant factors, with pulse width being the main contributor to average current, followed by frequency. (C) The interaction plot shows how pulse width affects average current across different frequencies. The nearly parallel lines suggest minimal interaction, confirming the additive effect of pulse width and frequency. (D) Response surface contour plot displays the combined influence of pulse width and frequency on average current, with both increasing the current, but pulse width being the more dominant factor. (E) Predicted versus actual plot shows a strong match between model predictions and observed values, confirming the model's validity.

4.4.2.2. Influence on Peak Current

Peak current was assessed in line with average current to evaluate the effect of pulse parameters on the peak current required to induce VF via a subcutaneous configuration. The factorial model for peak current was statistically significant ($F = 55.27$, $p < 0.001$). The model accounted for 94% of the variation in the peak current ($R^2 = 0.94$) with strong predictability (Pred $R^2 = 0.825$). Adequate precision was reported at 25.2, indicating solid model sensitivity without requiring data transformation.

The primary effects on peak current are presented in **Figure 19** A. In contrast to average current, increasing pulse width resulted in a significant reduction in peak current. Similarly, increasing frequency also lowered peak current requirements. Longer pulse widths enable sufficient depolarisation to be achieved at a lower instantaneous current level. The half-normal plot, **Figure 19** B. confirms that pulse width is the dominant factor influencing peak current, with frequency also demonstrating a strong, statistically significant effect. Notably, the separation of both factors from the noise distribution is more pronounced than in the average current model, indicating stronger overall effects. The interaction plot **Figure 19** C. demonstrates minimal divergence between response curves across the frequency range. This indicates that pulse width and frequency independently influence peak current. The absence of interactions confirms that the reduction in peak current is driven by additive physiological mechanisms rather than any higher-order coupling between waveform parameters.

The contour plot in **Figure 19** D. illustrates the combined effects of pulse width and frequency on peak current. A clear gradient is observed, with peak current decreasing as both parameters increase. The contour orientation indicates that both pulse width and frequency contribute substantially to reducing excitation thresholds. Relative to average current, the response surface plot for peak current shows a more balanced contribution from both factors.

The predicted versus actual plot, **Figure 19** E demonstrates strong agreement between model predictions and experimental observations. Data points closely follow the unity line, confirming the model's robustness and predictive accuracy. Peak current decreased with increasing pulse width and frequency, with pulse width exerting the dominant effect and is inversely related to both pulse width and frequency. Pulse width remains the dominant factor, consistent with strength-duration theory, while frequency exerts a stronger secondary effect.

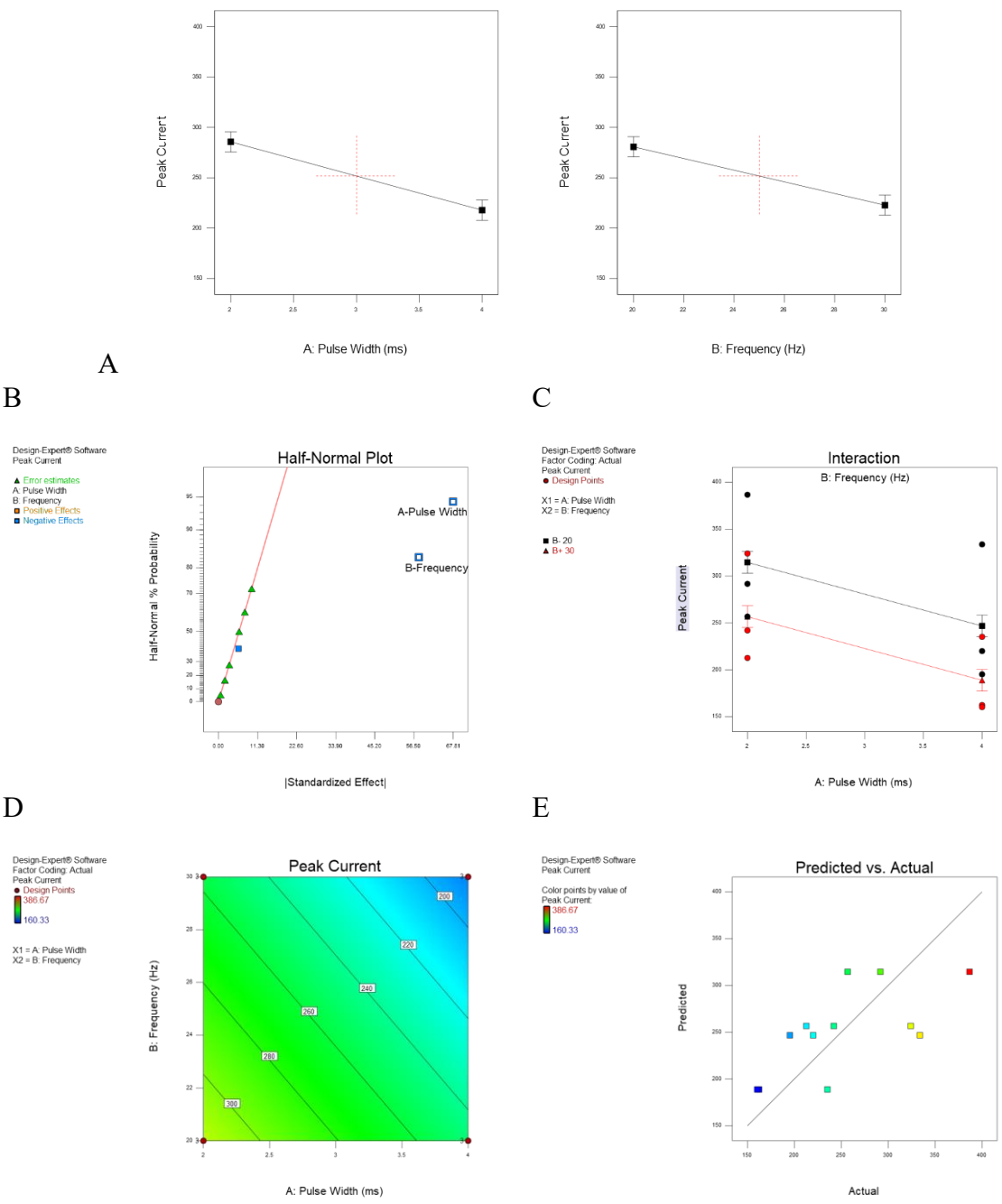


Figure 19. Peak Current (A) Main Effect plots showing the influence of pulse width and frequency on peak current. Increasing pulse width substantially reduces peak current, whereas frequency has a lesser effect. (B) Half-Normal plot identifying statistically significant factors. Pulse width is the dominant contributor to peak current, followed by frequency. (C) Interaction plot illustrating the effect of pulse width on peak current at different frequencies. The near-parallel trends indicate minimal interaction between pulse width and frequency. (D) Response surface contour plot illustrating the combined effects of pulse width and frequency on peak current. Both parameters decrease peak current, with pulse width exerting the dominant influence. (E) Predicted versus actual

plot demonstrating strong agreement between model predictions and observed values, confirming model validity.

4.4.2.3. Integrated interpretation of Average and Peak Current

A combined analysis of **Figure 18** and 16 reveal an underlying trade-off in subcutaneous stimulation behaviour. An increase in pulse width and frequency will reduce peak threshold current requirements **Figure 19**A-D., but simultaneously, the same parameters increase the average current through greater cumulative charge delivery **Figure 18**(A-D).

The difference highlights the following two opposing physiological factors:

- Efficiency of excitation (Peak Current): improved with longer pulse durations and higher frequencies.
- Energy delivered (Average Current): increased as charge accumulated over successive pulses.

The absence of interaction in both models **Figure 18**C. and **Figure 19**C. indicates that waveform parameters have independent effects on both peak and average current thresholds.

4.5. Discussion:

4.5.1. Clinical Implications of Subcutaneous VF Induction Thresholds

This pre-clinical study assessed the electrophysiological factors that determine VF induction in subcutaneous stimulation in the porcine model. Implementing a factorial DOE framework, the study quantified independent and interactive effects of pulse width and frequency on VF thresholds. The findings demonstrate that VF induction is governed not solely by pulse amplitude but on an interaction between various factors such as stimulus duration, repetition rate, and intrinsic myocardial excitability. The findings have a significant impact on waveform optimisation in S-ICDs. In light of PRAETORIAN-DFT , these findings are best interpreted within a selective-testing framework. Routine VF induction may become less common in appropriately positioned de novo S-ICD implants, but waveform optimisation remains relevant when induction is clinically indicated, when implant positioning is uncertain, during system revision, and in preclinical or next-generation device development.

The data confirm that increasing pulse width significantly reduces the peak current required for VF induction. When stimulus duration is extended from 1 ms to 8.6 ms, the VF threshold reduces by more than 50% (292.3 mA – 140.3 mA), a trend consistent with all subjects and validated by both regression modelling (Design Expert: $p < 0.001$; adj R2 ~0.92) and general

linear modelling ($p < 0.001$). This behaviour aligns with classical strength-duration theory, extending its validity to subcutaneous cardiac stimulation.

Higher stimulation frequencies had similar VF threshold-lowering effects, possibly due to increased likelihood of capturing the vulnerable window within the cardiac cycle that predisposes to fibrillation. Across all pulse widths tested, increasing the frequency from 10 to 50 Hz resulted in a significant reduction in mean peak current from approximately 217.7 mA to 151.7 mA ($p < 0.001$). There were no significant interactions between pulse width and frequency observed for peak current. This implies that both factors have additive, independent effects on peak current. This frequency-dependent reduction reflects a fundamental electrophysiological mechanism in which rapid, repetitive stimulation increases myocardial vulnerability to arrhythmia initiation.

These findings align with established principles of cardiac excitation dynamics, whereby rapid stimulation shortens cycle length and reduces diastolic interval. Experimental and computational studies have demonstrated that VF is initiated when successive wavefronts encounter incompletely recovered myocardium within the steep portion of the action potential duration restitution curve, resulting in conduction block and wave break formation.[90] This head-tail interaction between propagating wave fronts and refractory tissue represents a key mechanism underlying the transition from organised activation to fibrillation. [89]

In contrast to fibrillation, organised high-frequency stimulation has been shown to produce profound haemodynamic consequences without introducing arrhythmia. Experimental studies of alternating current stimulation demonstrated that rapid, regular activation within a narrow temporal window, with activation intervals of approximately 100-200 ms, can result in complete haemodynamic collapse despite the absence of VF. [94] These findings underscore that both the rate and temporal organisation of activation are critical determinants of cardiac response to electrical stimulation. Within this framework, the present study suggests that increasing stimulation frequency shifts myocardial activation towards a regime where small perturbations in timing or refractoriness can precipitate the transition from organised rapid activation to wave break and fibrillation.

From a physiological perspective, increasing stimulation frequency increases the probability of capturing the vulnerable window of repolarisation. Rapid stimulation reduces diastolic interval duration and shifts activation into the steep region of the action potential duration restitution curve, a condition strongly associated with electrical instability and wavefront fragmentation.[89] In the present study, the absence of a significant interaction between pulse

width and frequency indicates that frequency independently modulates this temporal vulnerability, reinforcing its role as a primary determinant of VF induction efficiency.

Despite the reduction in peak current threshold resulting from an increase in both pulse width and frequency, the total delivered current was observed to increase. The average current recorded increased by approximately fivefold the magnitude over the tested pulse width range and increased proportionally with frequency. This indicates that there is indeed a tradeoff between efficiency and power consumption. Even as low peak currents result in enhanced efficiency, high total currents introduce implications for myocardial safety, skeletal muscle activation and device battery longevity.

Large clinical studies, including the EFFORTLESS S-ICD registry and PRAETORIAN, have demonstrated the effectiveness of extravascular ICD therapies. These studies support the clinical role of S-ICD therapy as an alternative to transvenous ICD systems, particularly in appropriately selected patients where avoidance of intravascular lead-related complications is desirable while maintaining effective defibrillation therapy.[27,64,66,95]

More recently, PRAETORIAN-DFT has further refined the clinical landscape by showing that routine defibrillation testing can be selectively omitted in de novo S-ICD implants when guided by the PRAETORIAN score.[86] For now, defibrillation testing remains a Class 1 recommendation for all S-ICD implants globally.[86] The present results suggest that incorporating mechanistic insights, specifically the role of pulse width and stimulation frequency in modulating activation dynamics, may enable future optimisation of defibrillation efficacy and energy delivery. Thus, the relevance of waveform optimisation shifts from supporting universal testing towards improving the safety, reproducibility and efficiency of VF induction in selected testing scenarios.

The decrease in the confidence intervals associated with increased pulse widths implies improved reproducibility of VF induction. This has practical implications for preclinical studies, selected clinical defibrillation trials and future developments of extravascular ICD development. Consistent and predictable induction profiles are crucial factors to consider during the development process.

The findings provide insight into the potential value of transitioning from amplitude-based VF induction strategies to a more comprehensive approach that includes the use of multiple parameters in waveform optimisation. Future extravascular systems may improve the reproducibility and efficiency of VF induction testing strategies. These insights are also applicable to defibrillation, where successful termination similarly depends on effective myocardial engagement and field distribution. Therefore, improved understanding of waveform-dependent excitability may inform future S-ICD design, with the potential to

optimise energy delivery, and may contribute to improved procedural consistency and device efficiency.

4.6. Limitations

While this study provides novel insights into the electrophysiological determinants of ventricular fibrillation induction using subcutaneous stimulation, several limitations should be acknowledged.

The sample size was limited to three swine subjects, which, although sufficient to enable factorial DOE modelling of within-subject trends, may not fully capture the inter-individual variability observed in broader populations. The anatomical and electrophysiological properties of healthy swine hearts may differ from those of human patients with underlying cardiac pathology, potentially affecting the generalisability of the findings.

The study used a fixed coil-to-can vector configuration to represent current S-ICD implanted systems. While this approach ensured clinical relevance, it did not explore alternative electrode placements or orientations, which may influence field distribution and VF induction thresholds. Future studies incorporating different geometries could offer a broader understanding of vector-dependent effects. All testing was performed under acute conditions. This prevented assessment of long-term tissue remodelling, lead encapsulation, and fibrotic changes, which were not assessed and might influence system impedance and thresholds over time. The system's hardware limitations capped the maximum deliverable current at ≤400 mA, preventing full characterisation of induction thresholds for certain low-frequency, short-duration waveforms. This ceiling effect could have obscured the true rheobase in some cases and restricted the ability to develop complete strength-duration curves. Lastly, using a non-functional generator in the subcutaneous setup may have introduced differences in impedance and field distribution in impedance and field propagation compared with active, clinically implanted devices. Although the setup aimed to closely mimic clinical conditions, future validation with fully operational systems may be needed.

This study focuses on the induction of ventricular fibrillation. While VF induction and defibrillation efficacy are governed by related electrophysiological mechanisms, these findings cannot be directly extrapolated to predict clinical defibrillation success or shock efficacy.

Average current was calculated from waveform duty cycle and peak current rather than from direct measurement of delivered charge, power or energy. Therefore, average pulse train

currents should be interpreted as a current burden metric rather than a direct measure of delivered energy.

4.7. Conclusion

Subcutaneous VF induction thresholds are determined by the interplay of pulse width, frequency, and amplitude, consistent with classic strength-duration principles. This study demonstrates that waveform configuration is a modifiable factor influencing arrhythmia induction efficacy.

These findings support the development of parameter-informed VF induction strategies for situations in which defibrillation testing remains clinically or technically indicated. By combining waveform engineering with assessments of individual myocardial excitability, future induction strategies may be optimised for improved safety, consistency, and energy efficiency.

While the present work focuses on induction, the mechanistic insights into waveform-dependent myocardial excitability provide a foundation for future studies exploring optimisation of subcutaneous defibrillation strategies and device performance. In the contemporary context of PRAETORIAN score-guided selective testing, these findings are most relevant to selected clinical testing, system revision, preclinical validation, and the development of future lower-energy extravascular ICD platforms.

Chapter 5 Maturation of Human Induced Pluripotent Stem Cells

5.1. Introduction

Electrical stimulation (ES) is well-established as a fundamental aspect of cardiac rhythm management, enabling life-sustaining interventions such as pacing, resynchronisation, and defibrillation.[47,48,80,81] Chapters 3 and 4 examined the role of subcutaneous electrical waveforms in the control and restoration of myocardial excitation in vivo. In the present chapter, these same principles are examined in a different context, namely the electrical conditioning of engineered cardiac tissue. The emerging field of bioelectronic tissue engineering extends cardiac electrophysiology from device-based therapy to regenerative medicine, using electrical cues to guide the development and maturation of human induced pluripotent stem cell-derived cardiomyocytes (hiPSC-CMs).[34,43] In this setting, electrical stimulation is examined not as a means of capture or arrhythmia induction, but as a developmental cue that may influence maturation-associated transcriptional organisation in engineered human cardiac tissue, assessed here using quantitative polymerase chain reaction (qPCR) profiling of engineered human cardiac tissue.

The clinical relevance of this work lies in the continuing lack of therapies that can restore functional myocardium post-injury.[96] Cardiovascular disease (CVD) remains the leading cause of mortality worldwide, with ischaemic heart disease resulting in approximately 19.8 million deaths annually. According to the World Health Organisation, ischaemic heart disease is the leading cause of death worldwide.[97] Acute myocardial infarction (MI) is a serious complication of this disease. MI occurs when a coronary artery becomes blocked, mostly due to atherosclerotic plaque erosion or rupture, leading to ischaemia, hypoxia and cardiomyocyte death. Following MI, more than one billion cells can be lost, predominantly through necrosis. [98] The loss of cardiomyocytes following myocardial injury initiates an inflammatory and reparative fibrotic response aimed at stabilising the ventricular wall through scar formation.[99] While this fibrotic remodelling preserves structural integrity, it does so at the expense of electrical continuity and mechanical performance.[100,101] Consequently, necrotic myocardium is replaced not by new contractile cells but by non-excitable fibroblasts and extracellular matrix components that form scar.[9]

This inability to regenerate viable myocardium underpins the progressive decline in ventricular function following MI.[9,98] It explains why current clinical interventions, whether pharmacological, mechanical, or electrical, only compensate for lost function rather than

restoring it. As such, there is an unmet need for strategies that can replenish cardiomyocyte mass, re-establish electromechanical continuity, and recover native contractile behaviour within the infarcted heart.[33,102,103] Over time, the reduction in viable cardiomyocyte mass increases mechanical stress on the remaining myocardium, contributing to progressive ventricular dysfunction and heart failure. Regenerative medicine has the potential to replenish lost cardiomyocytes and support the restoration of electromechanical integration within the infarcted myocardium.[33,102,103]

Efforts to restore lost myocardial function have increasingly focused on the development of engineered tissue derived from human induced pluripotent stem cells (hiPSCs). Since their first derivation by Takahashi and Yamanaka in 2007, hiPSCs have enabled the generation of patient-specific cardiomyocytes, offering a promising cell source for myocardial repair, disease modelling and drug screening.[31,104,105] Despite the promising potential of hiPSC-CMs, these cells currently exhibit structural and functional immaturity relative to adult cardiomyocytes. This immaturity manifests as poor sarcomere organisation, altered ion channel expression, disorganised gap junctions, and underdeveloped calcium handling, all of which limit their ability to integrate with the host myocardium and to support coordinated excitation-contraction.[41,106]

To address this limitation, several biophysical conditioning strategies have been explored, including mechanical loading,[107] substrate stiffness modulation,[108] and electrical stimulation.[32,35,41] Among these, electrical stimulation has emerged as a promising cue for guiding cardiac maturation. This approach mimics aspects of the electromechanical environment of the native heart and has been associated with improved cell elongation, sarcomere alignment, gap junction polarisation and conduction velocity.[32,35,41] Electrical stimulation has also been associated with changes in structural and electrophysiological markers linked to maturation, including increased MYH7 expression and improved calcium handling. [41,109,110] More broadly, electrically conditioned maturation protocols have been associated with improved calcium handling and reduced proliferative activity in hiPSC-CMs under selected culture conditions. [44,49,106]

Despite significant advancements in the field, considerable heterogeneity remains in waveform parameters across research studies, including pulse amplitude, frequency, duration, and pulse configuration.[32,35,46] This variability has hindered cross-study comparability, making it more challenging to identify optimal stimulation protocols. Furthermore, the molecular and biophysical responses of hiPSC-CMs to different waveform configurations remain poorly understood, especially regarding their long-term effects on electrophysiological properties and structural organisation.

This study, conducted in collaboration with Centro Investigación Médica Aplicada (CIMA), implemented a Design of Experiments (DOE) framework to investigate how electrical waveform parameters are associated with maturation-associated transcriptional responses in hiPSC-CMs. The DOE examined the effects of pulse width, amplitude, frequency, and waveform type. These effects were assessed using transcriptional qPCR markers relevant to cardiomyocyte development, with particular emphasis on structural, electrophysiological, intercellular coupling, extracellular matrix, and calcium-handling domains. Accordingly, this chapter applies a focused transcriptional framework to evaluate how defined waveform configurations are associated with maturation-relevant transcript expression patterns in engineered human cardiac tissue.

5.2. Defining Maturation Metrics

The transition of hiPSC-CMs from a foetal to an adult phenotype involves a coordinated progression of morphological, molecular, and electrophysiological changes.[10,31,106] In the present chapter, maturation was assessed through transcriptional profiling of transcripts grouped into four functional categories: Muscle Contraction, Pacemaker Function, Electrical Coupling, and Calcium Handling. Each category represents a distinct axis of cardiomyocyte maturation, capturing structural and electrophysiological adaptations that occur during the transition.[31,41,106] Organising the transcript panel in this way provided a structured framework for assessing how waveform configuration was associated with maturation-relevant transcriptional organisation in engineered cardiac tissue.

The following sections outline the rationale for including key transcripts within each category and define how these domains were used to interpret waveform-associated transcriptional responses. This framework was intended to support a domain-based assessment of maturation-related transcriptional patterning rather than reliance on any single marker of cardiomyocyte development.

5.2.1. Muscle Contraction

The organisation and composition of the sarcomere, the basic unit of muscle contraction, are central to the contractile function of cardiomyocytes. In mature myocardium, sarcomeres are highly ordered, aligned along the longitudinal axis of the cell and associated with adult-like expression of key myofibrillar protein isoforms. In contrast, hiPSC-CMs typically exhibit a foetal-like contractile phenotype characterised by disorganised sarcomeres, shorter sarcomere lengths, and immature expression patterns of contractile proteins, including myosin isoforms. [10,41,106]

The switch in myosin heavy chain (MHC) isoforms is a key marker of cardiac maturation. During early development, the α-isoform (MYH6) is predominant. This isoform supports relatively rapid contraction suited to the foetal environment. After birth, expression progressively shifts towards the β-isoform (MYH7), which has slower ATPase activity but greater energetic efficiency and is better suited to sustained contraction under increased mechanical load. The transition from MYH6 to MYH7 is therefore widely accepted as a molecular indicator of cardiomyocyte maturation in engineered cardiac tissues.[41,49]

The expression of myosin light chain isoforms varies across chambers and developmental stages. MYL7 (MLC2a) is mainly found in atrial and immature ventricular cardiomyocytes. MYL2 (MLC2v) is more common in mature ventricular tissue. Accordingly, increased MYL2 expression together with reduced MYL7 expression is commonly interpreted as evidence of ventricular specification and maturation.[10,31]

In the present study, MYH6, MYH7, MYL2, and MYL7 were assessed using qPCR after 14 days of electrical stimulation with various waveforms. These transcripts were selected as markers of maturation-associated contractile remodelling within the engineered tissues. Expression levels were normalised using the 2^-ΔΔCt method to enable comparison across stimulation conditions and to support evaluation of derived isoform-expression ratios.

Electrical stimulation has been associated with improvements in contractile maturation, including more adult-like contractile protein expression, improved calcium handling and greater sarcomere organisation. Rhythmic pacing mimics aspects of the native cardiac cycle and, particularly when combined with mechanical loading, is associated with structural remodelling, improved excitation-contraction coupling, and maturation-related isoform changes.[32,41] Constructs subjected to long-term biphasic stimulation at physiological frequencies have demonstrated increased MYH7 expression, improved force-frequency relationships, and enhanced alignment of contractile units, hallmarks of mature ventricular myocardium.[41–43]

Collectively, these findings support the inclusion of contractile transcripts as one component of the present transcriptional framework for assessing maturation-related development in engineered cardiac tissue. In this study, these markers were used to examine whether waveform configuration was associated with contractile transcriptional patterns relevant to cardiomyocyte maturation.

5.2.2. Pacemaker Function

A defining feature of cardiomyocyte maturation is the transition from spontaneous, pacemaker-like activity to a quiescent, stimulus-dependent electrophysiological phenotype.

In early cardiac development and in hiPSC-CMs, spontaneous depolarisation is associated with the expression of pacemaker-associated ion channels, particularly HCN4, which mediates a hyperpolarisation-activated inward current that contributes to diastolic depolarisation. This automaticity is a hallmark of immature cardiomyocytes and reflects the retention of a pacemaker-like electrophysiological programme characteristic of sinoatrial node cells. [10,104]

In contrast, as cardiomyocytes mature, they acquire a more hyperpolarised diastolic membrane potential and more adult-like electrophysiological properties, including greater inward-rectifier potassium current activity. In PSC and hiPSC-derived cardiomyocytes, this maturation remains incomplete, with reported diastolic or resting membrane potentials remaining less negative than those of adult ventricular myocardium.[41,106] Accordingly, developmental downregulation of HCN4 together with increased IK1 function, associated with KCNJ2/Kir2.1, contributes to the suppression of spontaneous activity and the emergence of adult-like electrophysiological behaviour.[31]

Another regulator associated with pacemaker identity is the transcription factor SHOX2, which is expressed in sinoatrial node cells and has been used to drive pacemaker-like differentiation from hiPSCs. Persistent expression of SHOX2 together with HCN4 is, therefore, consistent with retention of nodal-like characteristics and a relatively immature electrophysiological phenotype. Conversely, reduced expression of these pacemaker-associated markers is consistent with progression toward a working myocardial phenotype. [10]

This study measured transcript expression of HCN4 and SHOX2 using qPCR after 14 days of electrical stimulation with different waveform configurations. These transcripts were selected as markers of pacemaker-associated phenotype and nodal-like immaturity. Their expression, therefore, provided a transcriptional basis for assessing whether waveform configuration was associated with pacemaker-associated immaturity within the engineered tissues. Expression values were normalised using the 2^-ΔΔCt method, enabling direct comparison across stimulation conditions.

Electrical stimulation has been shown to modulate pacemaker-associated transcript expression by partially recapitulating the electromechanical environment of the developing heart. Rhythmic pacing enhances calcium handling and membrane excitability and is associated with transcriptional changes in ion-channel and maturation-related genes, including reduced HCN4 expression.[32,32,41] Constructs subjected to long-term biphasic stimulation have demonstrated reduced HCN4 expression and more hyperpolarised resting

membrane potentials, consistent with a shift away from automaticity and toward a mature ventricular phenotype.[41]

Taken together, HCN4 and SHOX2 provide a useful transcriptional basis for evaluating pacemaker-associated characteristics within engineered cardiac tissue. In the context of the present study, these markers were used to assess whether waveform configuration was associated with transcriptional patterns consistent with reduced nodal-like automaticity and progression towards a working myocardial phenotype.

5.2.3. Electrical Coupling

The ability of cardiomyocytes to function as a cohesive syncytium depends on the formation of low-resistance intercellular connections that facilitate the rapid propagation of electrical impulses. This electrical coupling is mediated by gap junctions, specialised intercellular channels formed by connexin proteins, that permit the direct passage of ions and small molecules between adjacent cells.[60,111,112] In the mature myocardium, gap junctions are predominantly composed of connexin 43 (Cx43) and connexin 40 (Cx40), encoded by the GJA1 and GJA5 genes, respectively. These proteins are organised into dense plaques at the intercalated discs, specialised structures located at the longitudinal ends of cardiomyocytes, supporting anisotropic conduction and high velocity impulse propagation along the fibre axis.[10,31,113]

In contrast, hiPSC-CMs typically exhibit a foetal-like pattern of gap junction organisation. In immature cardiomyocytes, gap junctional proteins are more diffusely or circumferentially distributed rather than concentrated at the intercalated discs, resulting in slower, less directed conduction and increased arrhythmogenic potential. This immature phenotype is therefore associated with impaired electrical coupling and less coordinated propagation across the tissue. [19,111]

Electrical stimulation has been reported to promote aspects of gap-junction maturation. By mimicking elements of the native electromechanical environment, rhythmic pacing can influence connexin expression and distribution. Studies indicate that electrically stimulated tissues exhibit higher levels of GJA1 and GJA5 alongside improved organisation of gap junctions and more anisotropic electrical propagation, consistent with the emergence of a more functional cardiac syncytium.[10,41] Constructs subjected to charge-balanced biphasic stimulation exhibit enhanced electrical functionality, increased Cx43/GJA1 expression, improved connexin organisation and more synchronous contraction, findings consistent with improved gap-junction maturation and more coordinated impulse propagation.[114,115]

The structural features of these adaptations influence axial resistance, which affects the speed of signal conduction. Axial resistance is dependent on cell size, cytoplasmic resistivity, gap junction density, and interstitial conductivity.[19] As hiPSC-CMs mature, these properties change to resemble adult cells. This lowers impedance within the cells and improves impulse transmission. [19,31]

This study investigated maturation-associated transcriptional markers of electrical coupling by measuring transcript expression of GJA1 and GJA5 after 14 days of electrical stimulation using qPCR. These transcripts were selected as molecular markers of connexin-associated intercellular coupling across different waveform conditions. Data were normalised using the 2^-ΔΔCt method, enabling comparison across stimulation conditions.

Together, these findings support the inclusion of GJA1 and GJA5 as relevant transcriptional markers for evaluating electrical coupling within engineered cardiac tissue. In the present study, these markers were used to assess whether waveform configuration was associated with coupling-related transcriptional organisation relevant to maturation-associated changes in intercellular connectivity.

5.2.4. Calcium Handling

The cycling of calcium ions in cardiomyocytes is a fundamental driver of each heartbeat and represents a distinct axis of maturation in the transition from foetal-like to adult-like cardiac phenotypes.[31] In mature ventricular cardiomyocytes, excitation-contraction coupling depends on a well-organised calcium-handling system. Depolarisation triggers calcium influx through L-type calcium channels in the sarcolemma and T-tubules, which induces calcium release from the sarcoplasmic reticulum (SR) via ryanodine receptors (RYR2). This coordinated calcium-induced calcium release rapidly elevates cytosolic Ca2+, which binds to troponin C and initiates contraction. Relaxation then occurs through Ca2+ reuptake into the sarcoplasmic reticulum via SERCA2a, together with Ca2+ extrusion pathways such as the sodium-calcium exchanger. The efficiency of this process depends on the close spatial apposition of L-type calcium channels and ryanodine receptors within junctional couplons, enabling rapid and synchronised excitation-contraction coupling across the cell.[31,116]

In contrast, hiPSC-CMs and foetal cardiomyocytes exhibit an immature calcium-handling phenotype. They lack the developed T-tubule network of adult cells, resulting in spatially and temporally disorganised Ca2+ release.[30] Without a mature T-tubule system, calcium influx is initially confined to the cell periphery, resulting in a delayed and heterogeneous Ca2+ transient. Early-stage hiPSC-CMs also have smaller and functionally limited internal Ca2+ stores. During the first weeks after differentiation, SR calcium content gradually

increases. Even when the quantity of stored Ca2+ approaches that of adult cells, kinetics remain slow. Immature myocytes demonstrate prolonged time to peak and sluggish decay of Ca2+ transients. [117,118]

hiPSC-CMs typically do not exhibit the positive force-frequency relationship (FFR) that characterises mature myocardium, instead often displaying flat or negative FFR. This behaviour is thought to reflect immature sarcoplasmic reticulum calcium handling, with inadequate calcium reuptake and release at higher pacing rates.[42,43] At the early stages of development, incomplete calcium-cycling machinery can also contribute to spontaneous activity and broader electrophysiological immaturity.[31,119]

At the molecular level, the development of calcium-handling capacity is marked by significant changes in the expression of key channels, pumps, and buffering proteins. RYR2 expression is markedly lower in immature hiPSC-CMs compared with adult cardiomyocytes.[31] ATP2A2, which encodes the SERCA2a pump in cardiomyocytes, is also typically expressed at lower levels in immature cells, consistent with less efficient SR calcium reuptake.[120] Together, altered expression of calcium-handling transcripts reflects the incomplete intracellular calcium-cycling machinery characteristic of immature cardiomyocytes. [121]

Electrical stimulation has been shown to promote aspects of calcium-handling maturation in engineered cardiac tissue. Rhythmic pacing activates calcium-dependent pathways that accelerate the maturation of calcium cycling.[41] Biphasic electrical pacing at physiological frequencies has been shown to induce FFR in engineered cardiac tissue by enhancing SR calcium reserves and reuptake speed.[42] Similarly, metabolic maturation using fatty acid-rich media upregulates calcium-handling proteins and improves calcium transient kinetics.[122,123]

In this study, the expression of calcium-handling transcripts, including RYR2 and ATP2A2, was quantified using qPCR after 14 days of electrical stimulation. These transcripts were selected as molecular indicators of intracellular calcium-release and calcium-reuptake machinery. In the present study, these markers were incorporated into the transcriptional framework to assess whether defined waveform configurations were associated with calcium-handling transcriptional patterns relevant to cardiomyocyte maturation.

5.2.5. Electrical Conditioning Framework

As detailed in the preceding sections, electrical stimulation is an important biophysical cue associated with multiple aspects of hiPSC-CM maturation. Previous studies suggest that cyclic electrical conditioning can improve several indices of cardiomyocyte maturation, including cellular alignment, sarcomere organisation, intercellular coupling, conduction velocity, calcium handling and contractile performance. The stimulation regimes used across studies vary substantially in waveform type, field strength, pulse duration, frequency and overall conditioning schedule.

The present study was designed to examine how waveform configuration was associated with the maturation-associated transcriptional signatures of hiPSC-CMs. By systematically varying pulse amplitude, pulse width, frequency and waveform type, the study explored how defined electrical parameters were associated with transcriptional patterns relevant to cardiomyocyte development.

Error! Reference source not found. summarises representative studies on the electrical conditioning of cardiomyocytes across diverse experimental models, including hiPSC-CMs and neonatal rat cardiac tissue. Despite variations in waveform characteristics, amplitudes, pulse durations, and stimulation frequencies, the collective evidence indicates that appropriately applied electrical stimuli can be associated with improvements in several structural and functional features relevant to maturation. [32,35,41,42,45,109]

Table 14. Representative studies of electrical stimulation used to promote cardiomyocyte maturation. The table summarises stimulation parameters, experimental models, and reported biological outcomes across selected studies using hiPSC-derived or neonatal cardiomyocytes. Because waveform configuration, culture format, and stimulation geometry differ across studies, direct comparison of amplitudes and biological outcomes should be made with caution. Amplitude values are reported as presented in the original sources.

Study	Cell Type / Model	Waveform Type	Amplitude	PW(ms)	Freq (Hz)	Stimulation Duration
Tandon et al., 2009 [36]	Neonatal rat CMs in 3D collagen scaffold	Monophasic	5 V/cm	1-2 ms	1 Hz	7–8 days
Key Findings	Increased amplitude of synchronous contractions, enhanced cell alignment/coupling, and marked ultrastructural organisation.					
Nunes et al., 2013 [32]	hiPSC-CMs in 3D biowires	Biphasic	3-4 V/cm	1 ms	2-6 Hz (Ramped)	7 days
Key Findings	Increased myofibril ultrastructural organisation, improved conduction velocity, and enhanced Ca^{2+} handling.					
Ronaldson-Bouchard et al., 2018 [41]	hiPSC-CMs in fibrin hydrogel	Biphasic, ramped frequency protocol	4.5 V	2 ms	2–6 Hz (ramped)	28 days
Key Findings	Adult-like gene-expression profiles, physiological sarcomere length (~2.2 μm), increased mitochondrial density (~30%), anisotropic gap junction organisation, improved calcium handling, IK1 current, conduction velocity, positive force–frequency relationship, and T-tubule formation.					
Valls-Margarit et al., 2019 [109]	hiPSC-CMs on PCL scaffold with fibroblasts	Monophasic	1-5 V	2 ms	3 Hz	14 days
Key Findings	Increased sarcomere width and more developed intercellular unions					
Gabetti et al., 2023 [45]	Neonatal rat CMs and CFs	Monophasic Biphasic	5 V/cm	2 ms	1 Hz	7 days
Key Findings	enhanced electrical functionality and promoted synchronous contraction in neonatal rat cardiac cultures.					
Godier-Furnémont et al., 2015 [42]	Human ESC-derived CMs	Biphasic	5 V	3 ms	2–6 Hz	5 days
Key Findings	Increased twitch force, improved excitation-contraction coupling					

The stimulation regimes reported in these studies informed the selection of test conditions in the current work. Recognising that waveform type, pulse amplitude, pulse width, and frequency may exert independent and potentially interacting effects on maturation-associated transcriptional responses, the study implemented a structured DOE framework. This approach enabled structured exploration of the stimulus-response space across the selected parameter ranges.

The DOE comprised sixteen stimulation conditions based on high and low factor combinations, together with centre points. Amplitude ranged from 5 to 15 V, pulse width from 2 to 5 ms, and frequency from 2 to 5 Hz across both monophasic and biphasic waveforms.

Electrical stimulation was delivered using a custom-developed programmable waveform generator, as detailed in Chapter 2, to engineered hiPSC-CM constructs maintained in culture medium under controlled conditions. Within this design, waveform configuration was treated as a multidimensional experimental variable, allowing assessment of how individual electrical parameters were associated with maturation- relevant transcriptional organisation.

5.3. Research Question

The key research question investigated in this study is: How are electrical waveform parameters associated with maturation-relevant transcriptional patterns in human induced pluripotent stem cell-derived cardiomyocytes under controlled in vitro stimulation conditions?

This study used a structured DOE framework, similar to the approach in Chapter 4, to examine the impact of pulse amplitude, pulse width, frequency, and type on electrically stimulated hiPSC-CMs. Transcriptional markers spanning structural, electrophysiological, intercellular coupling, and calcium-handling domains were then assessed to determine how waveform configuration was associated with transcriptional organisation relevant to cardiomyocyte maturation.

5.4.Methods

5.4.1. Generation and Preparation of Human-Induced Pluripotent Stem Cell-Derived Cardiomyocytes

HiPSC-CMs were generated according to the protocol described by Sánchez-Bueno et al.[124], with modifications to accommodate the specific culture conditions used in this study. Cell differentiation and tissue generation were performed in collaboration with Maria Alejandra Rodriguez Pardo at CIMA Universidad de Navarra. The protocol was based on timed modulation of Wnt signalling, followed by metabolic selection, to obtain highly enriched cardiomyocyte populations suitable for tissue engineering applications.

hiPSCs were maintained under feeder-free conditions on Matrigel-coated plates in mTeSR medium and passaged every 4-5 days to preserve undifferentiated morphology and minimise spontaneous differentiation. When cultures reached 80-90% confluence, cells were harvested and replated onto fresh Matrigel-coated 12-well plates at a density selected to achieve 90% confluence within 72 hours, which was required for efficient cardiac induction.

Cardiac differentiation was initiated using a monolayer-based protocol. On day 0, Wnt signalling was activated by supplementing insulin-free RPMI medium (RPMI/B27 minus insulin) with CHIR99021 (10 µM), a GSK3 inhibitor. After 24 hours the medium was replaced with fresh RPMI/B27 minus insulin. On day 3, Wnt signalling was inhibited using C59 (5 µM) to promote cardiac lineage specification. On day 5, the medium was refreshed with RPMI/B27 minus insulin to support expansion of cardiac progenitors. From day 7 onward, cells were cultured in RPMI supplemented with B27.

Spontaneous contractile activity emerged between days 7 and 9. From day 10 onward, metabolic purification was applied to enrich the cardiomyocyte population by exploiting the ability of cardiomyocytes to utilise lactate as an energy source. Two 72-hour lactate selection cycles were performed on days 10 and 18, separated by a replating step in medium supplemented with KnockOut Serum Replacement and Y-27632 (ROCK inhibitor) to improve cell survival. This process yielded cardiomyocyte cultures with > 85% purity, as assessed by cardiac troponin T (cTnT) expression.

To prepare cells for tissue generation, hiPSC-CMs were harvested at day 21 post-induction using TrypLE enzymatic dissociation. Following dissociation, cells were counted and resuspended in a defined tissue generation medium before encapsulation within 40 µl fibrin hydrogels. The tissue generation medium comprised RPMI supplemented with B27, penicillin (1%), KSR (10%) Rock inhibitor (10 µM) and aprotinin (33 µg/mL).

Following encapsulation within fibrin hydrogels, the engineered cardiac constructs were transferred to the electrical stimulation platform for electrical conditioning. This phase of

the study employed the custom waveform generator as outlined in Chapter 2, designed to deliver controlled waveforms under sterile culture conditions. The following section outlines the experimental design, instrumentation and stimulation protocols used to evaluate how waveform configurations were associated with transcriptional patterns relevant to maturation in hiPSC-derived cardiac tissue.

5.4.2. Electrical Stimulation Test Method and Protocol

5.4.2.1. Experimental Design and Rationale

Electrical conditioning experiments were performed in accordance with a structured 16-run DOE. The aim to assess the influence of waveform configurations on maturation-relevant responses in engineered cardiac tissue. The design consisted of 12 factor conditions and 4 centre-point runs, allowing assessment of the effects of stimulation parameters across the design space while also providing sensitivity to potential non-linear responses near the centre of the tested range. Four independent factors were assessed: pulse amplitude (5-15 V), pulse width (2-5 ms), frequency (2-5 Hz), and waveform configuration (monophasic or biphasic), as summarised in Table 2.

Each condition was represented by four tissue constructs (n = 4) within a single experimental run. Unstimulated control tissues were maintained under the same culture and handling conditions as stimulated tissues, except that no electrical input was applied. The DOE provided a structured framework for evaluating waveform-dependent effects across the selected parameter space. Subsequent exclusions arising from non-viable conditions are addressed in the results section.

5.4.2.2. Electrical Stimulation Test Method for Engineered Cardiac Tissue

The tissue constructs were cultured for seven days at a time, before initiating electrical stimulation. This allowed sufficient time for tissue formation and hydrogel compaction around the support pillars. After seven days, each construct was transferred to a custom bioreactor and subjected to fourteen days of continuous electrical stimulation. The in vitro culture time was twenty-one days per sample. During the stimulation period, tissues remained in a standard cell incubator (37 °C, 5% CO2). The culture medium was changed frequently.

The tissues were stimulated by a near-uniform electric field in the bioreactor chamber as depicted in **Figure 20**A. The field was generated via two parallel high-purity graphite carbon rods (diameter = 3 mm), mounted in parallel at a fixed centre spacing of 20 mm. Each rod spanned the full length of the chamber and extended beyond the tissue area. This supported

maintaining field uniformity across the construct region, as illustrated in **Figure 20**C. This configuration was selected to provide reproducible delivery of electrical stimulation across the tissue holder.

Up to four tissue constructs were stimulated simultaneously. The constructs were mounted in a 5 mm × 7.5 mm (37.5 mm²) melt-electrowritten scaffold with a fibrin hydrogel core and secured in a custom 3D-printed stereolithography tissue holder, which positioned the samples equidistantly between the electrodes, as illustrated in **Figure 20**B and **Figure 20**D. This arrangement prevented construct drift, tilt and rotation, thereby improving uniform stimulation and spatial reproducibility.

Experimental electrical stimulation conditions were measured using a platinum reference electrode positioned adjacent to one construct with an oscilloscope. Electrical stimuli were delivered via a custom stimulation system, as detailed in Chapter 2.

Constructs were paced continuously, for fourteen days, according to the factorial DOE, as detailed in

Table 15.

Each tissue construct was paced under a unique condition and maintained at those parameters throughout the stimulation period. Control constructs, which were not electrically stimulated, were cultured in identical chambers over the same period as the stimulated tissues.

Throughout the protocol, all chambers were monitored for:

- incubator temperature and CO_2, assessed by daily incubator checks.
- waveform confirmation by oscilloscope at the start, midpoint and endpoint of stimulation.
- medium colour and pH stability through daily inspection of phenol red indicator changes.

Microscopic contractile responses during stimulation were observed in constructs using an inverted microscope. All constructs were harvested on day twenty-one for downstream transcriptional analysis.

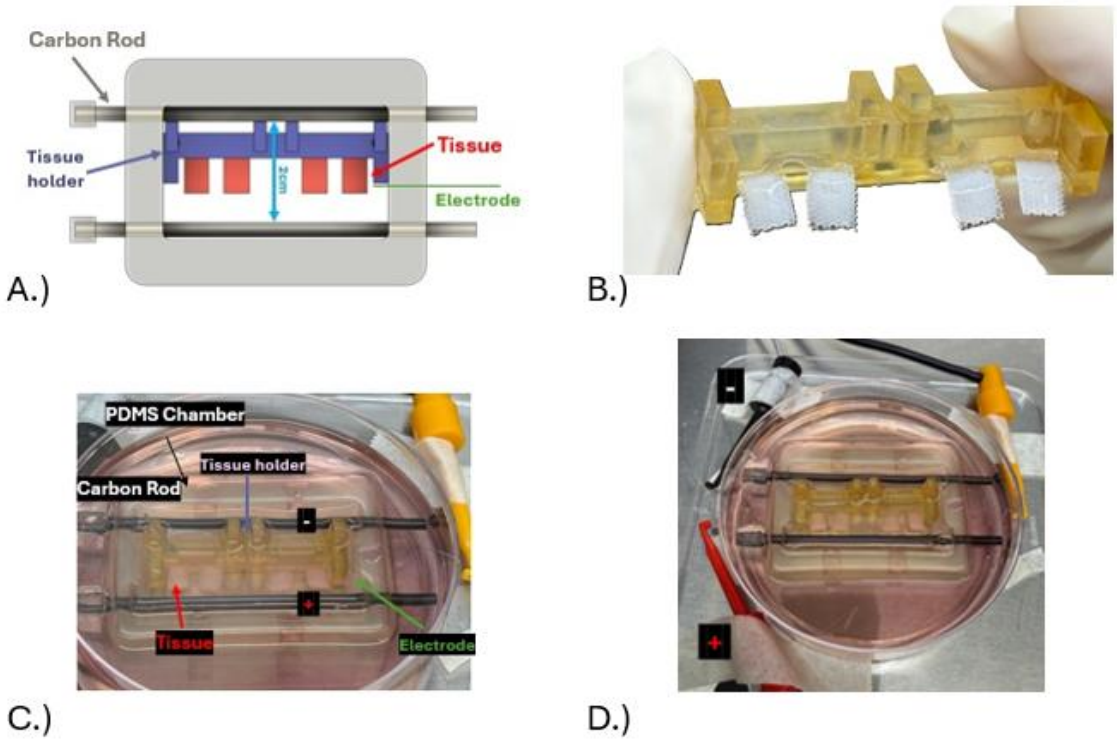


Figure 20 Custom electrical stimulation platform used for conditioning engineered hiPSC-CM tissues. (A) Schematic of the bioreactor chamber showing two parallel carbon rod electrodes positioned 20 mm apart and a tissue holder maintaining four constructs at equal spacing between the electrodes; schematic not to scale. (B) Photograph of the 3D-printed stereolithography tissue holder. (C) Representative image of the stimulation configuration with electrodes immersed in culture medium. (D) Representative photograph of the assembled stimulation platform and instrument connections.

5.5.Results

5.5.1. Experimental design and viable dataset

A 16-run design-of-experiments (DOE) was implemented to systematically investigate the effects of four waveform parameters on hiPSC-CM maturation. The four factors were pulse amplitude, constant-voltage stimulation at 5 V, 15 V, with a centre point at 10 V, pulse width, 2 ms, 5 ms; centre point 3.5 ms, stimulation frequency,2 Hz, 5 Hz; centre point 3.5 Hz, and waveform type either monophasic or biphasic pulse. Each of the 16 unique conditions was applied to a batch of four identical 3D cardiac microtissues for a continuous 14-day stimulation period. Chapter 2 details the custom waveform generator used for the delivery of these pulses. Throughout stimulation, tissue viability was monitored; three of the highest-energy conditions with high simultaneous amplitudes, long pulse widths, and high frequency exhibited poor tissue viability, resulting in medium acidification and cell death. As such, these runs were excluded from further analysis. The final dataset as detailed in

Table 15 comprised of 13 viable stimulation conditions for transcriptional analysis. **Figure 21** details the DOE parameter space, with viable runs highlighted in green and non-viable runs highlighted in red. Appendix 11, Chapter 5, Raw Data REV B, details the waveform parameters and viability outcome, including the raw transcriptional data recorded.

Table 15. Stimulus configurations used in the 16-run DOE and their analysis status. The table lists voltage, pulse width, frequency, waveform type, and whether each condition was retained or excluded from downstream analysis. Each condition was represented by four tissue constructs (n = 4) within a single experimental run; independent repeat runs were not performed.

Run	Voltage (V)	Pulse Width (ms)	Frequency (Hz)	Waveform Type	Analysis Status
1	5	2	2	Monophasic	Included
2	10	3.5	3.5	Monophasic	Included
3	15	2	5	Monophasic	Included
4	15	5	2	Monophasic	Excluded
5	5	2	5	Monophasic	Included
6	5	2	2	Biphasic	Included
7	10	3.5	3.5	Monophasic	Included
8	5	5	2	Biphasic	Included
9	15	2	2	Biphasic	Included
10	10	3.5	3.5	Biphasic	Included
11	5	5	5	Biphasic	Included
12	5	5	5	Monophasic	Included
13	10	3.5	3.5	Biphasic	Included
14	15	2	5	Biphasic	Included
15	15	5	2	Biphasic	Excluded
16	15	5	5	Monophasic	Excluded

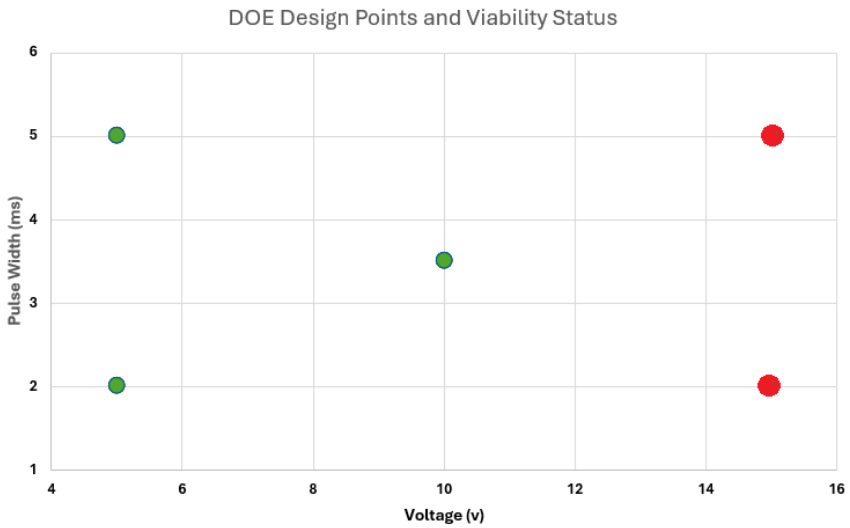


Figure 21. Distribution of DOE conditions in voltage–pulse width space with viability status indicated. Each point represents one programmed stimulation condition from the 16-run design. Viable conditions retained for downstream analysis are shown in green, and non-viable conditions excluded from analysis are shown in red. Frequency and waveform type were also varied within the DOE but are not displayed in this two-dimensional projection.

5.5.2. Raw transcriptional dataset overview

Gene expression profiling was performed on the 13 viable stimulation conditions (n=13). To provide a structured assessment of maturation-associated transcriptional responses, the qPCR panel was organised around functional domains relevant to cardiomyocyte development and phenotype. The transcriptional panel comprised 18 target genes selected to capture major maturation-relevant domains in hiPSC-derived cardiomyocytes. These included sarcomeric and contractile organisation (MYH6, MYH7, MYL2, MYL7, TNNI3, and TNNI1), electrophysiological function and calcium handling (SCN5A, HCN4, KCNJ2, CACNA1C, and RYR2), gap-junction coupling (GJA1 and GJA5), extracellular matrix remodelling (COL1A1), and developmental patterning, including SHOX2. Three biologically relevant expression ratios were derived to capture shifts in isoform predominance. These included MYH7/MYH6, reflecting the relative balance between beta and alpha myosin heavy chain expression; MYL2/MYL7, representing the ventricular-to-atrial myosin light-chain profile; and TNNI3/TNNI1, indicating the adult-to-foetal troponin I expression pattern.Gene expression for each target was quantified using qPCR, normalised to endogenous control genes and a calibrator condition, and expressed as relative expression values using the 2^-ΔΔCt method.

The raw transcriptional data showed substantial variation across the 13 stimulation conditions. Appendix 10 details the observed range of each transcript and ratio in the dataset. Many individual gene expression values varied by nearly an order of magnitude or more between different stimulation conditions.Initial inspection of the normalised qPCR dataset demonstrated condition-associated shifts across multiple maturation-relevant transcriptional endpoints. These shifts were evident both in individual gene expression values and in derived isoform ratios, with several endpoints showing broad ranges across the 13 viable waveform configurations. The expression of ventricular myosin light chain 2 (MYL2) ranged from approximately 0.42 to 3.83 relative units, normalised to control = 1, across the 13 test conditions, representing nearly a 9-fold difference. The MYH7/MYH6 mRNA ratio, representing the adult β- to foetal α-myosin heavy chain balance, varied between 0.35 and 5.15, an approximately 15-fold difference between conditions. Similarly, the TNNI3/TNNI1 ratio, representing the adult-to-foetal troponin I isoform profile, varied from 0.38 to 29.22, representing a 77-fold difference between the lowest and highest values. Genes with more moderate responses also demonstrated several-fold differences. Among them, the calcium-handling gene RYR2 shows a 2.5 fold difference across the range from 0.69 to 1.69. Broad response ranges indicated that distinct transcriptional profiles of the cardiac microtissues were associated with different waveform configurations. Subsequent analyses were therefore

performed to identify structured patterns within this multidimensional dataset. **Table 16** summarises the selected raw normalised transcript and ratio endpoint ranges across the viable data set across viable runs (n = 13).

Table 16: Selected ranges of raw normalised transcript and ratio endpoints across viable runs (n = 13)

Endpoint (raw)	Minimum	Maximum
MYL2	0.4248	3.8256
MYH6	0.4742	4.3357
MYH7	0.5941	3.0236
COL1A1	0.6402	3.1025
RYR2	0.6894	1.6887
CACNA1C	0.7988	2.9565
ATP2A2	0.5897	2.5467
MYL2/MYL7	0.2886	2.3832
MYH7/MYH6	0.3493	5.1475
TNNI3/TNNI1	0.3771	29.2153

5.5.3. Z-Score Transformation and standardised dataset

For multivariate analysis, the raw expression data were transformed into a standardised, z-score dataset. This step ensured that all transcript and ratio endpoints were on a comparable scale, each with a mean of 0 and a standard deviation of 1 across the 13 conditions. This would prevent any single gene's variance from dominating the analysis. In total, 21 variables, comprising 18 individual transcripts and 3 composite ratios, were retained for standardisation and further study. The final standardised dataset thus comprised a 13 × 21 matrix (13 conditions by 21 variables), serving as input to the unsupervised dimensionality reduction and regression analyses described below. The following z-score transformation was applied:

Equation 4: Z -score transformation

$$z_{ij} = \frac{x_{ij} - \mu_j}{\sigma_j}$$

Where x_{ij} is the raw normalised value for endpoint j in run i and μ_j and σ_j are the mean and standard deviation of endpoint j calculated across viable runs. The means and standard deviation for this standardisation are reported in Appendix 10, together with the resulting z-transformed dataset.

5.5.4. Principal component analysis of the standardised transcriptional dataset

Principal component analysis was used as an exploratory, unsupervised multivariate approach to identify major patterns of transcriptional variation across the 13 viable stimulation conditions. As an unsupervised method, PCA does not use predefined class labels or outcome groups. Instead, it summarises the dominant sources of variation within the dataset itself. This made it appropriate for examining whether the standardised gene-expression and ratio endpoints showed distinct patterns of separation. In this context, any separation observed in the PCA space could indicate underlying transcriptional response patterns associated with different waveform configurations. PCA was therefore performed on the 21-variable standardised dataset to identify the dominant modes of transcriptional variation across the stimulated conditions. dataset to identify dominant modes of transcriptional variation across the stimulated conditions. The scree plot of the PCA eigenvalues depicted in Figure 19B indicates how much variance is captured by each principal component (PC). The first principal component (PC1) had an eigenvalue of 7.52 and accounted for 35.8% of the total variance in the transcriptional data. PC2 had an eigenvalue of 4.37 and accounted for 20.8% of the variance, while PC3 captured an additional 15.4%. Combined, the top three PCs thus explained approximately 72.0% of the variance in the 18 gene and 3 ratio datasets. Subsequent components, PC4 and beyond, contributed progressively smaller portions of variance (Figure 18A). For the purposes of interpretation, analysis was focused on PC1 and PC2, as higher-order PCs each accounted for less than 10% of the variance individually.

The PCA loadings, which characterise each original variable's correlation with the PCs, were examined to characterise the biological meaning of the principal components (Figure 18B). PC1 represented a coordinated variation across multiple gene categories rather than being dominated by any single transcript. Several electrical-coupling and pacemaker-related genes recorded strong positive loadings on PC1 as evident in the loadings plot, Figure 19 C. The loadings of GJA1 0.289, GJA5 0.339, HCN4 0.319, and KCNJ2 0.283, indicating positive contributions from electrical-coupling and pacemaker-related genes. Several structural and contractile maturation markers recorded negative loadings on PC1, including TNNI3 -0.122, MYL2 -0.172, MYL2/MYL7 -0.264, and TNNI3/TNNI1-0.183. This suggests that PC1 captured an inverse relationship between the expression of certain electrophysiological/coupling genes and the expression of structural or isoform markers across the conditions. PC2 showed its strongest positive loadings for MYL2 0.393, TNNI3 0.345, MYH7 0.374, and the MYH7/MYH6 ratio 0.376, suggesting that this component was influenced primarily by sarcomeric and contractile-marker variation. In contrast to PC1,

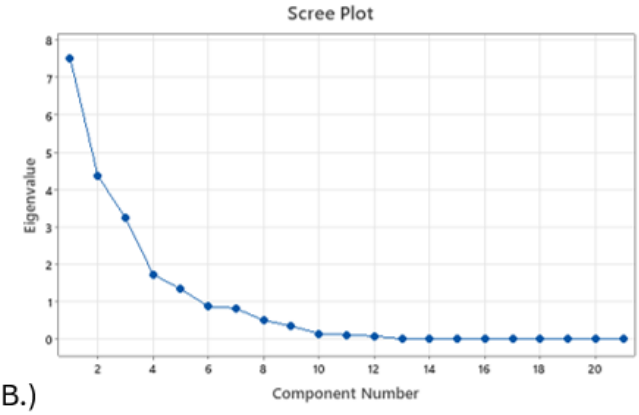
which was more strongly associated with electrical-coupling and pacemaker-related genes, PC2 appeared to capture a transcriptional axis related to myofilament composition and myosin isoform balance.

The numerical loading values are available in Appendix 9. Together, the PC1 and PC2 loadings indicate that the PCA distinguished multiple transcriptional features within the standardised dataset, rather than describing variation along a single transcriptional axis.

A.)

Variable	PC1	PC2
GJA5	0.339	-0.1
HCN4	0.319	0.066
GJA1	0.289	-0.092
KCNJ2	0.283	0.097
SHOX2	0.278	0.067
TNNI 1	0.263	0.122
SCN5A1	0.258	-0.016
ACTA2	0.248	0.136
DDR2	0.228	0.221
COL1A1	0.223	0.177
MYL7	0.195	0.232
CACNA1C	0.187	0.289
MYH6	0.095	-0.165
RYR2	0.072	0.106
MYH7	-0.025	0.374
SERCA _ATP2A2	-0.036	0.166
MYH7_MYH6	-0.078	0.376
TNNI 3	-0.122	0.345
MYL2	-0.172	0.393
TNNI3_TNNI1	-0.183	0.122
MYL2_MYL7	-0.264	0.276

B.)



C.)

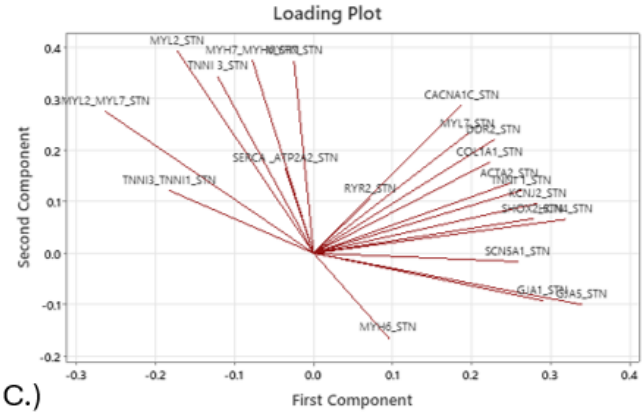


Figure 22. Principal component analysis of the standardised transcriptional dataset. (A) Colour-coded summary of loading values for principal components 1 and 2 across the 18 directly measured transcripts and 3 derived maturation-associated expression ratios included in the analysis. (B) Scree plot showing the eigenvalue spectrum across successive principal components. (C) Loading plot showing the relative orientation and contribution of variables in PC1–PC2 space. PCA was performed on the z-scored dataset using the correlation matrix; the first three principal components accounted for 72.0% of the total variance.

5.5.5. Main effects linear regression models

Building on the PCA, which identified the main transcriptional patterns PC1, PC2 and across the viable test conditions, multiple linear regression was used to test whether these patterns were associated with the waveform parameters. As each of the 13 viable stimulation conditions contributed one condition-level data point, the regression results were interpreted as exploratory. Table 17 summarises the key regression results.

The results, as detailed in Appendix 12, demonstrate that for PC1 the regression was also not significant ($p = 0.322$; $R^2 = 40.89\%$). All predictor p-values were higher than 0.10 and voltage had an approximate value of ($p = 0.10$), suggesting no individual factor clearly influenced PC1. The lack-of-fit test was near reaching, but not passing, the 5% significance threshold ($p = 0.052$), suggesting the PC1 model was not formally inadequate; however, the borderline figure might warrant caution in interpreting. The regression model was also not significant for PC2 ($p = 0.209$; $R^2 = 48.32\%$). Again, no predictor was significant at the 5% level, pulse width had the lowest value 9p ≈ 0.12). The lack-of-fit test for the model was clearly non-significant ($p = 0.909$*), indicating an acceptable fit of the main-effects model.

As with PC1, the PC2 regression model, Appendix 14, explained 48.32% of variance but did not show a statistically significant overall effect (ANOVA $p = 0.209$). All four waveform parameters remained non-significant in this model (the smallest predictor $p \sim 0.12$ for pulse width). The lack-of-fit test was non-significant ($p = 0.909$), indicating that the main-effects model provided an adequate fit for the PC2 data.

Likewise, as detailed in Appendix 13, the MYL2/MYL7 regression model explained 59.39% of the variance but did not reach overall statistical significance (ANOVA $p = 0.092$). Among the predictors, frequency was the only factor with a nominal effect ($p = 0.026$; negative coefficient), while pulse width ($p = 0.054$) and voltage ($p = 0.078$) did not reach significance and waveform type showed no effect ($p = 0.866$). The lack-of-fit test was non-significant ($p = 0.855$), indicating that the main-effects model provided an adequate fit for the MYL2/MYL7 data.

Table 17. Summary of general linear model (GLM) results for PC1, PC2, and MYL2/MYL7. Reported values include model R^2, overall regression p-values, predictor-level p-values, and lack-of-fit p-values. All p-values are shown as nominal values, as no multiple-testing correction was applied in the reported GLM outputs.

Response	Model R^2	Regression (p)	Voltage (p)	PW (p)	Frequency (p)	Type (p)	Lack-of-fit (p)
PC1	40.89%	0.322	0.103	0.12	0.112	0.274	0.052
PC2	48.32%	0.209	0.89	0.119	0.186	0.641	0.909
MYL2/ MYL7	59.39%	0.092	0.078	0.054	0.026	0.866	0.855

5.6. Discussion

5.6.1. Principal findings

This study investigated the effect of waveform configuration with maturation-relevant transcriptional organisation in electrically conditioned hiPSC-CMs using a structured DOE framework. After exclusion of three non-viable stimulation conditions, 13 viable waveform configurations were included in the final analysis dataset. Transcriptional responses were sparse at the level of individual endpoints, with no individual transcript or derived ratio showing a strong dominant pattern across stimulation conditions. All transcript-level p-values were considered nominal as no multiple testing correction was applied in the statistical outputs.

Although no strong transcript level effects were identified, principal component analysis indicated structured covariance across transcriptional endpoints. The first principal component accounted for 35.8% of the total variance. The first three principal components cumulatively accounted for 72.0% of the total variance. PC1 loadings represented coordinated contributions from multiple maturation-relevant domains, including electrophysiological and intercellular coupling transcripts (GJA1, GJA5, KCNJ2, SCN5A1, and HCN4), structural and contractile markers (MYH7, MYH6, MYL7, and derived myosin ratios), and calcium-handling transcripts (ATP2A2, RYR2, and CACNA1C).

This component was also contributed by pacemaker-related and non-myocyte markers. Taken together these loadings indicate that PC1 was reflecting a general axis of coordinated transcriptional organisation across multiple maturation-relevant domains, rather than a single pathway-driven variation. Principal component scores were analysed using general linear modelling with no statistically significant overall model effects found. Thus,

relationships between waveform parameters and principal component scores should be considered descriptive rather than statistically confirmatory. Collectively, these findings indicate that waveform configuration was linked to distributed transcriptional patterning across maturation-relevant domains in electrically conditioned hiPSC-CMs. Rather than driving either uniform transcriptional maturation or dominant regulation of individual genes, variation in the features of the waveform was associated with multivariate reorganisation of the transcriptome that resulted in mixed and partially overlapping expression patterns across structural, electrophysiological, intercellular coupling and calcium-handling axes

5.6.2. Electrical stimulation as a modulator of coordinated maturation

The role of electrical stimulation in shaping hiPSC-CM development and maturation is increasingly recognised, with accumulating evidence suggesting that electrical conditioning can partially advance immature cardiomyocyte features towards a more adult-like state. Human-induced pluripotent stem cell-derived cardiomyocytes usually display foetal-like structural, electrophysiological, metabolic, and transcriptional phenotypes, limiting their translational utility.[31] A growing body of evidence suggests that electrical conditioning can partially advance these immature features towards a more adult-like state. Previous studies have demonstrated that even short-term stimulation conditioning can promote measurable aspects of functional maturation. [43,125] Miyoshi et al. demonstrated that 48 hours of ES enhanced conduction velocity, improved sarcomeric organisation and established a positive force-frequency relationship in hiPSC-CMs.[126] These functional improvements were not necessarily accompanied by large, isolated transcriptional shifts, suggesting that electrical stimulation may act through coordinated, systems-level modulation rather than dominant single-gene induction. Masuda et al. reported that electrically stimulated cardiac microfibres showed sarcomere elongation and increased expression of electrophysiological markers, including GJA1 and KCNJ2, with the magnitude of these responses influenced by influenced by stimulation frequency.[115]

More recent work has emphasised the integrative role of electrical stimulation when combined with other maturation cues. Li et al. performed a systematic comparison of maturation drivers and identified electrical stimulation as the principal determinant of enhanced mitochondrial development, electrophysiological refinement and metabolic maturation, even when combined with lipid-enriched medium and nanopatterning.[110] Their findings reinforce the concept that ES acts as an integrative regulator of cardiomyocyte maturation across structural, electrophysiological and metabolic domains.

Most prior studies, however, have treated electrical stimulation as a binary intervention, stimulated versus non-stimulated, or varied only a single parameter, most commonly pacing frequency

.[32,41,43] Reviews of cardiac tissue engineering consistently highlight the importance of electromechanical conditioning while emphasising the need for systematic optimisation of stimulation regimes.[31,34,44] The present study extends this paradigm by implementing a structured DOE framework as a multidimensional design space rather than as a single-factor exposure. The findings therefore support interpretation of electrical stimulation not simply as the presence or absence of pacing but as a configurable conditioning variable associated with coordinated transcriptional organisation across maturation-relevant domains.

5.6.3. Distributed Transcriptional organisation versus dominant gene regulation

A central observation of this study is that waveform configuration was associated with structured multivariate transcriptional organisation despite the absence of strong isolated transcript-level effects. Rather than indicating a lack of biological structure, this pattern is consistent with the distributed and multiscale nature of cardiomyocyte maturation described in the literature.[31]

Karbassi et al. emphasised that the maturation of hiPSC-CMs is not governed by singular transcriptional switches but rather involves coordinated remodelling across sarcomeric structure, ion channel expression, excitation-contraction coupling, metabolic substrate utilisation, and intercellular junction formation.[31] Within this framework, maturation stimuli are expected to reorganise transcriptional covariance across functional domains rather than produce dominant regulation of individual transcripts.

The present data align with this view. While individual endpoint analysis identified only modest, nominal effects, principal component analysis revealed waveform-associated organisation spanning electrophysiological, structural pacemaker-associated, and calcium-handling endpoints. Importantly, these effects were mixed rather than uniformly maturational, with pacemaker-associated and non-myocyte-related markers contributing alongside maturation-associated transcripts. This pattern suggests partial and heterogeneous adaptation rather than wholesale progression toward an adult-like transcriptional state.

From this perspective, the absence of dominant transcript-level significance should not be interpreted as biological inactivity. Instead, the data indicate that waveform configuration was associated with the relative weighting and coordination of transcriptional domains, consistent with a systems-level response to electrical conditioning.

5.6.4. Electrophysiological and Gap Junction Regulation

Electrophysiological maturation is a central determinant of cardiomyocyte functional development, encompassing sodium channel expression, inward rectifier current development, gap junction formation and coordinated impulse propagation.[10,31,106] In the present study, electrophysiological and coupling transcripts, including GJA1 (connexin-43), GJA5 (connexin-40), SCN5A1, KCNJ2 and HCN4, demonstrated structured covariance within principal component space.

Although no individual electrophysiological transcript reached statistical significance response at the nominal level, their coordinated contribution to PC1 suggests that this component was associated with electrophysiological organisation at the systems level. Notably, pacemaker-associated markers such as HCN4 and SHOX2 contributed alongside ventricular electrophysiological markers, indicating that electrophysiological maturation remained biologically mixed under the experimental conditions examined.

This pattern is consistent with prior studies in which electrical conditioning improved electrophysiological function through coordinated structural and network-level changes rather than isolated ion channel upregulation. Nunes et al. demonstrated that progressive electrical conditioning enhanced conduction velocity and calcium transient propagation in engineered tissues, with improvements associated with alignment and coupling rather than dominant single-gene effects.[32] Similarly, Masuda et al, reported improved synchronised contraction and sarcomeric organisation alongside moderate transcriptional changes.[115]

Compared with more complex three-dimensional electromechanical systems, the present simplified engineered tissue model exhibited lower-amplitude transcriptional responses while retaining evidence of organised electrophysiological covariance. The absence of dominant transcript-level effects is therefore consistent with recognised limitations of simplified systems lacking aligned architecture, mechanical loading, and long-term conditioning. Together, these findings support a cautious interpretation in which waveform configuration modulated electrophysiological organisation rather than directly specifying a uniformly mature electrophysiological phenotype.

5.6.5. Simplified Engineered Tissue Context and Limits of Maturation

The present study used cells expanded and differentiated in a two-dimensional culture system before dissociation and incorporation into three-dimensional engineered tissues. Cardiomyocyte maturation is widely recognised to depend on integrated electromechanical and structural cues, including extracellular matrix alignment, mechanical stretch, and long-term conditioning.[44,127]Engineered tissues, such as the Biowire platform and engineered

human myocardium, have demonstrated more advanced structural and electrophysiological maturation under combined electromechanical stimulation within aligned three-dimensional constructs.[32,110] These systems incorporate architectural and conditioning cues that were not fully reproduced in the present model.

Within this context, the transcriptional responses observed here are best interpreted as partial maturation-associated adaptation rather than full adult-like maturation. Principal component analysis indicated that waveform configuration was associated with structured transcriptional organisation despite the absence of mechanical conditioning and complex tissue architecture. The findings, therefore, underscore the importance of interpreting waveform-associated effects within the biological and structural constraints of the experimental model, rather than as evidence of complete cardiomyocyte maturation.

5.6.6. Implications for waveform optimisation and bioelectrical design constraints

By treating electrical stimulation as a configurable design variable rather than a binary exposure, the present research establishes a structure for interpreting how waveform parameters were associated with maturation-associated transcriptional organisation. The results suggest that was associated with cardiomyocyte phenotype through distributed, multivariate mechanisms rather than through dominant regulation of individual transcripts.

From a translational perspective, this implies that optimisation strategies that rely solely on maximising single-gene expression changes may be misleading. Instead, multivariate endpoints, such as principal component organisation, domain-level covariance and derived ratio coordination, may offer more biologically meaningful targets for optimisation. Importantly, the observed transcriptional responses were mixed and partially overlapping across domains, indicating that optimisation will likely require balancing structural, electrophysiological, pacemaker-associated and calcium-handling outcomes rather than maximising a single composite signal.

The exclusion of three high-energy stimulation conditions due to observed phenol red colour change, indicating pH instability, further highlights the presence of bioelectrical constraints within the tested parameter space. These observations demonstrate that waveform optimisation must operate within electrochemical tolerance limits to maintain tissue viability. Accordingly, waveform optimisation should be viewed as a constrained biological design problem in which maturation-associated responses must be balanced against electrochemical stability and cytotoxic risk.

5.7.Limitations

Several limitations should be considered when interpreting the findings of this study. First, although three-dimensional engineered tissues were used, the model lacked several key features of the in vivo environment, including vascular structures, supporting non-myocyte cell populations such as fibroblasts, and the full layered architectural complexity of the heart. These factors are known to influence maturation and likely limited the magnitude of transcriptional responses observed.

Second, due to practical constraints, each stimulation condition was represented by a single experimental run with four tissue constructs per condition and no independent repeat runs were performed. In addition, the exclusion of non-viable conditions reduced the estimable design space, limiting regression modelling to main effects. While these constraints reduced statistical power, the factorial framework still enabled identification of waveform-associated multivariate structure.

Third, transcriptional analysis was limited to targeted qPCR measurements of eighteen directly measured transcripts and three derived maturation-associated expression ratios. While these markers capture key maturation-relevant domains, they cannot represent the full transcriptional, metabolic or proteomic landscape. Finally, functional electrophysiological measurements were not directly assessed, limiting the ability to link transcriptional organisation to functional outcomes.

Despite these limitations, the study provides a structured framework for examining waveform-associated transcriptional organisation in electrically conditioned hiPSC-derived cardiomyocytes and for informing future studies incorporating broader molecular and functional endpoints.

5.8.Conclusion

This study systematically examined the association of electrical stimulation waveform configuration with the maturation-associated transcriptional profile of hiPSC-CMs using a structured DOE framework. By simultaneously varying pulse amplitude, pulse width, frequency, and waveform type, the study extends the current paradigm of electrical conditioning beyond simple stimulated versus non-stimulated comparisons.

At the level of individual endpoints, only modest and isolated transcriptional effects were observed, with no individual transcript or derived ratio demonstrating a robust dominant response across stimulation conditions. In addition, no multiple-testing correction was reported in the associated statistical outputs.

However, multivariate analysis suggested that waveform configuration was associated with coordinated transcriptional variance across maturation-relevant domains, including electrophysiological, coupling, structural, and calcium-handling domains, and calcium handling pathways. Principal component modelling indicated that waveform configuration was associated with structured organisation of global transcriptional variance, with PC1 accounting for 35.8 % of the total variance in the dataset.

These findings support a systems-level view of cardiomyocyte maturation in which electrical stimulation was associated less with dominant regulation of individual genes than with coordinated organisation of transcriptional programmes across structural, electrophysiological, coupling and calcium handling domains. Within this framework, waveform configuration is best understood as a tunable modulator of coordinated transcriptional organisation rather than as a trigger of uniform maturation across all domains. The study therefore supports a parameterised framework for waveform optimisation in the bioelectrical conditioning of engineered cardiac tissue. By showing that maturation-associated responses were more effectively captured through coordinated multivariate organisation than through isolated endpoint-level effects, this work provides a structured basis for future optimisation of electrical conditioning protocols in cardiac tissue engineering.

Together, these results contribute to the emerging view that cardiomyocyte maturation is a distributed multiscale process governed by coordinated biological networks. Future integration of waveform optimisation with mechanical conditioning and more representative three-dimensional tissue architecture, including vascular structures and supporting non-myocyte cell populations such as fibroblasts, may further enhance the development of physiologically mature engineered myocardium for disease modelling, drug screening, and regenerative therapies.

Chapter 6 General Discussion and Conclusion

6.1.Overview and Integrative Perspective

This thesis draws together evidence from organ-scale and cellular-scale experiments to demonstrate that electrical waveform configuration is a pivotal design parameter shaping cardiac function and adaptation across multiple biological levels. By uniting preclinical in vivo studies of cardiac excitation and arrhythmia with in vitro analysis of gene expression in engineered cardiac tissues, the work reveals how modifying waveform attributes, including pulse shape, duration, frequency, can significantly influence both acute electrophysiological outcomes and long-term cardiomyocyte development, with important implications for future device optimisation and bioelectrical therapy. In this context, "waveform configuration" refers to the temporal structure of the electrical stimulation, pulse shape, phase balance, amplitude, pulse width, and repetition frequency. As outlined in Chapter 1, while electrical stimulation is fundamental to both cardiac device therapy and cardiac tissue engineering, the selection of waveform parameters in clinical settings has largely been empirical, lacking a systematic, multi-scale characterisation of their effects. To address this gap, the research included both in vivo and in vitro studies within a unified experimental framework.

The design of a stimulation system to facilitate research across organ-level and cellular models is inherently constrained by the requirements of the experimental models. The in vivo characterisation testing requires high-current delivery, electrical isolation, and robustness to complex tissue-electrode interactions. The in vitro system required low voltage, long duration and stable operation in controlled environments.

A custom waveform generator (CWG) developed in Chapter 2 provided precise and reproducible control over pulse duration, amplitude, and frequency. It was used in high-current preclinical studies on swine models and low-voltage cellular-level conditioning experiments with hiPSC-CMs. This cross-scale stimulation approach reduced hardware-related variability and enabled waveform parameters to be evaluated across both experimental settings within a common technical framework. Chapters 3 and 4 employed the CWG within a porcine S-ICD model, studying how waveform parameters influence myocardial excitation thresholds and ventricular fibrillation induction. This highlights their importance in improving cardiac therapy and device safety. Chapter 5 extended the research by examining how waveform modulation was associated with maturation-relevant transcriptional responses in hiPSC-CMs under chronic pacing in vitro. Together, these studies offer a cross-scale perspective on how waveform architecture interacts with cardiac

electrophysiology, with implications for both device development and electrical conditioning strategies in tissue engineering. The following discussion integrates the results from each experimental objective and considers their wider implications for cardiac devices and tissue engineering.

6.1.1. Objective 1: Development of a Programmable Waveform Platform

Objective 1 focused on the development of a programmable waveform generator capable of delivering electrical stimulation across a wide range of current and voltage levels. These capabilities were necessary for subcutaneous pacing and ventricular fibrillation induction experiments. The main motivation for Objective 1 arose from the limitation of laboratory stimulation systems that share a common electrical ground with other clinical equipment. These setups can unintentionally create earth-return paths, causing noise, instability, or measurement artefacts during stimulation testing. To prevent this, the waveform generator was powered by an independent battery supply with galvanically isolated circuitry. This design effectively removed interference pathways and supported stable, artefact-free delivery of stimulation pulses during electrophysiological assessments.

The system was designed to reproduce stimulation vectors relevant to subcutaneous configurations. This was achieved by applying current between two active electrodes arranged in a coil-to-can configuration. The system could be programmed to support both monophasic and biphasic waveforms, with output currents ranging from 0 to 400 mA. It delivered stimulation to loads with impedances from 12.5 to 200 Ω, typical of thoracic impedances encountered during extravascular stimulation. Pulse widths were adjustable from 500 µs to 10 ms, with configurable inter-pulse intervals.

Validation testing confirmed that the system consistently produced reproducible waveforms, with pulse-width deviations of less than 1% and current-output variability of less than 4% across a variety of impedance conditions. All evaluations were performed under physiologically relevant load scenarios. The platform was used to support both in vivo electrophysiological characterisation and in vitro cardiomyocyte conditioning. Incorporating an electrically isolated system across experimental setups minimised variability related to instrumentation and facilitated direct comparison of stimulation waveforms with biological responses. Using a single platform across both high-power in vivo models and low-power cell culture experiments also reduced methodological inconsistency and strengthened cross-scale comparison.

Overall, the development of this stimulation platform laid a technical foundation for the research described herein. By creating a common system capable of generating accurate and

reproducible waveforms in both organ-level and cellular models. It enabled the experimental continuity necessary to elucidate how electrical waveform characteristics influence cardiac excitability, arrhythmogenesis, and maturation-associated transcriptional responses in cardiomyocyte maturation.

6.1.2. Objective 2: Subcutaneous Pacing Threshold Characteristics

With a stable and programmable stimulation platform established, the next step was to characterise the fundamental excitability limits of cardiac tissue under subcutaneous stimulation. The purpose of this stage of the investigation was to determine whether the classical electrophysiological relationships that govern myocardial excitation during transvenous pacing remain valid when stimulation is delivered from an extravascular location. In particular, the study sought to quantify the strength-duration characteristics of subcutaneous pacing and derive the associated rheobase and chronaxie parameters that describe myocardial excitability.

Pacing thresholds were evaluated in a porcine model designed to replicate the clinically relevant coil-to-can stimulation vector characteristic of a subcutaneous implantation. Threshold measurements were systematically performed across a range of waveform configurations. These data supported the development of strength-duration curves for each subject. Myocardial capture consistently followed the classical hyperbolic relationship between stimulus amplitude and pulse duration, as initially described by Weiss and Lapicque. As expected, capture under subcutaneous conditions required substantially higher current amplitudes than those typically reported for endocardial pacing. Model-fitting provided estimates of rheobase and chronaxie for each subject, confirming that the fundamental mechanisms of membrane depolarisation remain active despite the spatial separation between the electrode and the myocardial tissue. Although the overall shape of the strength-duration curves was consistent across experiments, the actual capture thresholds showed notable variability compared to those observed in standard endocardial pacing systems. Rheobase values ranged from 19 to 78 mA, while chronaxies varied from 0.7 to 3.1 ms. These thresholds are higher than those reported for transvenous leads, reflecting the increased energy required for remote-field stimulation through thoracic tissues.

An additional pattern emerged when the subject-specific strength duration parameters were compared. Animals exhibiting higher rheobase currents showed shorter chronaxies. This relationship likely reflects geometric and biophysical factors such as electrode-myocardium distance, transthoracic impedance and the distribution of current density. While these parameters were not directly measured in the present study, the observed behaviour is

consistent with established principles describing how electrode spacing and tissue conductivity influence excitation thresholds.

The investigation explored the impact of waveform type on capture thresholds by comparing monophasic and biphasic stimulation in a subset of animal subjects. Contrary to findings reported in previous studies related to neural stimulation and endocardial pacing, no statistically significant difference in capture threshold was observed in this study. While trends were that were directionally consistent with previous reports, the study's data did not achieve statistical significance. Typically, threshold currents for both pulse types were comparable across a range of tested pulse durations.

The overall findings suggest that classical strength-duration theory remains applicable to subcutaneous cardiac stimulation. Nonetheless, the energetic demands of achieving myocardial capture are markedly higher than those observed with intravascular pacing. These results establish quantitative benchmarks defining the electrical conditions required for myocardial excitation from an extravascular source. Characterising these excitation parameters was a crucial step before conducting further investigations. Elucidation of the relationship between current, pulse duration and myocardial capture provided the physiological framework necessary to evaluate how waveform parameters influence arrhythmogenesis. In this respect, Objective 2 was achieved: the study demonstrated that classical excitability models remain informative under subcutaneous conditions, while also showing that extravascular stimulation imposes substantially greater energetic demands and greater intersubject variability than conventional endocardial pacing.

Building on this foundation, Objective 3 broadens the scope from myocardial excitation to encompass the induction of ventricular fibrillation, emphasising how stimulus configurations and cardiac excitability interact to affect arrhythmogenic risk.

6.1.3. Objective 3: Waveform Modulation of Ventricular Fibrillation Induction

The strength-duration properties governing subcutaneous myocardial capture were developed in Chapter 3 for the porcine model. Objective 3 then examined how these excitability principles relate to the initiation of ventricular fibrillation. The pacing characterisations confirmed that classical electrophysiological relationships are maintained under extravascular stimulation, while also demonstrating that substantially higher current levels are necessary compared to endocardial pacing systems. These observations prompted an investigation into how waveform parameters that influence myocardial excitability also modulate the electrical conditions required to induce ventricular fibrillation. The third objective explored how waveform configurations interact to set thresholds for VF induction.

Special attention was given to clarifying the relationship between peak current, which determines instantaneous myocardial excitation, and average current, which affects the overall electrical load on device power systems. Although previous research on VF induction has primarily focused on peak current or voltage thresholds, this study aimed to determine whether VF could be reliably triggered by waveform configurations that minimise the sustained average current, even if these configurations involve moderately elevated peak currents.

Subcutaneous implantable cardioverter-defibrillator (S-ICD) systems operate across a broad voltage spectrum. Post-shock pacing and induction systems operate at low voltage, typically 80-100 V. In contrast, defibrillation shocks utilise high-voltage systems at 1350 V. A key determinant of the size of implantable devices is the battery. The current A209/A219 Emblem platform utilises a 9 V battery comprising three 3 V lithium manganese dioxide batteries. Reducing the battery voltage can significantly reduce the system's size and overall footprint.

Lowering the primary-side voltage by a third will introduce additional design constraints, particularly with the flyback power supply that delivers the high-voltage output. Efficient performance depends on the implanted device operating at both low voltages, around 80 V, for post-shock pacing and induction protocols, and high voltages, near 1400 V, for defibrillation therapy. This operational range requires precise selection of the transformer turns ratio and effective management of duty-cycle parameters. Very high duty cycles at elevated voltages can increase core losses and reflected energy in the transformer. This can reduce the power transferred to the load, with potentially important consequences for device performance. Conversely, very short duty cycles at lower voltages may prevent the flyback converter from extracting sufficient input power. Therefore, an optimal balance is required between immediate current delivery and the ability to sustain the electrical load.

The current EMBLEM S-ICD platform demonstrates these limitations in practice: VF is induced using a fixed stimulation protocol consisting of an alternating-polarity biphasic pulse train with a pulse width of 8.6 ms, delivered at 200 mA and repeated at 50 Hz. Due to the long pulse duration and high duty cycle, this waveform produces a substantial average current of 172 mA. While this stimulus profile is consistent in inducing VF, it requires substantial power from the device's power supply and associated circuitry.

This study systematically examined the impact of waveform parameter variations on VF induction thresholds. Using a structured design of experiments (DOE) methodology, the study evaluated the effects of pulse width and stimulation frequency within physiologically relevant ranges. The results demonstrate that both parameters significantly influence the

peak current required for VF induction. Increases in pulse width and frequency consistently reduced this current across all subjects. Extending pulse widths from 1 ms to 8.6 ms resulted in approximately a 50% decrease in the average peak current needed for successful VF induction. These findings reinforce established electrophysiological principles, whereby longer stimulus durations enhance membrane charging, thus increasing the likelihood of myocardial depolarisation sufficient to induce arrhythmogenesis. Similarly, higher stimulation frequencies appear to lower thresholds, probably by increasing the chances of stimuli occurring during the myocardium's vulnerable period.

This study revealed an interesting trade-off in cardiac stimulation between peak and average current delivery. Longer pulse widths and higher frequencies resulted in lower peak currents required to induce ventricular fibrillation. This is consistent with classic principles of membrane charging. These same conditions increase the average current over the pulse train. Conversely, shorter pulse durations with lower repetition rates demand much higher peak currents but result in significantly lower average current exposure. This presents an interesting engineering and physiological challenge: optimising extravascular stimulation systems involves balancing immediate electrical excitation with overall energy use. From an engineering perspective, this trade-off has significant implications: the average current directly affects total energy consumption, thereby impacting battery life and thermal loads on pulse-generation electronics. Strategies that reduce average pulse-train current may help address constraints related to battery chemistry, power-converter design and thermal loading, particularly in future lower-energy or miniaturised extravascular ICD platforms..

Alternatively, approaches that permit elevated peak currents while decreasing sustained current might lower the voltage required for subcutaneous implantable cardioverter-defibrillators (S-ICDs). This could enable a platform redesign by moving from the current 9 V design to lower-voltage systems. This, in turn, provides a viable pathway to device miniaturisation. However, a key physiological limitation exists: waveform configurations with lower average currents can still effectively induce VF, but the higher peak currents they require increase skeletal muscle activation. This is a consequence of subcutaneous stimulation interacting with surrounding thoracic muscles; these increased instantaneous currents cause visible muscle contractions. Although manageable in anaesthetised experimental settings, such effects are unlikely to be tolerated by conscious patients. These findings demonstrate electrophysiological and engineering feasibility; waveform strategies that require drastically increased peak currents are unlikely to be clinically acceptable because of patient comfort and tolerability constraints. This, therefore, establishes a pivotal boundary condition for the development of extravascular defibrillation systems. Although

waveform optimisation can significantly improve the energy efficiency of VF induction, physiological tolerability ultimately limits the permissible peak current amplitudes. Future device innovations must therefore carefully balance electrical efficiency with patient comfort and procedural reliability when designing induction and defibrillation protocols.

Furthermore, these findings are relevant to ongoing debates about the clinical necessity of ventricular fibrillation (VF) induction during device implantation procedures. Randomised trials such as SIMPLE and NORDIC have shown that routine defibrillation threshold testing can be safely omitted in many transvenous implantable cardioverter-defibrillator (ICD) systems. Recent PRAETORIAN-DFT results have changed the clinical framing of VF induction in S-ICD implantation. Rather than supporting universal routine defibrillation testing, the evidence now supports a selective strategy in which PRAETORIAN score assessment can guide omission of testing in appropriately positioned de novo S-ICD implants. This does not diminish the relevance of the present work. Instead, it narrows its clinical application to scenarios in which VF induction remains indicated or valuable, including uncertain implant positioning, elevated PRAETORIAN scores, system revision, generator replacement, preclinical validation and next-generation extravascular ICD development. Within this more selective framework, understanding how waveform configuration influences induction threshold, reproductivity and current burden remains important for improving procedural safety and device efficiency. While these trials mainly focus on anatomical factors affecting defibrillation success, this work emphasises the importance of electrophysiological factors as additional contributors. Specifically, the data suggest that waveform configuration influences not only the energy efficiency of VF induction but also its reproducibility in subcutaneous systems. Developing a mechanistic understanding of these relationships could improve induction protocols and enhance waveform design for next-generation extravascular defibrillation technologies.

The findings presented in Chapter 4 show that waveform design directly influences arrhythmia-induction thresholds and energy requirements. Building on the strength-duration principles established in Objective 2, these results highlight a key principle of this thesis: that electrical waveform configuration is a vital design factor in the development of future bioelectronic cardiac therapies. Taken together, objective 3 was achieved by demonstrating that VF induction under subcutaneous conditions is not governed solely by absolute current amplitude, but by a broader interaction between pulse width, frequency, peak current and average current, with direct implications for device efficiency, miniaturisation and procedural design.

6.1.4. Objective 4: Waveform-Dependent Maturation of hiPSC-Derived Cardiomyocytes.

The initial objectives concentrated on how electrical waveform parameters influence myocardial excitation and the induction of arrhythmia in vivo. Objective 4 investigated whether similar principles are associated with the maturation of engineered human myocardium in vitro. Specifically, the study evaluated how systematic variation in electrical waveform configuration was associated with maturation-associated transcriptional organisation in human induced pluripotent stem cell-derived cardiomyocytes (hiPSC-CMs). As detailed in Chapter 1, hiPSC-CMs typically exhibit immature phenotypes similar to those of foetal cardiomyocytes. These are characterised by disorganised sarcomeres, altered expression of ion channels, immature calcium handling, and limited electrophysiological coupling. These features hinder their usefulness in disease modelling, drug screening and regenerative applications. Although electrical stimulation is a common strategy for promoting maturation, most studies treat it as an empirical intervention. Previous studies have examined the effects of electrical stimuli by changing a single parameter, usually pacing frequency. Therefore, the complex influence of waveform parameters on cardiomyocyte development remains insufficiently explored.

To address this knowledge gap, Chapter 5 adopted a structured DOE framework, similar to that used in Chapter 4 to study how waveform parameters influence maturation-associated transcriptional responses in engineered cardiac tissue. Using the CWG from Chapter 2, hiPSC-derived cardiac constructs were subjected to controlled electrical stimulation for 14 days. The factorial design enabled simultaneous assessment of individual parameters and their higher-order interactions thereby enabling the study to investigate which electrical factors affect cardiomyocyte maturation systematically. Transcriptional analysis showed clear patterns: electrical stimulation caused modest changes in gene expression at the level of individual genes. Certain transcripts, such as MYL7 and MYH7, did show nominal associations but did not withstand correction for multiple comparisons. The multivariate analysis suggested that waveform configuration was associated with structured patterns of transcriptional covariance, although the principal-component regression models did not reach conventional statistical significance. Principal component analysis indicated that stimulation parameters, particularly voltage amplitude, stimulation frequency, and waveform type, contributed to organising coordinated transcriptional responses across various functional domains.

These responses involved not only isolated gene expression changes but also the coordinated regulation of multiple networks related to cardiomyocyte maturation. Transcripts associated

with electrical coupling and membrane excitability, such as GJA1, GJA5, KCNJ2, and SCN5A, played a major role in the main axes of variation. At the same time, structural and contractile gene expression, exemplified by MYH6, MYH7, and MYL2, outlined a distinct yet connected transcriptional axis related to sarcomeric development. Additionally, calcium-handling genes like RYR2 and ATP2A2 contributed to differences in transcriptional patterning related to calcium handling capacity. These patterns suggest that stimulus configuration was associated with how transcriptional programmes are organised during cardiomyocyte maturation, rather than simply increasing the expression of individual genetic markers. This supports the growing view that cardiomyocyte maturation is a distributed, systems-level process involving the coordinated remodelling of structural, electrophysiological, metabolic, and calcium-handling pathways. In this context, electrical stimulation may act more as a regulatory input that shapes the development of these interconnected biological networks than as a simple binary trigger for intervention. The findings suggest that waveform configuration may represent a tunable developmental signal associated with the reorganisation of transcriptional covariance across key maturation domains.

The data also offer a key methodological insight. Traditional single-gene fold-change analyses might underestimate the biological impact of electrical conditioning. In contrast, multivariate methods like principal component analysis are more informative because they reveal coordinated, domain-level responses that could otherwise go unnoticed. This highlights the importance of systems-level analytical frameworks in understanding complex maturation processes. Additionally, the experimental design showed that high-energy waveform conditions can influence the electrochemical stability of the culture medium. This was indicated by phenol-red decolourisation and decreased cell viability, highlighting the need for electrical conditioning protocols to remain within a safe electrochemical range. Excessive stimulation energy can disrupt the physicochemical environment of the culture, reducing the viability of certain waveform regimes. Therefore, optimising electrical conditioning protocols requires a careful balance between promoting maturation and maintaining electrochemical stability.

The maturation signatures observed in this study were derived from a model in which cells were expanded and differentiated in two-dimensional culture before incorporation into three-dimensional engineered tissues, but which lacked mechanical loading or the full architectural complexity of more advanced engineering systems. Cardiomyocyte maturation is known to depend on integrated electromechanical cues, including extracellular matrix organisation and mechanical strain. Therefore, the transcriptional responses documented here likely

represent early-stage maturation pathways rather than fully matured adult phenotypes. Nonetheless, the structured transcriptional responses identified demonstrate that waveform parameters alone can be associated with the reorganisation of maturation-related gene networks, even in the absence of additional biomechanical stimuli.

From a translational perspective, this indicates a need to revise the conceptual framework of electrical conditioning in cardiac tissue engineering. Instead of considering stimulation merely as a binary intervention, waveform architecture should be regarded as a design variable that can be systematically optimised to influence cardiomyocyte maturation. The structured DOE approach used here provides a practical framework for identifying electrical conditioning protocols that encourage coordinated maturation while operating within safe electrochemical limits.

The results from Objective 4 show that electrical stimulus design has a measurable though cautious, systems-level association on cardiomyocyte maturation, coordinating integrated transcriptional networks across structural, electrophysiological, and calcium-handling domains. This broadens the main premise of the current work beyond organ-level electrophysiology to focus on the cellular level. Just as waveform architecture influences myocardial excitation and arrhythmia susceptibility in vivo, it may also act as a controllable conditioning variable associated with maturation-related transcriptional patterning of engineered cardiac tissues.

This thesis proposes a cross-scale framework that connects waveform engineering with cardiac biology. The programmable stimulation platform from Objective 1 allowed controlled studies of subcutaneous myocardial excitability in Objective 2, which helped analyse arrhythmia induction in Objective 3. Objective 4 showed that waveform parameters affecting organ-level electrophysiology are also associated with maturation-related transcriptional organisation in engineered cardiac tissue.

These findings support the view that electrical waveform parameters are an important design variable influencing cardiac electrophysiology in vivo and associated with maturation-relevant transcriptional organisation in vitro.

6.2. Future Works

Across all experiments, stimulation architecture emerged as an important factor influencing cardiac excitation and arrhythmogenesis and as a variable associated with maturation-relevant transcriptional organisation in hiPSC-derived cardiomyocytes. At the same time, the study identifies several promising directions for future research. These directions are based both on the findings of the present work and on the remaining mechanistic, methodological and translational questions that must be addressed to optimise waveform design in more precisely controlled experimental and clinical settings.

At the organ level, subcutaneous pacing experiments corroborated that classical strength-duration relationships remain applicable under extravascular stimulation, although with markedly increased energy requirements. Future research should aim to validate and extend these findings. This will require larger cohorts and more rigorous experimental designs to quantify intersubject variability in rheobase and chronaxie more accurately. Incorporating anatomical parameters such as thoracic impedance, electrode-myocardium distance, and tissue geometry could enhance mechanistic insights and facilitate more accurate modelling of current-density distributions in extravascular pacing systems.

The experiments on ventricular fibrillation induction revealed a notable trade-off between peak current demands and the average current burden. Subsequent studies should investigate this relationship through narrower DOE boundaries guided by insights from Objective 3. Additionally, characterisation of inter-pulse delay parameters could elucidate the effects of optimised biphasic waveforms. Coupling these experimental insights with detailed modelling of implantable power electronics would enable a comprehensive evaluation of waveform optimisation, encompassing electrophysiological efficacy, converter efficiency, battery longevity, and thermal management. Such integrated analyses are instrumental in informing the development of lower-voltage and more energy-efficient architectures for next-generation extravascular defibrillation devices.

At the cellular level, experiments utilising hiPSC-derived cardiomyocytes demonstrated that waveform configurations were associated with structured changes in the coordinated transcriptional networks associated with cardiomyocyte maturation. An important subsequent step is to replicate and extend these investigations by applying refined ranges of electrical parameters that remain within biologically permissible limits. The current study identified specific high-energy waveform conditions that destabilised the culture environment, thereby establishing a valuable reference point for delineating a safe electrical conditioning window. Future research should expand on this foundation by using larger sample sizes and more robust experimental design (DOE) frameworks to better understand

the relationship between waveform parameters and maturation, with greater statistical confidence.

Additionally, the interpretation of hiPSC-CM maturation data will be enhanced by integrating other phenotypic datasets. The ongoing sarcomeric imaging analyses are expected to provide vital structural insights that put the transcriptional results into context. Particular emphasis should be placed on sarcomeric alignment, organisation and anisotropy, as these structural features may help determine whether the transcriptional patterns observed here are accompanied by measurable morphological maturation. If these structural markers reveal a stronger maturation signature than gene expression alone, they could significantly improve understanding of waveform-dependent maturation pathways.

Future research should aim for two main goals: optimising waveform design for use in extravascular cardiac devices and improving electrical conditioning protocols for engineered cardiac tissues. By systematically exploring the parameter space outlined here, electrical stimulation can evolve from an empirical intervention to a carefully designed modality. This progress would enable precise control of cardiac development and function, thereby enhancing the translational potential of electrical conditioning in cardiac regenerative therapies.

Bibliography

1. Bennett P. Peter_Bennett_10212759_Raw_Data_supporting objective evidence. Zenodo; 2026. doi:10.5281/zenodo.20190662

2. World Health organisation. World Health Organisation [Internet]. [cited 2026 Mar 18]. Cardiovascular diseases (CVDs). Available from: https://www.who.int/news-room/fact-sheets/detail/cardiovascular-diseases-(cvds)

3. Palaniappan L, Allen N, Almarzooq Z. professional.heart.org [Internet]. 2026 [cited 2026 Mar 18]. 2026 Heart disease and stroke statistics: a report of US and global data from the American Heart Association. Available from: https://professional.heart.org/en/science-news/2026-heart-disease-and-stroke-statistics

4. Zipes DP, Wellens HJJ. Sudden Cardiac Death. Circulation. 1998;98(21):2334–51. doi:10.1161/01.CIR.98.21.2334.

5. John RM, Tedrow UB, Koplan BA, Albert CM, Epstein LM, Sweeney MO, et al. Ventricular arrhythmias and sudden cardiac death. The Lancet. 2012 Oct;380(9852):1520–9. doi:10.1016/S0140-6736(12)61413-5

6. Konishi S, Minamiguchi H, Masuda M, Ashihara T, Okuyama Y, Ohtani T, et al. Self-terminated long-lasting ventricular fibrillation: What is the mechanism? Journal of Cardiology Cases. 2014 Oct;10(4):136–9. doi:10.1016/j.jccase.2014.06.005

7. Adgey AAJ, Spence MS, Walsh SJ. Theory and practice of defibrillation: (2) defibrillation for ventricular fibrillation. Heart. 2005 Jan;91(1):118–25. doi:10.1136/hrt.2003.019927

8. Awada HK, Hwang MP, Wang Y. Towards comprehensive cardiac repair and regeneration after myocardial infarction: Aspects to consider and proteins to deliver. Biomaterials. 2016 Mar;82:94–112. doi:10.1016/j.biomaterials.2015.12.025

9. Kikuchi K, Poss KD. Cardiac Regenerative Capacity and Mechanisms. Annual Review of Cell and Developmental Biology. 2012 Nov 10;28(1):719–41. doi:10.1146/annurev-cellbio-101011-155739

10. James EC, Tomaskovic-Crook E, Crook JM. Bioengineering Clinically Relevant Cardiomyocytes and Cardiac Tissues from Pluripotent Stem Cells. IJMS. 2021 Mar 16;22(6):3005. doi:10.3390/ijms22063005

11. Uygur A, Lee RT. Mechanisms of Cardiac Regeneration. Developmental Cell. 2016 Feb;36(4):362–74. doi:10.1016/j.devcel.2016.01.018

12. Bardy GH, Smith WM, Hood MA, Crozier IG, Melton IC, Jordaens L, et al. An Entirely Subcutaneous Implantable Cardioverter–Defibrillator. N Engl J Med. 2010 Jul;363(1):36–44. doi:10.1056/NEJMoa0909545

13. Park. Development and Function of the Cardiac Conduction System in Health and Disease. Journal of Cardiovascular Development and Disease. 2017. doi:10.3390/jcdd4020007

14. White DW, Raven PB. Autonomic neural control of heart rate during dynamic exercise: revisited. The Journal of Physiology. 2014 Jun 15;592(12):2491–500. doi:10.1113/jphysiol.2014.271858

15. Kashou AH, Basit H, Chhabra L. Physiology, Sinoatrial Node. In: StatPearls [Internet] [Internet]. StatPearls Publishing; 2022 [cited 2026 Apr 24]. Available from: https://www.ncbi.nlm.nih.gov/books/NBK459238/ PubMed PMID: 29083608.

16. Ball CM, Featherstone PJ. The early history of cardiac pacing. Anaesth Intensive Care. 2019 Jul;47(4):320–1. doi:10.1177/0310057X19860986

17. Nelson GD. A Brief History of Cardiac Pacing. Texas Heart Institute Journal. 1993;20(1):12.

18. Maria E, Olaru A, Cappelli S. The Entirely Subcutaneous Defibrillator (S-Icd): State of the Art and Selection of the Ideal Candidate. CCR. 2014 Dec 24;11(2):180–6. doi:10.2174/1573403X10666140827094126

19. Spach MS, Heidlage JF, Barr RC, Dolber PC. Cell size and communication: Role in structural and electrical development and remodeling of the heart. Heart Rhythm. 2004 Oct;1(4):500–15. doi:10.1016/j.hrthm.2004.06.010

20. Veeraraghavan R, Gourdie RG, Poelzing S. Mechanisms of cardiac conduction: a history of revisions. American Journal of Physiology-Heart and Circulatory Physiology. 2014;306(5):H619–27.

21. Dalsey W, Syverud S, Trott A. Transcutaneous cardiac pacing. J Emerg Med. 1984;1(3):201–5. doi:10.1016/0736-4679(84)90072-6 PubMed PMID: 6386970.

22. Maria ED, Giacopelli D, Borghi A, Modonesi L, Cappelli S. Antitachycardia pacing programming in implantable cardioverter defibrillator: A systematic review. WJC. 2017;9(5):429. doi:10.4330/wjc.v9.i5.429

23. Gorbunov BB, Vostrikov VA, Nesterenko IV, Telyshev DV. A History of the Discovery of the Hoorweg–Weiss–Lapicque Law. Biomed Eng. 2019 Jan;52(5):357–60. doi:10.1007/s10527-019-09847-7

24. Lapicque, L. Recherches quantitatives sur l'excitation electrique des nerfs traites comme une polarization. Journal de physiologie et de pathologie générale. 1907;9:620–35.

25. Weiss,G. Sur la possibilité de render comparable entre les appareils cervant à l'excitation électrique. Archives Italiennes de Biologie. 1901;35:413–46.

26. Serbetci YA, Jaryal S, Bhasin I, Elhassan M, Muslim A, Aquilini P, et al. Pacemakers in Modern Cardiology and Their Transition From Traditional to Leadless Models. Cureus. 2025 Apr 13. doi:10.7759/cureus.82182

27. Boersma L, Barr C, Knops R, Theuns D, Eckardt L, Neuzil P, et al. Implant and Midterm Outcomes of the Subcutaneous Implantable Cardioverter-Defibrillator Registry. Journal of the American College of Cardiology. 2017 Aug;70(7):830–41. doi:10.1016/j.jacc.2017.06.040

28. Friedman P, Murgatroyd F, Boersma LVA, Manlucu J, O'Donnell D, Knight BP, et al. Efficacy and Safety of an Extravascular Implantable Cardioverter–Defibrillator. N Engl J Med. 2022 Oct 6;387(14):1292–302. doi:10.1056/NEJMoa2206485

29. Akerström F. Subcutaneous implantable defibrillator: State-of-the art 2013. WJC. 2013;5(9):347. doi:10.4330/wjc.v5.i9.347

30. Ahmed RE, Anzai T, Chanthra N, Uosaki H. A Brief Review of Current Maturation Methods for Human Induced Pluripotent Stem Cells-Derived Cardiomyocytes. Front Cell Dev Biol. 2020 Mar 19;8:178. doi:10.3389/fcell.2020.00178

31. Karbassi E, Fenix A, Marchiano S, Muraoka N, Nakamura K, Yang X, et al. Cardiomyocyte maturation: advances in knowledge and implications for regenerative medicine. Nat Rev Cardiol. 2020 Jun;17(6):341–59. doi:10.1038/s41569-019-0331-x

32. Nunes SS, Miklas JW, Liu J, Aschar-Sobbi R, Xiao Y, Zhang B, et al. Biowire: a platform for maturation of human pluripotent stem cell–derived cardiomyocytes. Nat Methods. 2013 Aug;10(8):781–7. doi:10.1038/nmeth.2524

33. Tiburcy M, Hudson JE, Balfanz P, Schlick S, Meyer T, Chang Liao ML, et al. Defined Engineered Human Myocardium With Advanced Maturation for Applications in Heart Failure Modeling and Repair. Circulation. 2017 May 9;135(19):1832–47. doi:10.1161/CIRCULATIONAHA.116.024145

34. Sun X, Nunes SS. Bioengineering Approaches to Mature Human Pluripotent Stem Cell-Derived Cardiomyocytes. Front Cell Dev Biol. 2017 Mar 9;5. doi:10.3389/fcell.2017.00019

35. Tandon N, Cannizzaro C, Chao PHG, Maidhof R, Marsano A, Au HTH, et al. Electrical stimulation systems for cardiac tissue engineering. Nat Protoc. 2009 Feb;4(2):155–73. doi:10.1038/nprot.2008.183

36. Tandon N, Marsano A, Maidhof R, Wan L, Park H, Vunjak-Novakovic G. Optimization of electrical stimulation parameters for cardiac tissue engineering. J Tissue Eng Regen Med. 2011 Jun;5(6):e115–25. doi:10.1002/term.377

37. Coates, S, Thwaites, B. The Strength-Duration Curve and Its Importance in Pacing Efficiency: A Study of 325 Pacing Leads in 229 Patients. Pacing and Clinical Electrophysiology [Internet]. 2000. p. 1273–7. Available from: https://onlinelibrary.wiley.com/doi/abs/10.1111/j.1540-8159.2000.tb00943.x

38. Friedman DJ, Parzynski CS, Varosy PD, Prutkin JM, Patton KK, Mithani A, et al. Trends and In-Hospital Outcomes Associated With Adoption of the Subcutaneous Implantable Cardioverter Defibrillator in the United States. JAMA Cardiol. 2016 Nov 1;1(8):900. doi:10.1001/jamacardio.2016.2782

39. Link MS, Joglar JA. Transvenous or Subcutaneous ICD — Similar but Different. N Engl J Med. 2020 Aug 6;383(6):587–8. doi:10.1056/NEJMe2022198

40. Lambiase PD, Barr C, Theuns DAMJ, Knops R, Neuzil P, Johansen JB, et al. Worldwide experience with a totally subcutaneous implantable defibrillator: early results from the EFFORTLESS S-ICD Registry. European Heart Journal. 2014 Jul 1;35(25):1657–65. doi:10.1093/eurheartj/ehu112

41. Ronaldson-Bouchard K, Ma SP, Yeager K, Chen T, Song L, Sirabella D, et al. Advanced maturation of human cardiac tissue grown from pluripotent stem cells. Nature. 2018 Apr;556(7700):239–43. doi:10.1038/s41586-018-0016-3

42. Godier-Furnémont AFG, Tiburcy M, Wagner E, Dewenter M, Lämmle S, El-Armouche A, et al. Physiologic force-frequency response in engineered heart muscle by electromechanical stimulation. Biomaterials. 2015 Aug;60:82–91. doi:10.1016/j.biomaterials.2015.03.055

43. Ruan JL, Tulloch NL, Razumova MV, Saiget M, Muskheli V, Pabon L, et al. Mechanical stress conditioning and electrical stimulation promote contractility and force maturation of induced pluripotent stem cell-derived human cardiac tissue. Circulation. 2016;134(20):1557–67. doi:10.1161/CIRCULATIONAHA.114.014998

44. Stoppel WL, Kaplan DL, Black LD. Electrical and mechanical stimulation of cardiac cells and tissue constructs. Advanced Drug Delivery Reviews. 2016 Jan;96:135–55. doi:10.1016/j.addr.2015.07.009

45. Gabetti S, Sileo A, Montrone F, Putame G, Audenino AL, Marsano A, et al. Versatile electrical stimulator for cardiac tissue engineering—Investigation of charge-balanced monophasic and biphasic electrical stimulations. Front Bioeng Biotechnol. 2023 Jan 4;10:1031183. doi:10.3389/fbioe.2022.1031183

46. Tandon N, Marsano A, Cannizzaro C, Voldman J, Vunjak-Novakovic G. Design of electrical stimulation bioreactors for cardiac tissue engineering. In: 2008 30th annual international conference of the IEEE engineering in medicine and biology society. IEEE; 2008. p. 3594–7.

47. Baranowski B, Saarel EV, Chung MK. Imaging of Implantable Devices. In: Clinical Cardiac Pacing, Defibrillation and Resynchronization Therapy [Internet]. Elsevier; 2011 [cited 2022 Oct 10]. p. 771–810. Available from: https://linkinghub.elsevier.com/retrieve/pii/B9781437716160000278 doi:10.1016/B978-1-4377-1616-0.00027-8

48. Ballantyne B, Chew D, Vandenberk B. Paradigm Shifts in Cardiac Pacing: Where Have We Been and What Lies Ahead? JCM. 2023 Apr 18;12(8):2938. doi:10.3390/jcm12082938

49. Feyen DAM, McKeithan WL, Bruyneel AAN, Spiering S, Hörmann L, Ulmer B, et al. Metabolic Maturation Media Improve Physiological Function of Human iPSC-Derived Cardiomyocytes. Cell Reports. 2020 Jul;32(3):107925. doi:10.1016/j.celrep.2020.107925

50. Chiu LLY, Iyer RK, King JP, Radisic M. Biphasic Electrical Field Stimulation Aids in Tissue Engineering of Multicell-Type Cardiac Organoids. Tissue Engineering Part A. 2011 Jun;17(11–12):1465–77. doi:10.1089/ten.tea.2007.0244

51. Boston Scientific Corporation. EMBLEM S-ICD and EMBLEM MRI S-ICD: Subcutaneous Implantable Cardioverter Defibrillator Physician Technical Manual [Physician Technical Manual] [Internet]. Marlborough, MA; 2022 Mar [cited 2025 May 12]. Physician Technical Manual 359481–001. Available from: https://www.bostonscientific.com/content/dam/bostonscientific/Rhythm%20Management/portfolio-group/EMBLEM_S-ICD/Download_Center/359481-001%20EMBLEM%20S-ICD%20PTM_English.pdf

52. Kolbl F, Bornat Y, Castelli J, Regnacq L, N'Kaoua G, Renaud S, et al. IC-Based Neuro-Stimulation Environment for Arbitrary Waveform Generation. Electronics. 2021 Aug 3;10(15):1867. doi:10.3390/electronics10151867

53. Grounding. In: Electromagnetic compatibility engineering. Hoboken, N.J: John Wiley & Sons; 2009. p. 107–40.

54. Doshi SK, Pittaro MD, Reeves R, Boyce K, Payne JP, Kroll MW, et al. Efficacy of Tuned Waveforms Based on Different Membrane Time Constants on Defibrillation Thresholds: Primary Results from the POWER Trial: DEFIBRILLATION EFFICACY-TUNED WAVEFORMS. Pacing and Clinical Electrophysiology. 2012 Oct;35(10):1253–61. doi:10.1111/j.1540-8159.2012.03500.x

55. Koster RW, Dorian P, Chapman FW, Schmitt PW, O'Grady SG, Walker RG. A randomized trial comparing monophasic and biphasic waveform shocks for external cardioversion of atrial fibrillation. American Heart Journal. 2004 May;147(5):e1–7. doi:10.1016/j.ahj.2003.10.049

56. Niebauer MJ, Brewer JE, Chung MK, Tchou PJ. Comparison of the rectilinear biphasic waveform with the monophasic damped sine waveform for external cardioversion of atrial fibrillation and flutter. The American Journal of Cardiology. 2004 Jun;93(12):1495–9. doi:10.1016/j.amjcard.2004.03.006

57. Casciola M, Feaster TK, Caiola MJ, Keck D, Blinova K. Human in vitro assay for irreversible electroporation cardiac ablation. Front Physiol. 2023 Jan 9;13:1064168. doi:10.3389/fphys.2022.1064168

58. Grill WM, Mortimer JT. Stimulus waveforms for selective neural stimulation. IEEE Eng Med Biol Mag. 1995 Aug;14(4):375–85. doi:10.1109/51.395310

59. Bennett P. Peter_Bennett_10212759_Chapter_2_Raw_Data_supporting objective evidence. Zenodo; 2026. doi:10.5281/zenodo.19987007

60. Merrill DR, Bikson M, Jefferys JGR. Electrical stimulation of excitable tissue: design of efficacious and safe protocols. Journal of Neuroscience Methods. 2005 Feb;141(2):171–98. doi:10.1016/j.jneumeth.2004.10.020

61. Van Barreveld M, Verstraelen TE, Van Dessel PFHM, Boersma LVA, Delnoy PPHM, Tuinenburg AE, et al. Dutch Outcome in Implantable Cardioverter-Defibrillator Therapy: Implantable Cardioverter-Defibrillator–Related Complications in a Contemporary Primary Prevention Cohort. JAHA. 2021 Apr 6;10(7):e018063. doi:10.1161/JAHA.120.018063

62. Kirkfeldt RE, Johansen JB, Nohr EA, Jorgensen OD, Nielsen JC. Complications after cardiac implantable electronic device implantations: an analysis of a complete, nationwide cohort in Denmark. European Heart Journal. 2014 May 2;35(18):1186–94. doi:10.1093/eurheartj/eht511

63. Koneru JN, Jones PW, Hammill EF, Wold N, Ellenbogen KA. Risk Factors and Temporal Trends of Complications Associated With Transvenous Implantable Cardiac Defibrillator Leads. JAHA. 2018 May 15;7(10):e007691. doi:10.1161/JAHA.117.007691

64. Knops RE, Olde Nordkamp LRA, Delnoy PPHM, Boersma LVA, Kuschyk J, El-Chami MF, et al. Subcutaneous or Transvenous Defibrillator Therapy. N Engl J Med. 2020 Aug 6;383(6):526–36. doi:10.1056/NEJMoa1915932

65. Thompson AE, Atwater B, Boersma L, Crozier I, Engel G, Friedman P, et al. The development of the extravascular defibrillator with substernal lead placement: A new Frontier for device-based treatment of sudden cardiac arrest. Cardiovasc electrophysiol. 2022 Jun;33(6):1085–95. doi:10.1111/jce.15511

66. Knops RE, Pepplinkhuizen S, Delnoy PPHM, Boersma LVA, Kuschyk J, El-Chami MF, et al. Device-related complications in subcutaneous versus transvenous ICD: a secondary analysis of the PRAETORIAN trial. European Heart Journal. 2022 Dec 14;43(47):4872–83. doi:10.1093/eurheartj/ehac496

67. Crozier I, Haqqani H, Kotschet E, Shaw D, Prabhu A, Roubos N, et al. First-in-Human Chronic Implant Experience of the Substernal Extravascular Implantable Cardioverter-Defibrillator. JACC: Clinical Electrophysiology. 2020 Nov;6(12):1525–36. doi:10.1016/j.jacep.2020.05.029

68. Sears SF, Harrell R, Crozier I, Murgatroyd F, Boersma LV, Manlucu J, et al. Patient-reported quality of life and acceptance of the extravascular implantable cardioverter-defibrillator: results from pivotal study. Journal of cardiovascular electrophysiology. 2024;35(2):240–6.

69. Jolley M, Stinstra J, Tate J, Pieper S, MacLeod R, Chu L, et al. Finite element modeling of subcutaneous implantable defibrillator electrodes in an adult torso. Heart Rhythm. 2010 May;7(5):692–8. doi:10.1016/j.hrthm.2010.01.030

70. Sholevar DP, Tung S, Kuriachan V, Leong-Sit P, Roukoz H, Engel G, et al. Feasibility of extravascular pacing with a novel substernal electrode configuration: The Substernal Pacing Acute Clinical Evaluation study. Heart Rhythm. 2018 Apr;15(4):536–42. doi:10.1016/j.hrthm.2017.11.030

71. Guide for the Care and Use of Laboratory Animals: Eighth Edition [Internet]. Washington, D.C.: National Academies Press; 2011 [cited 2025 May 31]. Available from: http://www.nap.edu/catalog/12910 doi:10.17226/12910

72. Gliner BE, Lyster TE, Dillion SM, Bardy GH. Transthoracic Defibrillation of Swine With Monophasic and Biphasic Waveforms. Circulation. 1995. p. 1634–43.

73. Costea R, Ene I, Pavel R. Pig Sedation and Anesthesia for Medical Research. Animals. 2023 Dec 10;13(24):3807. doi:10.3390/ani13243807

74. Rushton WAH. Lapicque's canonical strength duration curve. The Journal of Physiology. 1932;74(4):424–40. doi:https://doi.org/10.1113/jphysiol.1932.sp002859

75. Geddes. The strength-duration curve. IEEE Trans Biomed Eng. 1985. doi:10.1109/TBME.1985.325456

76. Irnich. The chronaxie time and its practical importance. Pacing Clin Electrophysiol. 1980. doi:10.1111/j.1540-8159.1980.tb05236.x

77. Molnár L, Crozier I, Haqqani H, O'Donnell D, Kotschet E, Alison J, et al. The extravascular implantable cardioverter-defibrillator: characterization of anatomical parameters impacting substernal implantation and defibrillation efficacy. EP Europace. 2022 May 3;24(5):762–73. doi:10.1093/europace/euab243

78. Rodríguez-Reyes H, Muñoz-Gutiérrez M, Salas-Pacheco JL. Current behavior of sudden cardiac arrest and sudden death. ACME. 2020 Sep 8;90(2):4584. doi:10.24875/ACME.M20000114

79. Jabbari R, Engstrøm T, Glinge C, Risgaard B, Jabbari J, Winkel BG, et al. Incidence and Risk Factors of Ventricular Fibrillation Before Primary Angioplasty in Patients With First ST-

Elevation Myocardial Infarction: A Nationwide Study in Denmark. JAHA. 2015 Jan 5;4(1):e001399. doi:10.1161/JAHA.114.001399

80. Ellenbogen KA, Kaszala K. Cardiac pacing and ICDs. Vol. 4. John Wiley & Sons; 2014. 455–458 p.

81. Hayase J, Do DH, Boyle NG. Defibrillation Threshold Testing: Current Status. Arrhythmia & Electrophysiology Review. 2018;7(4):288. doi:10.15420/aer.2018.54.2

82. le Polain de Waroux JB, Ploux S, Mondoly P, Eschalier R, Strik M, Houard L, et al. Defibrillation testing is mandatory in patients with subcutaneous implantable cardioverter–defibrillator to confirm appropriate ventricular fibrillation detection. Heart Rhythm. 2018 May;15(5):642–50. doi:10.1016/j.hrthm.2018.02.013

83. Bänsch D, Bonnemeier H, Brandt J, Bode F, Svendsen JH, Táborský M, et al. Intra-operative defibrillation testing and clinical shock efficacy in patients with implantable cardioverter-defibrillators: the NORDIC ICD randomized clinical trial. Eur Heart J. 2015 Oct 1;36(37):2500–7. doi:10.1093/eurheartj/ehv292

84. Healey JS, Hohnloser SH, Glikson M, Neuzner J, Mabo P, Vinolas X, et al. Cardioverter defibrillator implantation without induction of ventricular fibrillation: a single-blind, non-inferiority, randomised controlled trial (SIMPLE). The Lancet. 2015 Feb;385(9970):785–91. doi:10.1016/S0140-6736(14)61903-6

85. Wilkoff BL, Fauchier L, Stiles MK, Morillo CA, Al-Khatib SM, Almendral J, et al. 2015 HRS/EHRA/APHRS/SOLAECE expert consensus statement on optimal implantable cardioverter-defibrillator programming and testing. Europace. 2016 Feb;18(2):159–83. doi:10.1093/europace/euv411

86. Knops RE, Marquie C, Nordbeck P, Tilz R, Dijkshoorn LA, Quast AFBE, et al. Subcutaneous Defibrillator Implantation With or Without Defibrillation Test: The Primary Results of the Randomized PRAETORIAN-DFT Trial. Circulation. 2026 Apr 25;CIRCULATIONAHA.126.080638. doi:10.1161/CIRCULATIONAHA.126.080638

87. Quast AFBE, Baalman SWE, Betts TR, Boersma LVA, Bonnemeier H, Boveda S, et al. Rationale and design of the PRAETORIAN-DFT trial: A prospective randomized CompArative trial of SubcutanEous ImplanTable CardiOverter-DefibrillatoR ImplANtation with and without DeFibrillation testing. American Heart Journal. 2019 Aug;214:167–74. doi:10.1016/j.ahj.2019.05.002

88. Crozier I, O'Donnell D, Boersma L, Murgatroyd F, Manlucu J, Knight BP, et al. The extravascular implantable cardioverter-defibrillator: The pivotal study plan. J Cardiovasc Electrophysiol. 2021 Sep;32(9):2371–8. doi:10.1111/jce.15190 PubMed PMID: 34322918; PubMed Central PMCID: PMC9290824.

89. Voroshilovsky O, Qu Z, Lee MH, Ohara T, Fishbein GA, Huang HLA, et al. Mechanisms of Ventricular Fibrillation Induction by 60-Hz Alternating Current in Isolated Swine Right Ventricle. Circulation. 2000 Sep 26;102(13):1569–74. doi:10.1161/01.CIR.102.13.1569

90. Cao JM, Qu Z, Kim YH, Wu TJ, Garfinkel A, Weiss JN, et al. Spatiotemporal Heterogeneity in the Induction of Ventricular Fibrillation by Rapid Pacing: Importance of Cardiac Restitution Properties. Circulation Research. 1999 Jun 11;84(11):1318–31. doi:10.1161/01.RES.84.11.1318

91. Chen B, Yu T, Ristagno G, Quan W, Li Y. Average current is better than peak current as therapeutic dosage for biphasic waveforms in a ventricular fibrillation pig model of cardiac arrest. Resuscitation. 2014 Oct;85(10):1399–404. doi:10.1016/j.resuscitation.2014.06.029

92. Furman. Energy consumption for cardiac stimulation as a function of pulse duration. J Surg Res. 1966. doi:10.1016/S0022-4804(66)80025-2

93. Frommeyer G, Zumhagen S, Dechering DG, Larbig R, Bettin M, Löher A, et al. Intraoperative Defibrillation Testing of Subcutaneous Implantable Cardioverter-Defibrillator Systems—A Simple Issue? JAHA. 2016 Mar 9;5(3):e003181. doi:10.1161/JAHA.115.003181

94. Malkin RA, Hoffmeister BK. Mechanisms by which AC Leakage Currents Cause Complete Hemodynamic Collapse Without Inducing Fibrillation. Cardiovasc electrophysiol. 2001 Oct;12(10):1154–61. doi:10.1046/j.1540-8167.2001.01154.x

95. Lambiase PD, Theuns DA, Murgatroyd F, Barr C, Eckardt L, Neuzil P, et al. Subcutaneous implantable cardioverter-defibrillators: long-term results of the EFFORTLESS study. European Heart Journal. 2022 Jun 1;43(21):2037–50. doi:10.1093/eurheartj/ehab921

96. Cahill TJ, Choudhury RP, Riley PR. Heart regeneration and repair after myocardial infarction: translational opportunities for novel therapeutics. Nat Rev Drug Discov. 2017 Oct;16(10):699–717. doi:10.1038/nrd.2017.106

97. World Health Organization. WHO CVDs Fact Sheet [Fact sheet] [Internet]. World Health Organization; 2019 [cited 2025 Jun 2]. Available from: https://www.who.int/news-room/fact-sheets/detail/cardiovascular-diseases-(cvds)

98. Kamal NH, Heikal LA, Abdallah OY. The future of cardiac repair: a review on cell-free nanotherapies for regenerative myocardial infarction. Drug Deliv and Transl Res. 2025 Jul;15(7):2253–71. doi:10.1007/s13346-024-01763-y

99. Prabhu. The biological basis for cardiac repair after myocardial infarction: from inflammation to fibrosis. Circ Res. 2016. doi:10.1161/CIRCRESAHA.116.303577

100. Kong. The pathogenesis of cardiac fibrosis. Cellular and Molecular Life Sciences. 2014. doi:10.1007/s00018-013-1349-6

101. Verheule S, Schotten U. Electrophysiological Consequences of Cardiac Fibrosis. Cells. 2021 Nov 18;10(11):3220. doi:10.3390/cells10113220

102. Zhuang RZ, Lock R, Liu B, Vunjak-Novakovic G. Opportunities and challenges in cardiac tissue engineering from an analysis of two decades of advances. Nat Biomed Eng. 2022 Apr 27;6(4):327–38. doi:10.1038/s41551-022-00885-3

103. Laflamme M A, Chen K Y, Naumova A V. Cardiomyocytes derived from human embryonic stem cells in pro-survival factors enhance function of infarcted rat hearts. Nature Biotechnology. 2007;25(9):1015-24. doi:10.1038/nbt1327

104. de Lange WJ, Farrell ET, Kreitzer CR, Jacobs DR, Lang D, Glukhov AV, et al. Human iPSC-engineered cardiac tissue platform faithfully models important cardiac physiology. American Journal of Physiology-Heart and Circulatory Physiology. 2021 Apr 1;320(4):H1670–86. doi:10.1152/ajpheart.00941.2020

105. Takahashi K, Tanabe K, Ohnuki M, Narita M, Ichisaka T, Tomoda K, et al. Induction of Pluripotent Stem Cells from Adult Human Fibroblasts by Defined Factors. Cell. 2007 Nov;131(5):861–72. doi:10.1016/j.cell.2007.11.019

106. Lundy SD, Zhu WZ, Regnier M, Laflamme MA. Structural and Functional Maturation of Cardiomyocytes Derived from Human Pluripotent Stem Cells. Stem Cells and Development. 2013 Jul 15;22(14):1991–2002. doi:10.1089/scd.2012.0490

107. Zhang C, Zhu J, Zhou Y, Thampatty BP, Wang JHC. Tendon Stem/Progenitor Cells and Their Interactions with Extracellular Matrix and Mechanical Loading. Stem Cells International. 2019 Oct 13;2019:1–10. doi:10.1155/2019/3674647

108. Young JL, Engler AJ. Hydrogels with time-dependent material properties enhance cardiomyocyte differentiation in vitro. Biomaterials. 2011 Feb;32(4):1002–9. doi:10.1016/j.biomaterials.2010.10.020

109. Valls-Margarit M, Iglesias-García O, Di Guglielmo C, Sarlabous L, Tadevosyan K, Paoli R, et al. Engineered Macroscale Cardiac Constructs Elicit Human Myocardial Tissue-like Functionality. Stem Cell Reports. 2019 Jul;13(1):207–20. doi:10.1016/j.stemcr.2019.05.024

110. Li W, Luo X, Strano A, Arun S, Gamm O, Poetsch MS, et al. Comprehensive promotion of iPSC-CM maturation by integrating metabolic medium with nanopatterning and electrostimulation. Nat Commun. 2025 Mar 21;16(1):2785. doi:10.1038/s41467-025-58044-6

111. Sachse FB, Moreno AP, Seemann G, Abildskov JA. A Model of Electrical Conduction in Cardiac Tissue Including Fibroblasts. Ann Biomed Eng. 2009 May;37(5):874–89. doi:10.1007/s10439-009-9667-4

112. Mohrman DE, Heller LJ. Overview of the Cardiovascular System. In: Cardiovascular Physiology, 9e [Internet]. New York, NY: McGraw-Hill Education; 2018 [cited 2023 Oct 16]. p. Chp 2 /Characteristics of Cardiac Muscle Cells/1-9. Available from: https://accessmedicine.mhmedical.com/content.aspx?bookid=2432&sectionid=190800450#1153946101

113. Jackman CP, Ganapathi AM, Asfour H, Qian Y, Allen BW, Li Y, et al. Engineered cardiac tissue patch maintains structural and electrical properties after epicardial implantation. Biomaterials. 2018 Mar;159:48–58. doi:10.1016/j.biomaterials.2018.01.002

114. Tzatzalos E, Abilez O J, Shukla P, Wu J C. Engineered heart tissues and induced pluripotent stem cells: macro- and microstructures for disease modeling, drug screening, and translational studies. Advanced drug delivery reviews. 2016;(96):234-244. doi:10.1016/j.addr.2015.09.010

115. Masuda A, Kurashina Y, Tani H, Soma Y, Muramatsu J, Itai S, et al. Maturation of Human iPSC-Derived Cardiac Microfiber with Electrical Stimulation Device. Adv Healthcare Materials. 2024 Oct;13(27):2303477. doi:10.1002/adhm.202303477

116. Bers DM. Cardiac excitation–contraction coupling. Nature. 2002;415 (6868):p.198-205. doi:10.1038/415198a

117. Hwang HS, Kryshtal DO, Feaster TK, Sánchez-Freire V, Zhang J, Kamp TJ, et al. Comparable calcium handling of human iPSC-derived cardiomyocytes generated by multiple laboratories. Journal of molecular and cellular cardiology. 2015;85:79–88.

118. Satin J, Itzhaki I, Rapoport S, Schroder EA, Izu L, Arbel G, et al. Calcium Handling in Human Embryonic Stem Cell-Derived Cardiomyocytes. Stem Cells. 2008 Aug 1;26(8):1961–72. doi:10.1634/stemcells.2007-0591

119. Carmeliet E. Cardiac Ionic Currents and Acute Ischemia: From Channels to Arrhythmias. Physiological Reviews. 1999 Jul 1;79(3):917–1017. doi:10.1152/physrev.1999.79.3.917

120. Liu J, Lieu DK, Siu CW, Fu JD, Tse HF, Li RA. Facilitated maturation of Ca2+handling properties of human embryonic stem cell-derived cardiomyocytes by calsequestrin expression. American Journal of Physiology-Cell Physiology. 2009;297(1):152–9. doi:10.1152/ajpcell.00060.2009

121. Liu J, Fu JD, Siu CW, Li RA. Functional Sarcoplasmic Reticulum for Calcium Handling of Human Embryonic Stem Cell-Derived Cardiomyocytes: Insights for Driven Maturation. Stem Cells. 2007 Dec 1;25(12):3038–44. doi:10.1634/stemcells.2007-0549

122. Yang X, Rodriguez ML, Leonard A, Sun L, Fischer KA, Wang Y, et al. Fatty Acids Enhance the Maturation of Cardiomyocytes Derived from Human Pluripotent Stem Cells. Stem Cell Reports. 2019 Oct;13(4):657–68. doi:10.1016/j.stemcr.2019.08.013

123. Correia C, Koshkin A, Duarte P, Hu D, Teixeira A, Domian I, et al. Distinct carbon sources affect structural and functional maturation of cardiomyocytes derived from human pluripotent stem cells. Sci Rep. 2017 Aug 17;7(1):8590. doi:10.1038/s41598-017-08713-4

124. Sánchez-Bueno A, Iglesias-García O, Montero-Calle P, Gavira JJ, Prosper F, Mazo MM. 3D Human Myocardial Tissue Generation Using Melt Electrospinning Writing of Polycaprolactone Scaffolds and hiPSC-Derived Cardiac Cells. JoVE. 2025 Mar 28;(217):67847. doi:10.3791/67847

125. Chan. Electrical Stimulation Promotes Maturation of Cardiomyocytes Derived from Human Embryonic Stem Cells. Journal of Cardiovascular Translational Research. 2013. doi:10.1007/s12265-013-9510-z

126. Miyoshi H, Morimura K, Hara R, Hori R, Watanabe E, Mochizuki N, et al. Short-term electrical stimulation promotes partial functional and morphological maturation of human-induced pluripotent stem cell-derived cardiomyocytes enabling cardiotoxicity risk mitigation at early-stage drug discovery for cardiac contractility modulation. Toxicological Sciences. 2026 Mar 2;209(3):kfag018. doi:10.1093/toxsci/kfag018

127. Shadrin IY, Allen BW, Qian Y, Jackman CP, Carlson AL, Juhas ME, et al. Cardiopatch platform enables maturation and scale-up of human pluripotent stem cell-derived engineered heart tissues. Nat Commun. 2017 Nov 28;8(1):1825. doi:10.1038/s41467-017-01946-x